J. Plasma Phys. (2025), *vol.* 91, E77
 doi:10.1017/S0022377825000200

On the convergence of bootstrap current to the Shaing–Callen limit in stellarators

Christopher G. Albert[1], Craig D. Beidler[2], Gernot Kapper[1], Sergei V. Kasilov[1,3] and Winfried Kernbichler[1]

[1]Fusion@ÖAW, Institute for Theoretical Physics - Computational Physics, Graz University of Technology, Graz 8010, Austria
[2]Max-Planck-Institut für Plasmaphysik, Greifswald 17489, Germany
[3]Institute of Plasma Physics, National Science Center "Kharkov Institute of Physics and Technology", Kharkov 61108, Ukraine

Corresponding author: Christopher Albert, albert@tugraz.at

(Received 31 July 2024; revision received 18 February 2025; accepted 19 February 2025)

The bootstrap current in stellarators can be presented as a sum of a collisionless value given by the Shaing–Callen asymptotic formula and an off-set current, which non-trivially depends on plasma collisionality and radial electric field. Using NEO-2 modeling, analytical estimates and semi-analytical studies with the help of a propagator method, it is shown that the off-set current in the $1/\nu$ regime does not converge with decreasing collisionality ν_* but rather shows oscillations over $\log \nu_*$ with an amplitude of the order of the bootstrap current in an equivalent tokamak. The convergence to the Shaing–Callen limit appears in regimes with significant orbit precession, in particular, due to a finite radial electric field, where the off-set current decreases as $\nu_*^{3/5}$. The off-set current strongly increases in case of nearly aligned magnetic field maxima on the field line where it diverges as $\nu_*^{-1/2}$ in the $1/\nu$ regime and saturates due to the precession at a level exceeding the equivalent tokamak value by $v_E^{*\,-1/2}$, where v_E^* is the perpendicular Mach number. The latter off-set, however, can be minimized by further aligning the local magnetic field maxima and by fulfilling an extra integral condition of "equivalent ripples" for the magnetic field. A criterion for the accuracy of this alignment and of ripple equivalence is derived. In addition, the possibility of the bootstrap effect at the magnetic axis caused by the above off-set is also discussed.

Key words: Fusion Plasma, Plasma Simulation

1. Introduction

One relatively simple way to evaluate the bootstrap current in stellarators is to use the long mean free path asymptotic formula of Shaing & Callen (1983) which

contains all the information about device geometry in a geometrical factor independent of plasma parameters. This way is especially suited for stellarator optimization (Beidler *et al.* 1990; Nakajima *et al.* 1989) where multiple fast estimates of the bootstrap current are required. Despite the fact that it has been derived more than 40 years ago, the validity range of this formula still remains unclear. Although the same result is exactly (Helander, Geiger & Maassberg *et al.* 2011) or approximately (Boozer & Gardner 1990) reproduced by different derivations, however, it is not reproduced in the $1/\nu$ regime by numerical modeling (Beidler *et al.* 2011). Namely, with decreasing normalized collisionality ν_*, the bootstrap coefficient does not come to a saturation at the asymptotic limit but rather shows a complicated behavior which is quite different at magnetic surfaces with different radii (Kernbichler *et al.* 2016). In turn, in the presence of a radial electric field, numerical modeling shows a saturation to the Shaing–Callen limit with decreasing ν_*. This feature of the bootstrap coefficient regularly observed in the drift kinetic equation solver, DKES (Hirshman *et al.* 1986; van Rij & Hirshman 1989) modeling, and later confirmed by various codes of different types (Beidler *et al.* 2011) has been pointed out to the authors of a paper by Henning Maassberg (2004) more than 20 years ago, and, together with the problem of bootstrap resonances (Boozer & Gardner 1990), it was the main reason to start the development of the drift kinetic equation solver NEO-2 (Kernbichler *et al.* 2008; Kasilov *et al.* 2014; Martitsch *et al.* 2016; Kernbichler *et al.* 2016; Kapper *et al.* 2016, 2018). Finally, we can present here the results of this long going effort.

Some of the reasons for the anomalous behavior of the bootstrap coefficient described above have been identified recently (Beidler 2020) by using the general solution of the ripple-averaged kinetic equation, GSRAKE (Beidler & D'haeseleer 1995), to determine the Ware-pinch coefficient, which is equivalent to the bootstrap coefficient due to Onsager symmetry. Although instructive, these results are largely of a qualitative nature, and one of the main purposes of this paper is to treat this problem in a more analytical manner, with subsequent verification by numerical modeling using NEO-2 and a simplified propagator method in order to provide simple scalings and certain conditions useful for stellarator optimization. The challenges which such an endeavor must face will also be illustrated by considering the extreme example of a so-called anti-sigma configuration – the antithesis of the model field considered in Mynick, Chu & Boozer (1982) – for which the bootstrap coefficient obviously diverges with decreasing collisionality over the entire ν_* range of DKES computations. A second purpose of this paper is to outline a simple numerical approach, utilizing the computations of the bootstrap coefficient in the $1/\nu$ regime, to also allow computations in regimes where particle precession (in particular, due to the radial electric field) is important, thereby providing an effective tool for the optimization problem mentioned above.

As shown below, for the 'anomalous' behavior of the bootstrap coefficient, the interaction between boundary layers separating co- and counter-passing particles from trapped particles and the layers separating different trapped particle classes from each other plays an important role. In collisionless asymptotic theories, these layers are assumed infinitely thin and non-overlapping. This cannot be fulfilled at irrational flux surfaces, where the number of trapped particle classes is infinite, while the width of the layers is finite at any collisionality. Another reason is the interaction of the trapped–passing boundary layer with itself, which happens in case of anti-sigma configurations where the magnetic field maximum at a given flux surface is reached on a line which splits the field line into non-equivalent segments exchanging transient particles via the boundary layer. In both cases, an important prerequisite

https://doi.org/10.1017/S0022377825000200 Published online by Cambridge University Press

for anomaly is a finite bounce-averaged cross-surface drift of trapped particles, which is absent in axisymmetric and nearly absent in sufficiently accurate quasi-symmetric configurations showing no anomalies of the bootstrap current (Landreman, Buller & Drevlak 2022).

We restrict our analysis here to the mono-energetic approach (Beidler *et al.* 2011) employing the Lorentz collision model, since this approach is sufficient for the account of main effects related to the magnetic field geometry. Effects of energy and momentum conservation pertinent to the full linearized collision model can be recovered then with good accuracy from the mono-energetic solutions of the kinetic equation using various momentum correction techniques (Taguchi 1992; Sugama & Nishimura 2002, 2008; Maassberg, Beidler & Turkin 2009). This mono-energetic approach is briefly outlined in § 2.1 where also the basic notation is introduced. In § 2.2 we re-derive the Shaing–Callen formula (Shaing & Callen 1983) within this approach in the $1/\nu$ transport regime in order to obtain an explicit solution for trapped particle distribution accounting for various trapped particle classes. The structure of this solution is quite demonstrative for the reasons behind the 'anomalous' behavior of the bootstrap current mentioned above. In that section, we also extend the alternative derivation of Helander *et al.* (2011) within the adjoint approach to the next order in collisionality. Although the obtained correction has no effect on the resulting Ware-pinch (bootstrap) coefficient, it is useful for understanding a certain paradox contained in this solution. Collisionless asymptotic solutions are compared with numerical solutions for finite plasma collisionality in § 2.3 where the cases with convergence of these solutions to the Shaing–Callen limit at low collisionality are demonstrated. In § 3 we examine the effect of collisional boundary layers on the distribution function in the adjoint (Ware pinch) problem where they lead to the off-set of this function from the value of collisionless asymptotic of Helander *et al.* (2011) and respective off-set of the Ware-pinch coefficient. In particular, in § 3.2 we introduce a simplified approach (propagator method) to describe this off-set in the leading order over collisionality with help of a set of Wiener–Hopf-type integral equations. This set is infinite in the case of irrational field lines, and becomes finite for closed field lines. In § 3.3, with the help of this set, we derive the conditions on the equilibrium magnetic field required to avoid the leading-order off-set. We obtain a simple expression for the distribution function off-set in the case these conditions are weakly violated in § 3.5, where we express these solutions via two discrete functions tabulated using the numerical solutions of two respective infinite integral equation sets resulting from the linearization of the original Wiener–Hopf-type set. In § 4 we examine the off-set of the distribution function and Ware-pinch coefficient at irrational flux surfaces both numerically, with the help of the NEO-2 code solutions at high-order rational magnetic field lines approximating the irrational surface (§ 4.1), and using the analytical estimates of the asymptotic behavior of the off-set with decreasing plasma collisionality (§ 4.2). A related issue of bootstrap resonances is briefly discussed in § 4.4. In § 5 we study the effect of banana orbit precession (in particular, due to a finite radial electric field) on the off-set of the Ware-pinch coefficient and formulate there a simple bounce-averaged approach for the account of this effect in computations of the Ware-pinch coefficient using the numerical solutions for the distribution function in the $1/\nu$ regime. A qualitative discussion of the off-set in the direct problem describing the bootstrap coefficient is presented in § 6 where we also examine the possibility of bootstrap effect at the magnetic axis. Finally, the results are summarized in § 7, where some implications for reactor optimization are also discussed.

https://doi.org/10.1017/S0022377825000200 Published online by Cambridge University Press

2. Asymptotic models and finite collisionality

In this section, we review asymptotical long mean free path models of the bootstrap and Ware-pinch effect in the set-up where all explicit and implicit assumptions used in derivations of those models are fulfilled. We use a standard method (Hinton & Hazeltine 1976; Galeev & Sagdeev 1979; Helander & Sigmar 2002) to re-derive transport coefficients in both cases, with a main focus on the boundary conditions in the presence of multiple trapped particle classes. We verify these models by numerical computation and identify their applicability range and mechanisms responsible for discrepancies at finite collisionality.

2.1. *Adjoint mono-energetic problems on a closed field line*

For the present analysis of bootstrap current convergence with plasma collisionality, a mono-energetic approach is sufficient, where a Lorentz collision model and constant electrostatic potential within flux surfaces are assumed. The linear deviation of the distribution function f from the local Maxwellian f_M is presented as a superposition of thermodynamic forces A_k as detailed in Kernbichler *et al.* (2016)

$$f - f_M = f_M \sum_{k=1}^{3} g_{(k)} A_k, \tag{2.1}$$

where

$$A_1 = \frac{1}{n_\alpha}\frac{\partial n_\alpha}{\partial r} - \frac{e_\alpha E_r}{T_\alpha} - \frac{3}{2T_\alpha}\frac{\partial T_\alpha}{\partial r}, \quad A_2 = \frac{1}{T_\alpha}\frac{\partial T_\alpha}{\partial r}, \quad A_3 = \frac{e_\alpha \langle E_\parallel B\rangle}{T_\alpha \langle B^2\rangle}, \tag{2.2}$$

where, e_α, m_α, n_α and T_α are the α species charge, mass, density and temperature, respectively, E_r, $E_\parallel$ are the radial (electrostatic) and parallel (inductive) electric field, B is the magnetic field strength and $\langle \ldots \rangle$ denotes a neoclassical flux surface average. This reduces the linearized drift kinetic equation in the $1/\nu$ regime to a set of independent equations

$$\hat{L} g_{(k)} \equiv \sigma \frac{\partial g_{(k)}}{\partial \varphi} - \frac{\partial}{\partial \eta}\left(D_\eta \frac{\partial g_{(k)}}{\partial \eta}\right) = s_{(k)}, \qquad D_\eta \equiv \frac{|\lambda|\eta}{l_c B^\varphi}, \tag{2.3}$$

which differ only by source terms

$$s_{(1)} = -\frac{B v_g^r}{|v_\parallel| B^\varphi} = \frac{\partial H'_\varphi}{\partial \eta}, \qquad s_{(2)} = z s_{(1)}, \qquad s_{(3)} = \frac{\sigma B^2}{B^\varphi}, \tag{2.4}$$

where

$$H'_\varphi = \frac{|\lambda|}{3B^\varphi}\left(3 + \lambda^2\right)|\nabla r| k_G \rho_L, \tag{2.5}$$

will be integrated along the field line later to give bounce integrals H_j in (2.26). Here, we use a field aligned coordinate system $(r, \vartheta_0, \varphi)$, where r is a flux surface label (effective radius) fixed by the condition $\langle |\nabla r| \rangle = 1$, $\vartheta_0 = \vartheta - \iota\varphi$ is a field line label, ι is the rotational transform and ϑ and φ are the poloidal and toroidal angles of periodic Boozer coordinates (Boozer 1981; d'Haeseleer *et al.* 1991), respectively. Variables in the velocity space are parallel velocity sign $\sigma = v_\parallel/|v_\parallel|$ and two invariants of motion, $z = m_\alpha v^2/(2T_\alpha)$ and $\eta = v_\perp^2/(v^2 B)$ respectively being the normalized kinetic energy (playing a role of parameter) and perpendicular adiabatic invariant (magnetic moment). The other notation is the pitch parameter

https://doi.org/10.1017/S0022377825000200 Published online by Cambridge University Press

$\lambda = v_\parallel/v = \sigma\sqrt{1-\eta B}$, the mean free path $l_c = v/(2\nu_\perp)$ defined via deflection frequency $\nu_\perp$ (the same as ν in Beidler *et al.* 2011), radial guiding center velocity $v_g^r = \mathbf{v}_g \cdot \nabla r$, Larmor radius $\rho_L = cm_\alpha v/(e_\alpha B)$ and the geodesic curvature given by

$$|\nabla r|k_G = (\mathbf{h}\times(\mathbf{h}\cdot\nabla)\mathbf{h})\cdot\nabla r = \frac{1}{B}(\mathbf{h}\times\nabla B)\cdot\nabla r = \frac{\mathrm{d}r}{\mathrm{d}\psi}\left(\frac{B_\vartheta}{B_\varphi+\iota B_\vartheta}\frac{\partial B}{\partial\varphi} - \frac{\partial B}{\partial\vartheta_0}\right), \tag{2.6}$$

with $\mathbf{h} = \mathbf{B}/B$ and ψ being the toroidal flux normalized by 2π and counted in the toroidal angle direction for the right-handed coordinate system and in the opposite direction for the left-handed system, and B^φ, B_φ and B_ϑ being contra- and covariant components of the magnetic field in Boozer coordinates.

Neoclassical transport coefficients D_{jk} link thermodynamic forces A_k by

$$\mathcal{I}_j = -n_\alpha \sum_{k=1}^{3} D_{jk}A_k, \tag{2.7}$$

to thermodynamic fluxes $\mathcal{I}_j$ defined via particle, Γ_α, and energy, Q_α, flux density and parallel flow velocity $V_{\parallel\alpha}$ as follows:

$$\mathcal{I}_1 = \Gamma_\alpha, \qquad \mathcal{I}_2 = \frac{Q_\alpha}{T_\alpha}, \qquad \mathcal{I}_3 = n_\alpha\left\langle V_{\parallel\alpha}B\right\rangle. \tag{2.8}$$

These transport coefficients are obtained by energy convolution of mono-energetic coefficients (Beidler *et al.* 2011) $\bar{D}_{jk}$ with a local Maxwellian

$$D_{jk} = \frac{2}{\sqrt{\pi}}\int_0^\infty \mathrm{d}z\sqrt{z}\,\mathrm{e}^{-z}\bar{D}_{jk}. \tag{2.9}$$

Presenting neoclassical flux surface averages in the form of field line averages explicitly given in field aligned variables by

$$\langle a\rangle = \lim_{\varphi_N\to\infty}\left(\int_{\varphi_0}^{\varphi_N}\frac{\mathrm{d}\varphi}{B^\varphi}\right)^{-1}\int_{\varphi_0}^{\varphi_N}\frac{\mathrm{d}\varphi}{B^\varphi}a, \tag{2.10}$$

the mono-energetic coefficients are given by

$$\bar{D}_{jk} = v\lim_{\varphi_N\to\infty}\left(\int_{\varphi_0}^{\varphi_N}\frac{\mathrm{d}\varphi}{B^\varphi}\right)^{-1}\frac{1}{4}\sum_{\sigma=\pm1}\int_{\varphi_0}^{\varphi_N}\mathrm{d}\varphi\int_0^{1/B}\mathrm{d}\eta\, s_{(j)}^\dagger g_{(k)} \equiv v\lim_{\varphi_N\to\infty}\int_{\Omega_N}\mathrm{d}\Omega\, s_{(j)}^\dagger g_{(k)}, \tag{2.11}$$

where

$$a^\dagger(\varphi,\eta,\sigma) = a(\varphi,\eta,-\sigma). \tag{2.12}$$

Definitions of thermodynamic forces and fluxes and, respectively, of diffusion coefficients (2.9) here are the same as in Kernbichler *et al.* (2016) and coincide with

https://doi.org/10.1017/S0022377825000200 Published online by Cambridge University Press

those of Beidler *et al.* (2011) for the reference field $B_0 = 1$ except for the sign of A_3. The sign convention used here results in a simple Onsager symmetry for all transport coefficients, $D_{jk} = D_{kj}$, but negative coefficient D_{33} corresponding to plasma conductivity.

For the present analysis, we solve the kinetic equation on the rational surface using a 'representative' field line where necessary conditions valid for the irrational flux surface are fulfilled. The flux surface average (2.10) at the irrational surface corresponds then to the limit of the series of representative field lines closed after N turns at respective rational surfaces, $r = r_N$, where $\iota(r_N) = M/N$, which converge to the irrational surface, $\lim_{N\to\infty} \iota(r_N) = \iota(r)$. The requested condition is Liouville's theorem, which states that the integral over any closed surface of the normal component of the guiding center velocity multiplied by the phase space Jacobian is zero for fixed total energy and the perpendicular adiabatic invariant used as phase space variables. For the magnetic surface with constant electrostatic potential, this means $\left\langle B v_g^r / v_\parallel \right\rangle = 0$, where the surface integration is performed over regions where $v_\parallel^2 = v^2(1 - \eta B) \geqslant 0$ keeping invariants z and η constant. The field line average form (2.10) of Liouville's theorem results in

$$\lim_{\varphi_N\to\infty} \left(\int_{\varphi_0}^{\varphi_N} \frac{\mathrm{d}\varphi}{B^\varphi} \right)^{-1} \int_{\varphi_0}^{\varphi_N} \frac{\mathrm{d}\varphi B v_g^r}{B^\varphi v_\parallel} = 0, \tag{2.13}$$

for passing particles and in

$$\lim_{\varphi_N\to\infty} \left(\int_{\varphi_0}^{\varphi_N} \frac{\mathrm{d}\varphi}{B^\varphi} \right)^{-1} \sum_{j=1}^{j_{\max}} \int_{\varphi_j^-}^{\varphi_j^+} \frac{\mathrm{d}\varphi B v_g^r}{B^\varphi v_\parallel} = 0, \tag{2.14}$$

for trapped particles, where $\varphi_j^-(\eta)$ and $\varphi_j^+(\eta)$ are the left and right turning points, being solutions to $\eta B(\varphi_j^\pm) = 1$, index j enumerates local magnetic field maxima $B(\varphi_j)$ fulfilling $B(\varphi_j)\eta > 1$ so that turning points are contained between maximum points φ_j and φ_{j+1}. The upper summation limit $j_{\max} = j_{\max}(\eta, N)$ is the total number of such maxima between φ_0 and φ_N. For the "representative" closed field line with φ_0 at the largest maximum we require that conditions (2.13) and (2.14) are fulfilled exactly for finite φ_N, i.e.

$$\int_{\varphi_0}^{\varphi_N} \mathrm{d}\varphi\, s_{(1)} = 0, \qquad \sum_{j=1}^{j_{\max}} \int_{\varphi_j^-}^{\varphi_j^+} \mathrm{d}\varphi\, s_{(1)} = 0, \tag{2.15}$$

for passing and trapped particles, respectively (see (2.4)). We will call these conditions "quasi-Liouville's theorem". In the devices with stellarator symmetry conditions (2.15) are satisfied for closed field lines passing through the magnetic field symmetry point φ_{sts} which is obvious due to anti-symmetry of the geodesic curvature (and, respectively, of v_g^r and $s_{(1)}$) with respect to this point, $s_{(1)}(2\varphi_{\mathrm{sts}} - \varphi) = -s_{(1)}(\varphi)$. Restricting our analysis to such devices with a single global maximum per field period, the reference field line is then the one starting from the global maximum, which must be located at one of (at least two possible) symmetry points $\varphi_0 \in \varphi_{\mathrm{sts}}$.

https://doi.org/10.1017/S0022377825000200 Published online by Cambridge University Press

Representing flux surface averages (2.10) and (2.11) by the same expressions without the limit $\varphi_N \to \infty$, one can check that so defined mono-energetic coefficients stay Onsager-symmetric. Namely, replacing source terms in (2.11) via equation (2.3), integrating by parts and using the periodicity of the distribution in the passing region, $g(\varphi_0, \eta, \sigma) = g(\varphi_N, \eta, \sigma)$ and its continuity at the turning points in the trapped region, $g(\varphi_j^{\pm}, \eta, 1) = g(\varphi_j^{\pm}, \eta, -1)$, we get

$$\bar{D}_{jk} = \int\limits_{\Omega_N} \mathrm{d}\Omega\, g_{(k)} \left(\hat{L} g_{(j)}\right)^{\dagger} = \int\limits_{\Omega_N} \mathrm{d}\Omega\, g_{(j)}^{\dagger} \hat{L} g_{(k)} = \int\limits_{\Omega_N} \mathrm{d}\Omega\, g_{(j)}^{\dagger} s_{(k)} = \bar{D}_{kj}. \quad (2.16)$$

Thus, we can either compute the bootstrap coefficient $\bar{D}_{31}$ solving the direct problem driven by $s_{(1)}$ or use its equality to the Ware-pinch coefficient $\bar{D}_{13}$ resulting from the adjoint problem driven by $s_{(3)}$.

2.2. *Collisionless asymptotic solutions*

Omitting the drive index (k), asymptotic solutions of (2.3) in the long mean free path limit $l_c \to \infty$ follow from the standard procedure where the normalized distribution function is looked for in the form of the series expansion in l_c^{-1}

$$g(\varphi, \eta, \sigma) = g_{-1}(\eta, \sigma) + g_0(\varphi, \eta, \sigma) + g_1(\varphi, \eta, \sigma) + \ldots, \quad (2.17)$$

where the leading-order term g_{-1} is independent of φ, and corrections satisfy

$$\sigma \frac{\partial g_n}{\partial \varphi} = \frac{\partial}{\partial \eta}\left(D_\eta \frac{\partial g_{n-1}}{\partial \eta}\right) + \delta_{n0} s, \qquad n \geqslant 0. \quad (2.18)$$

Equation (2.18) is integrated to

$$g_n(\varphi, \eta, \sigma) = \sigma \frac{\partial}{\partial \eta}\left(\int\limits_{\varphi_{\mathrm{beg}}}^{\varphi} \mathrm{d}\varphi' D_\eta \frac{\partial g_{n-1}}{\partial \eta}\right) + \sigma \delta_{n0} \int\limits_{\varphi_{\mathrm{beg}}}^{\varphi} \mathrm{d}\varphi' s + \bar{g}_n(\eta, \sigma), \quad (2.19)$$

where $\varphi_{\mathrm{beg}} = \varphi_j^-(\eta)$ for trapped particles and $\varphi_{\mathrm{beg}} = \varphi_0$ for passing, and we require that each of g_n is continuous at the periodic boundary and at the turning points. Continuity at $\varphi = \varphi_j^-$ means that $\bar{g}_n$ is an even function of σ in the trapped region, $\bar{g}_n = \bar{g}_n(\eta)$, while continuity at the periodic boundary in the passing region and at $\varphi = \varphi_j^+$ in the trapped region results in an equation for the integration constant $\bar{g}_{n-1}$ (solubility constraint for g_n). The leading-order constraint for g_0 gives a bounce-averaged equation for g_{-1}

$$\sum_{\sigma=\pm 1}^{\mathrm{trapped}} \left(\frac{\partial}{\partial \eta}\left(\frac{\partial g_{-1}}{\partial \eta} \int\limits_{\varphi_{\mathrm{beg}}}^{\varphi_{\mathrm{end}}} \mathrm{d}\varphi' D_\eta\right) + \int\limits_{\varphi_{\mathrm{beg}}}^{\varphi_{\mathrm{end}}} \mathrm{d}\varphi' s\right) = 0, \quad (2.20)$$

where $\varphi_{\mathrm{end}} = \varphi_j^+(\eta)$ for trapped particles and $\varphi_{\mathrm{end}} = \varphi_N$ for passing, and the sum $\sum_{\sigma=\pm 1}^{\mathrm{trapped}}$ is taken for trapped particles only. Higher-order constraints result in equations

https://doi.org/10.1017/S0022377825000200 Published online by Cambridge University Press

for integration constants $\bar{g}_n$

$$\sum_{\sigma=\pm1}^{\text{trapped}} \frac{\partial}{\partial\eta}\left(\frac{\partial\bar{g}_n}{\partial\eta}\int_{\varphi_{\text{beg}}}^{\varphi_{\text{end}}} \mathrm{d}\varphi' D_\eta + \int_{\varphi_{\text{beg}}}^{\varphi_{\text{end}}} \mathrm{d}\varphi' D_\eta \frac{\partial(g_n-\bar{g}_n)}{\partial\eta}\right)=0, \qquad n\geqslant 0, \tag{2.21}$$

where $g_n-\bar{g}_n$ is determined by g_{n-1} via (2.19).

Since boundary conditions for the collisional flux in velocity space restrict only the whole solution (2.17), we have a freedom for setting boundary conditions for individual expansion terms. Thus, we can require that this flux is produced by g_{-1} only

$$\sum_{\sigma=\pm1}^{\text{trapped}} \int_{\varphi_{\text{beg}}}^{\varphi_{\text{end}}} \mathrm{d}\varphi' D_\eta \frac{\partial g}{\partial\eta} = \sum_{\sigma=\pm1}^{\text{trapped}} \frac{\partial g_{-1}}{\partial\eta}\int_{\varphi_{\text{beg}}}^{\varphi_{\text{end}}} \mathrm{d}\varphi' D_\eta, \tag{2.22}$$

while the corrections carry no flux so that (2.21) is integrated to

$$\sum_{\sigma=\pm1}^{\text{trapped}} \left(\frac{\partial\bar{g}_n}{\partial\eta}\int_{\varphi_{\text{beg}}}^{\varphi_{\text{end}}} \mathrm{d}\varphi' D_\eta + \int_{\varphi_{\text{beg}}}^{\varphi_{\text{end}}} \mathrm{d}\varphi' D_\eta \frac{\partial(g_n-\bar{g}_n)}{\partial\eta}\right)=0, \qquad n\geqslant 0. \tag{2.23}$$

We apply this ansatz separately to the direct problem driven by source $s_{(1)}$ and to the adjoint problem driven by source $s_{(3)}$.

2.2.1. Direct problem

Due to the first condition (2.15), the bounce-averaged equation (2.20) for passing particles is homogeneous

$$\frac{\partial}{\partial\eta}\left(\frac{\partial g_{-1}}{\partial\eta}\int_{\varphi_0}^{\varphi_N} \mathrm{d}\varphi' D_\eta\right)=0. \tag{2.24}$$

Integrating it once and applying the boundary condition $\partial g_{-1}/\partial\eta=0$ at the strongly passing boundary $\eta=0$ we get $g_{-1}=\text{const.}$ in the passing region. Since g_{-1} is continuous at the global maximum point $\varphi=\varphi_0$ at the trapped–passing boundary $\eta=1/B_{\max}$, the function g_{-1} can only be even. Since any constant satisfies the homogeneous mono-energetic equation in the whole phase space making no contribution to transport coefficients but only re-defining the moments of equilibrium Maxwellian, we fix $g_{-1}=0$ in the passing region. In the trapped region, (2.20) is

$$\frac{\partial}{\partial\eta}\left(\frac{\eta I_j}{l_c}\frac{\partial g_{-1}}{\partial\eta}+H_j\right)=0, \tag{2.25}$$

where we denoted

$$I_j(\eta)=\int_{\varphi_j^-(\eta)}^{\varphi_j^+(\eta)} \mathrm{d}\varphi\frac{|\lambda|}{B^\varphi}, \qquad H_j(\eta)=\int_{\varphi_j^-(\eta)}^{\varphi_j^+(\eta)} \mathrm{d}\varphi H'_\varphi, \tag{2.26}$$

https://doi.org/10.1017/S0022377825000200 Published online by Cambridge University Press

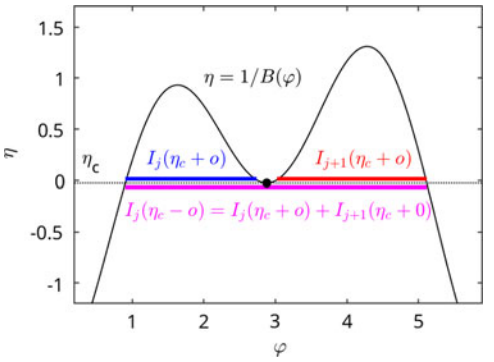

FIGURE 1. Example of class-transition boundary introduced by local field maximum $B_{\max}^{\mathrm{loc}}$ (black dot) where three types of trapped particles meet (two "single-trapped" and one "double-trapped"). Boundary conditions (2.28) are fulfilled by (2.27) due $H_j(\eta_c - o) = H_j(\eta_c + o) + H_{j+1}(\eta_c + o)$.

see definitions (2.3)–(2.5). Since $\partial g_{-1}/\partial\eta = 0$ at the bottoms of local magnetic wells $\eta = 1/B_{\min}^{\mathrm{loc}}$ where $H_j = 0$ due to $\varphi_j^+ = \varphi_j^-$ we can integrate (2.25) to

$$\frac{\partial g_{-1}(\eta)}{\partial\eta} = -\frac{l_c H_j}{\eta I_j}. \tag{2.27}$$

This solution automatically satisfies collisional flux conservation relations in all boundary layers separating different trapped particle classes

$$\left[I_j \frac{\partial g_{-1}^{(j)}}{\partial\eta}\right]_{\eta=\eta_c-o} = \left[I_j \frac{\partial g_{-1}^{(j)}}{\partial\eta}\right]_{\eta=\eta_c+o} + \left[I_{j+1} \frac{\partial g_{-1}^{(j+1)}}{\partial\eta}\right]_{\eta=\eta_c+o}, \tag{2.28}$$

where $\eta_c = 1/B_{\max}^{\mathrm{loc}}$, see figure 1, o denotes an infinitesimal number and the superscript (j) on g_{-1} denotes particle type trapped between the reflection points $\varphi_j^{\pm}$. Derivative (2.27) satisfies also the flux conservation through the trapped–passing boundary $\eta = \eta_b$ turning there to zero, because only a single type of trapped particles exists near this boundary, and $H_1(\eta_b + o) = 0$ follows then from the second condition (2.15).

Solution (2.27) is sufficient for the computation of the effective ripple (Nemov *et al.* 1999) $\varepsilon_{\mathrm{eff}}$ which determines device geometry effect on the mono-energetic diffusion coefficient $\bar{D}_{11}$ (and all other $\bar{D}_{jk}$ for $j, k \leqslant 2$ trivially related to $\bar{D}_{11}$). Substituting in (2.11) $g_{(1)} = g_{-1}$ and $s_{(1)}$ via (2.4), integrating the result by parts over η and using the continuity of g_{-1} through all boundary layers, changing the integration order over φ and η results in

$$\bar{D}_{11} = \frac{v l_c}{2}\left(\int_{\varphi_0}^{\varphi_N} \frac{\mathrm{d}\varphi}{B^{\varphi}}\right)^{-1} \int_{\eta_b}^{\eta_m} \mathrm{d}\eta \sum_{j=1}^{j_{\max}(\eta,N)} \frac{H_j^2}{\eta I_j} = \frac{4\sqrt{2}}{9\pi} \frac{v l_c \rho_L^2 B^2}{R_0^2 B_0^2} \varepsilon_{\mathrm{eff}}^{3/2}, \tag{2.29}$$

where $\eta_b = 1/B_{\max}$ and $\eta_m = 1/B_{\min}$ are defined by global field maximum and minimum, respectively. The last equality (2.29) where R_0 and B_0 are reference values of major radius and magnetic field, respectively, defines $\varepsilon_{\mathrm{eff}}^{3/2}$ in the same way as

https://doi.org/10.1017/S0022377825000200 Published online by Cambridge University Press

equation (29) of Nemov *et al.* (1999), where quantities $\hat{I}_j(b')$ and $\hat{H}_j(b')$ are related to the present notation by $\hat{I}_j = I_j$ and $\hat{H}_j = 3B_0^{3/2}\eta^{1/2}(\rho_L B)^{-1}H_j$ with $b' = (B_0\eta)^{-1}$.

For the next-order correction g_0, we notice that the first two terms in the right-hand side of (2.19) are odd in σ. Therefore, in the trapped particle region, equation (2.23) for the integration constant (which can only be even there) is homogeneous, resulting in $\bar{g}_0 = \text{const}$. Due to the continuity of the distribution function across the trapped–passing boundary, the integration constant in the passing region is the same. We can again absorb this constant into the equilibrium Maxwellian, as we have already done in the previous order when setting $g_{-1} = 0$ in the passing region. Thus, substituting in (2.19) the derivative $\partial g_{-1}/\partial\eta$ via (2.27) and the source $s = s_{(1)}$ via (2.4) and (2.5) we get explicitly

$$g_0(\varphi, \eta, \sigma) = \sigma \frac{\partial}{\partial \eta} \int\limits_{\varphi_j^-(\eta)}^{\varphi} \mathrm{d}\varphi' \left(H'_\varphi(\varphi', \eta) - \frac{|\lambda(\varphi', \eta)|}{B^\varphi(\varphi')} \frac{H_j(\eta)}{I_j(\eta)} \right), \tag{2.30}$$

where we have exchanged the derivative over η with integration in the first term using $H'_\varphi(\varphi_j^-(\eta), \eta) = 0$. It should be noted now that the integral over φ' is a discontinuous function of η at the boundaries between classes $\eta = \eta_c$ where either $\varphi_j^-(\eta)$ or $\varphi_j^+(\eta)$ jumps. Respectively, the function g_0 contains a δ-function $\delta(\eta - \eta_c)$, which is required by particle conservation in the boundary layer. Namely, integrating (2.3) over η across the boundary, we get

$$\sigma \int\limits_{\eta_c - o}^{\eta_c + o} \mathrm{d}\eta \frac{\partial g}{\partial \varphi} = D_\eta(\varphi, \eta) \frac{\partial g(\varphi, \eta)}{\partial \eta} \Bigg|_{\eta = \eta_c - o}^{\eta = \eta_c + o}. \tag{2.31}$$

Substituting here $g = g_{-1} + g_0$ and ignoring g_0 on the right-hand side where its contribution is linear in collisionality we get

$$\sigma \frac{\partial}{\partial \varphi} \int\limits_{\eta_c - o}^{\eta_c + o} \mathrm{d}\eta\, g_0(\varphi, \eta, \sigma) = \frac{|\lambda(\varphi, \eta_c)|}{B^\varphi(\varphi)} \left(\frac{H_j(\eta_c - o)}{I_j(\eta_c - o)} - \frac{H_j(\eta_c + o)}{I_j(\eta_c + o)} \right), \tag{2.32}$$

which is an identity for g_0 in the form (2.30).

In the passing region where $g_{-1} = 0$, (2.19) results in

$$g_0 = \sigma \frac{\partial}{\partial \eta} \int\limits_{\varphi_0}^{\varphi} \mathrm{d}\varphi' H'_\varphi(\varphi', \eta) + \bar{g}_0, \tag{2.33}$$

where

$$\frac{\partial \bar{g}_0}{\partial \eta} = -\frac{\sigma}{\langle |\lambda| \rangle} \left\langle |\lambda| \frac{\partial^2}{\partial \eta^2} \int\limits_{\varphi_0}^{\varphi} \mathrm{d}\varphi' H'_\varphi(\varphi', \eta) \right\rangle, \tag{2.34}$$

follows from (2.23) and $\langle \ldots \rangle$ denotes a field line average (flux surface average (2.10) with φ_N kept finite). This derivative has an integrable singularity at the trapped–passing boundary, $\partial \bar{g}_0/\partial\eta \propto (\eta_b - \eta)^{-1/2}$ which follows from $|\nabla r| k_G \propto (\varphi - \varphi_0)$ near the global maximum $\varphi = \varphi_0$ (and $\varphi = \varphi_N$ since the innermost integral is a single-valued (periodic) function of φ on the closed field line). Therefore,

https://doi.org/10.1017/S0022377825000200 Published online by Cambridge University Press

$\bar{g}_0$ is continuous at the trapped–passing boundary, where it is connected to $\bar{g}_0 = 0$ in the trapped region. Moreover, the derivative of the full solution $\partial g_0/\partial\eta$ has no singularity at this boundary (in contrast to $\partial\bar{g}_0/\partial\eta$). One can also check that this derivative does not depend on the lower integration limit φ_0 in (2.33) and (2.34) which, therefore, needs not to be the global maximum point.

We can formally combine expressions (2.30) and (2.33) into

$$g_0(\varphi,\eta,\sigma) = \sigma\frac{\partial}{\partial\eta}\int\limits_{\varphi_{\rm beg}}^{\varphi} \mathrm{d}\varphi'\left(H'_\varphi(\varphi',\eta) - \frac{|\lambda(\varphi',\eta)|}{B^\varphi(\varphi')}\frac{H_j(\eta)}{I_j(\eta)}\right) + \bar{g}_0(\eta,\sigma), \tag{2.35}$$

valid for the whole phase space with $I_j = I_0$ and $H_j = H_0 = 0$ in the passing region where they are given by (2.26) with the limits φ_0 and φ_N instead of $\varphi_j^{\pm}$. Due to the linear scaling of g_0 with velocity module v, we can evaluate energy integral in the expression for the parallel current density of the α species substituting in (2.1) $g = g_0$ which is the only term contributing in the leading order

$$j_{\parallel\alpha} = e_\alpha\int \mathrm{d}^3v v_\parallel(f - f_M) = C_\alpha B\sum_{\sigma=\pm1}\sigma\int\limits_0^{1/B}\mathrm{d}\eta\, g_0, \tag{2.36}$$

where

$$C_\alpha = \frac{3c}{4B\rho_L}\left(\frac{\partial p_\alpha}{\partial r} - e_\alpha n_\alpha E_r\right), \qquad p_\alpha = n_\alpha T_\alpha, \tag{2.37}$$

and we omitted the inductive current by setting $A_3 = 0$. Since g_0/ρ_L is independent of particle species, total current density is independent of E_r in quasi-neutral plasmas,

$$j_\parallel = \sum_\alpha j_{\parallel\alpha} = C_\parallel B\sum_{\sigma=\pm1}\sigma\int\limits_0^{1/B}\mathrm{d}\eta\, g_0 = C_\parallel B\sum_{\sigma=\pm1}\sigma\int\limits_0^{1/B}\mathrm{d}\eta\left(g_0 - \bar{g}_0 - \eta\frac{\partial\bar{g}_0}{\partial\eta}\right), \tag{2.38}$$

where

$$C_\parallel = C_\parallel(r) = \frac{1}{\rho_L}\sum_{\alpha'}C_{\alpha'}\rho'_L = \frac{3c}{4B\rho_L}\frac{\partial p}{\partial r}, \qquad p = \sum_\alpha p_\alpha, \tag{2.39}$$

where ρ'_L denotes the Larmor radius of α' species, and we used the condition $\bar{g}_0 = 0$ at the boundary $\eta = 1/B$ when integrating by parts in the last expression (2.38). According to (2.35), the term $g_0 - \bar{g}_0$ is a derivative which contributes only at the lower limit $\eta = 0$ where using explicitly (2.5) one gets parallel equilibrium current density as

$$j_\parallel = -2cB\frac{\partial p}{\partial r}\int\limits_{\varphi_0}^{\varphi}\mathrm{d}\varphi'\frac{|\nabla r|k_G}{BB^\varphi} - C_\parallel B\sum_{\sigma=\pm1}\sigma\int\limits_0^{\eta_b}\mathrm{d}\eta\,\eta\frac{\partial\bar{g}_0}{\partial\eta} = j_{\rm PS} + j_b. \tag{2.40}$$

Here, as well as in (2.34), the point φ_0 must be at a global maximum because integration over η in the first term required the continuity of $\varphi_{\rm beg}$ at the trapped–passing boundary. Equation (2.40) naturally agrees with the ideal magnetohydrodynamic

https://doi.org/10.1017/S0022377825000200 Published online by Cambridge University Press

radial force balance which determines the Pfirsch–Schlüter current density j_{PS} up to the arbitrary constant times B. Due to quasi-Liouville's theorem (2.15), the current density (2.40) is periodic, $j_\parallel(\varphi_N) = j_\parallel(\varphi_0)$, so that the last expression (2.6) for the geodesic curvature leads to

$$\frac{\partial}{\partial \vartheta_0} \int_{\varphi_0}^{\varphi_N} \frac{\mathrm{d}\varphi}{B^\varphi} = 0, \tag{2.41}$$

which is a "true" rational surface condition (Solov'ev & Shafranov, 1970). Using the explicit form of H'_φ in (2.34) and taking the flux "surface average" (2.10) of $j_\parallel B$ thus eliminating the Pfirsch–Schlüter current which is driven solely by charge separation potential and, therefore, must satisfy $\langle j_{\mathrm{PS}} B\rangle = 0$, we finally obtain the bootstrap current density j_b which scales with B as

$$\langle j_\parallel B\rangle = j_b \frac{\langle B^2\rangle}{B} = -c\lambda_{bB}\frac{\partial p}{\partial r}. \tag{2.42}$$

Here, λ_{bB} is the dimensionless geometrical factor λ_b given by equation (9) of Nemov *et al.* (2004) in the case of normalization field $B_0 = \langle B^2\rangle^{1/2}$

$$\lambda_{bB} = \left\langle 2B^2 \int_{\varphi_0}^{\varphi} \mathrm{d}\varphi' \frac{|\nabla r| k_G}{B B^\varphi} + \frac{3\langle B^2\rangle}{8} \int_0^{\eta_b} \mathrm{d}\eta \frac{\eta^2 |\lambda|}{\langle |\lambda|\rangle} \int_{\varphi_0}^{\varphi} \mathrm{d}\varphi' \frac{|\nabla r| k_G B^2}{|\lambda|^3 B^\varphi} \right\rangle, \tag{2.43}$$

with $\langle \ldots \rangle$ given for a closed field line by (2.10) with finite φ_N. It is convenient to express it via the mono-energetic bootstrap coefficient (2.11)

$$\lambda_{bB} = \frac{3\bar{D}_{31}}{v\rho_L B}, \tag{2.44}$$

in order to use it also for finite collisionality.

The separate contribution of trapped particle region to λ_{bB} is obtained by replacement of the lower integration limit in (2.38) from 0 to $\eta_b + o$

$$\lambda^{tr}_{bB} = \left\langle B^2 \int_{\varphi_0}^{\varphi} \mathrm{d}\varphi' \frac{|\nabla r| k_G}{2B B^\varphi} \lambda_b (3 + \lambda_b^2) \right\rangle, \qquad \lambda_b = \sqrt{1 - \eta_b B}. \tag{2.45}$$

In the usual case of small magnetic field modulation amplitude $\varepsilon_M \ll 1$, this contribution is of the order $\varepsilon_M^{1/2}$ as compared with the first term in (2.43) and is of the order ε_M as compared with the second term. Therefore, it can be ignored (Boozer & Gardner 1990) as long as an exact compensation of bootstrap current, $\lambda_{bB} = 0$, is not looked for.

The factor (2.43) matches the result of Shaing and Callen, which is a natural consequence of using the same method. Namely, $\lambda_{bB} = (1 - f_c)\langle \tilde{G}_b\rangle / S$ where $S = \mathrm{d}V/\mathrm{d}r$ is the flux surface area, fraction of circulating particles f_c is given by equation (56) of Shaing & Callen (1983), and geometrical factor $\tilde{G}_b$ is given there by equations (75*b*) and (60*c*). In the case of negligible toroidal equilibrium current, $B_\vartheta = 0$, the result of Boozer & Gardner (1990) is also approximately recovered,

https://doi.org/10.1017/S0022377825000200 Published online by Cambridge University Press

$\lambda_{bB} = \Delta_0 B_\varphi \, \mathrm{d}r/\, \mathrm{d}\psi + O(\varepsilon_\mathrm{M})$, where the quantity Δ_0 is given by equations (51), (53) and (54) of Boozer & Gardner (1990), ignoring the small trapped particle contribution and other corrections linear in ε_M (in the case of a circular tokamak, $\lambda_{bB} \approx A\Delta_0$ where A is the aspect ratio).

Note that the trapped particle distribution function here is formally the same as the one given in the implicit form by equation (54) of Shaing & Callen (1983) omitting there the ripple plateau contribution absent in our case where we ignored banana precession (cross-field drift within flux surfaces) already in the starting equation (2.3). On the other hand, we obtained also the explicit expression for its odd part, (2.35), which is demonstrative for the distribution of the parallel equilibrium current in the velocity space. It can be seen that a significant part of this current (essentially of the Pfirsch–Schlüter current) flows in the boundary layers between trapped particle classes (but not in the main, trapped–passing boundary layer). The origin of these localized currents is the same as the origin of the Pfirsch–Schlüter current in all devices, i.e. they remove charge separation introduced by the radial particle drift. However, in contrast to tokamaks (and tokamak-like part of the current in stellarators) where compensation currents are produced in a long mean free path regime within a single turn of particle bounce motion due to the finite radial displacement during this time, localized currents serve to compensate charge separation by finite bounce-averaged drift, which accumulates on much longer collisional detrapping time. Interpreting the source term $s_{(1)}$, (2.4), in the regions where it is positive as a source of 'particles' and where it is negative as a source of 'anti-particles' whose total amount generated at the flux surface is the same as the amount of 'particles', being a consequence of quasi-Liouville's theorem (2.15), we see that particles (or anti-particles) accumulated in the local ripple wells due to the finite bounce-averaged drift, $H_j \neq 0$, can only leave the wells due to collisional scattering flux through the class boundaries (see figure 1). Since local collisional flux density generally needs not be continuous at this boundary, $\partial g_{-1}(\eta - o)/\partial\eta \neq \partial g_{-1}(\eta + o)/\partial\eta$, a significant amount of particles (anti-particles) is re-distributed through the boundary layers, which is manifested by the δ-like behavior of g_0, (2.35), being, up to a factor, a parallel flow density in velocity space.

The asymptotic series expansion (2.17) can be continued to the next order, leading to the correction g_1. This correction, however, has a non-integrable singularity at class-transition boundaries, $g_1 \propto (\eta - \eta_c)^{-2}$ (in contrast to integrable singularity of $g_0 \propto \log|\eta - \eta_c|$), which is a consequence of finite geodesic curvature at respective local field maxima. Therefore, contributions of different order corrections to the collisional flux density in the matching conditions (2.31) become comparable at finite collisionality for $|\eta - \eta_c| = \delta\eta \propto l_c^{-1/2} \propto \nu^{1/2}$, where $\partial g_0(\eta)/\partial\eta \sim \delta\eta^{-1}$ and $\partial g_1(\eta)/\partial\eta \sim l_c^{-1}\delta\eta^{-3}$. In other words, the expansion (2.17) breaks down at the edge of the boundary layer of width $\delta\eta$. Respectively, matching interval o in (2.28), which is an infinitesimal for vanishing collisionality, should satisfy $\delta\eta \ll o \ll \eta$ for finite collisionality, which means that the error of the asymptotic solution scales with $\sqrt{\nu}$ rather than with ν. Since the particle–anti-particle re-distribution flux manifested by δ-functions in asymptotic expression (2.35) for g_0 is independent of collisionality, we can estimate the odd part of the distribution function which carries this flux in the class-transition boundary layers as $g^{\mathrm{odd}} \propto \delta\eta^{-1} \propto l_c^{1/2} \propto \nu^{-1/2}$.

As shown below, the presence of these strong parallel flows in class-transition boundary layers is actually responsible for the 'anomalous' behavior of the bootstrap current at finite collisionality.

https://doi.org/10.1017/S0022377825000200 Published online by Cambridge University Press

2.2.2. Adjoint problem

The asymptotic solution of the adjoint problem has been derived by Helander *et al.* (2011) omitting in the correction g_0, which determines particle flux, the φ independent part $\bar{g}_0$ which does not contribute to this flux and, respectively, is not needed for the Ware-pinch coefficient. Here, we extend this derivation in order to obtain the complete even part of this correction useful for the interpretation of numerical examples in the following sections. The leading-order asymptotic solution is odd in σ and is given by the bounce-averaged equation (2.20) for the source $s_{(3)}$, see (2.4), with the same boundary conditions as previously as

$$g_{-1} = \sigma \int_{\varphi_0}^{\varphi_N} \mathrm{d}\varphi \, \frac{B^2}{B^\varphi} \int_{\eta}^{\eta_b} \mathrm{d}\eta' \, \eta' \left(\int_{\varphi_0}^{\varphi_N} \mathrm{d}\varphi \, D_\eta \right)^{-1} = \sigma l_c \int_{\eta}^{\eta_b} \mathrm{d}\eta' \, \frac{\langle B^2 \rangle}{\langle |\lambda| \rangle}, \tag{2.46}$$

in the passing region, and $g_{-1} = 0$ in the trapped region. The next-order correction results from (2.19) in the trapped region in

$$g_0(\varphi, \eta) = \sigma \int_{\varphi_j^-}^{\varphi} \mathrm{d}\varphi' s_{(3)} + \bar{g}_0(\eta) = \int_{\varphi_j^-}^{\varphi} \mathrm{d}\varphi' \frac{B^2}{B^\varphi} + \bar{g}_0(\eta) = \int_{\varphi_b}^{\varphi} \mathrm{d}\varphi' \frac{B^2}{B^\varphi} \equiv g_0^t(\varphi), \tag{2.47}$$

where we integrated (2.23)

$$\frac{\partial \bar{g}_0}{\partial \eta} = \frac{B^2(\varphi_j^-)}{B^\varphi(\varphi_j^-)} \frac{\partial \varphi_j^-}{\partial \eta}, \tag{2.48}$$

from the trapped–passing boundary and included an arbitrary integration constant into the lower integration limit φ_b being, therefore, an arbitrary constant too. This constant is the same for all classes due to continuity of g_0 at class-transition boundaries.

In the passing region, solutions of (2.19) and (2.23) result in

$$g_0(\varphi, \eta) = \int_{\varphi_b}^{\varphi} \mathrm{d}\varphi' \left(\frac{B^2}{B^\varphi} - \frac{\partial}{\partial \eta} \frac{\eta \langle B^2 \rangle}{\langle |\lambda| \rangle} \frac{|\lambda|}{B^\varphi} \right) + \bar{g}_0(\eta), \tag{2.49}$$

where

$$\bar{g}_0(\eta) = \int_0^{\eta} \frac{\mathrm{d}\eta'}{\langle |\lambda| \rangle} \left\langle |\lambda| \frac{\partial^2}{\partial \eta'^2} \frac{\eta' \langle B^2 \rangle}{\langle |\lambda| \rangle} \int_{\varphi_b}^{\varphi} \mathrm{d}\varphi' \frac{|\lambda|}{B^\varphi} \right\rangle + C_\sigma, \tag{2.50}$$

and where C_σ are different integration constants of (2.23) for $\sigma = \pm 1$. Similar to the solution of the direct problem, derivative $\partial g_0 / \partial \eta$ of the function (2.49) does not depend on φ_b in the passing region. Actually, the lower integration limit φ_b in (2.49) and (2.50) enters g_0 via a periodic function of φ_b which adds up to the integration constant C_σ (this follows from explicit evaluation of $\partial g_0 / \partial \varphi_b = \left(\langle B^2 \rangle - B^2(\varphi_b) \right) / B^\varphi(\varphi_b)$ whose integral over the whole range $\varphi_0 < \varphi_b < \varphi_N$ is zero).

https://doi.org/10.1017/S0022377825000200 Published online by Cambridge University Press

Function g_0 has an integrable logarithmic singularity at the trapped–passing boundary, $g_0 \propto \log(\eta_b - \eta)$, in particular, due to such singularity of $\partial\langle|\lambda|\rangle/\partial\eta$ which, up to a constant factor, is a bounce time. Next-order correction shows again that series expansion breaks down in the boundary layer, $|\eta_b - \eta| \leqslant \delta\eta \propto l_c^{-1/2}$.

In order to fully determine g_0 in the whole phase space we must express three integration constants, φ_b and C_σ, via a single constant which is the only degree of freedom re-defining an equilibrium Maxwellian. For that, we must match the solutions through the trapped–passing boundary where g_0 is singular, but first it is convenient to split g_0 into even and odd parts in σ, $g_0 = g_0^{\rm even} + g_0^{\rm odd}$, where $g_0^{\rm even}$ is given by (2.47)–(2.50) with replacement of C_σ by a constant $C_{\rm even}$ and $g_0^{\rm odd} = \sigma C_{\rm odd}\Theta(\eta_b - \eta)$, where $\Theta(x)$ is a Heaviside step function, and $C_{\rm odd}$ is another constant.

Function $g_0^{\rm odd}$ is of no interest in the following since it does not contribute to the Ware pinch but only provides a correction to the leading-order solution (2.46). As for $g_0^{\rm even}$, we still need to determine it formally in the boundary layer identifying there its most singular part. For this purpose, we take the odd part of (2.3) and, similar to (2.32), and integrate it across the boundary layer ignoring the contribution of the source term and retaining only the leading-order solution (2.46) in the collisional flux through the boundaries of integration domain

$$\frac{\partial}{\partial\varphi}\int\limits_{\eta_b-\Delta\eta}^{\eta_b+\Delta\eta} {\rm d}\eta\, g_0^{\rm even}(\varphi,\eta) = \left(\frac{\eta\langle B^2\rangle}{\langle|\lambda|\rangle}\frac{|\lambda|}{B^\varphi}\right)_{\eta=\eta_b-\Delta\eta} \to \left(\frac{\eta\langle B^2\rangle}{\langle|\lambda|\rangle}\frac{|\lambda|}{B^\varphi}\right)_{\eta=\eta_b}. \tag{2.51}$$

Here, $\delta\eta \ll \Delta\eta \ll \eta_b$, $\delta\eta$ is the boundary layer width and the last expression corresponds to the collisionless limit $\Delta\eta \to 0$. Thus $g_0^{\rm even}$ can be formally presented near the trapped passing boundary as

$$g_0^{\rm even} = \delta(\eta_b - \eta)\left(\int\limits_{\varphi_b}^{\varphi} {\rm d}\varphi' \frac{\eta\langle B^2\rangle}{\langle|\lambda|\rangle}\frac{|\lambda|}{B^\varphi} + C_{\rm bou}\right) + o(\delta\eta^{-1}), \tag{2.52}$$

where $C_{\rm bou}$ is yet another integration constant, and the last term provides a vanishing contribution to the η-integral in (2.51). Similar to the passing particle solution (2.49), which is defined for the whole closed field line and which is a periodic function of φ with period $\varphi_N - \varphi_0$, boundary layer solution (2.52) is formally defined for the whole field period too and must be a periodic function as well. In order to be periodic, function (2.52) must be discontinuous over the variable φ, and the only point where a jump restoring the periodicity is possible, as we see below, is the global maximum point $\varphi = \varphi_0$ (and $\varphi = \varphi_N$). This discontinuity requirement leads to a certain paradox because, according to (2.3), the distribution function is continuous with φ everywhere in the range where $\eta B(\varphi) < 1$, which includes the whole trapped–passing boundary approached from the passing side, $\eta = \eta_b - 0$, which in turn seems to contradict the discontinuity of the function (2.52). To resolve this paradox, we note that a formal representation with a δ-function actually assumes a small but finite width of the boundary layer, which is partly located in the passing particle region where the distribution is strictly continuous with φ, and partly in the trapped particle region where it is continuous too except a small forbidden region with $\eta B(\varphi) > 1$ located near the global maximum. Discontinuity of $g_0^{\rm even}$ within this trapped part

https://doi.org/10.1017/S0022377825000200 Published online by Cambridge University Press

of the boundary layer is sufficient to provide the required jumps restoring the periodicity.

Similarly to the boundary layer, the periodicity argument means for the trapped particle distribution that its integral form (2.47) determined via φ_b from the interval $\varphi_0 < \varphi_b < \varphi_N$ can be used only in the same interval, $\varphi_0 < \varphi < \varphi_N$. Thus, an extension of (2.47) and (2.51) to the infinite φ range is obtained replacing there the lower integration limit φ_b with $\varphi_b + (\varphi_N - \varphi_0)\,[(\varphi - \varphi_0)/(\varphi_N - \varphi_0)]$, where $[\ldots]$ denotes the integer part. As already mentioned above, the passing particle solution (2.49) is valid for the infinite φ range as is. We can actually combine all these periodic solutions for g_0^{even} in one multiplying so extended trapped particle solution (2.47) with $\Theta(\eta - \eta_b)$, adding an even part of the passing particle solution (2.49) multiplied with $\Theta(\eta_b - \eta)$ and then adding an extended boundary layer solution (2.52).

In order to eliminate from such a combined solution, all but one unknown constants out of three, φ_b, C_{even} and C_{bou}, we use the stellarator symmetry of our closed field line such that $B(2\varphi_s - \varphi) = B(\varphi)$ and $B^\varphi(2\varphi_s - \varphi) = B^\varphi(\varphi)$, where φ_s is a symmetry point. We use the fact that the stellarator-symmetric part of the generalized Spitzer function $g = g_{(3)}$ given by $g_{\text{sym}}(\varphi, \eta, \sigma) \equiv (g(\varphi, \eta, \sigma) + g^*(\varphi, \eta, \sigma))/2$ with $g^*(\varphi, \eta, \sigma) \equiv g(2\varphi_s - \varphi, \eta, -\sigma)$ can only be a constant. Namely, it can be checked that g^* satisfies the same (2.3) but with an opposite sign of the source $s_{(3)}$ and, therefore, $g^* = -g + C$, where C is an arbitrary constant. Thus, $g_{\text{sym}} = C/2$ in the whole phase space. Introducing now a stellarator-antisymmetric part of the distribution function, $g_{\text{asym}}(\varphi, \eta, \sigma) \equiv (g(\varphi, \eta, \sigma) - g^*(\varphi, \eta, \sigma))/2$, we can split our solution g_0^{even} into stellarator-symmetric and stellarator-antisymmetric parts, $g_0^{\text{even}} = g_{\text{sym}}^{\text{even}} + g_{\text{asym}}^{\text{even}}$. Thus, we obtain that stellarator-antisymmetric part of the combined g_0^{even} does not contain any unknown and is determined by

$$g_{\text{asym}}^{\text{even}}(\varphi, \eta) = \int_{\varphi_s}^{\varphi} \mathrm{d}\varphi' \left(\frac{B^2}{B^\varphi} - \frac{\partial}{\partial \eta} \left(\Theta(\eta_b - \eta) \frac{\eta \langle B^2 \rangle}{\langle |\lambda| \rangle} \frac{|\lambda|}{B^\varphi} \right) \right), \tag{2.53}$$

where φ_s is fixed now to a second stellarator symmetry point $\varphi_s = (\varphi_0 + \varphi_N)/2$ which necessarily exists besides the global maximum point φ_0. Solution (2.53) is given here only for $\varphi_0 < \varphi < \varphi_N$ and can be extended to the infinite φ range replacing there φ_s with $\varphi_s + (\varphi_N - \varphi_0)\,[(\varphi - \varphi_0)/(\varphi_N - \varphi_0)]$. Such an extended expression is stellarator antisymmetric with respect to symmetry points of both kinds (in particular, anti-symmetry with respect to field maximum points $\varphi_0 + k(\varphi_N - \varphi_0)$, where k are integers is enabled by the discontinuity of the extended lower integration limit at those points) and is independent of an arbitrary constant φ_b.

In turn, all the unknown constants enter the stellarator-symmetric part of the combined solution g_0^{even} which is of the form

$$\begin{aligned} g_{\text{sym}}^{\text{even}} = &\int_{\varphi_b}^{\varphi_s} \mathrm{d}\varphi' \frac{B^2}{B^\varphi} + \Theta(\eta_b - \eta) \left(C_{\text{even}} - \int_{\varphi_b}^{\varphi_s} \mathrm{d}\varphi' \frac{\langle B^2 \rangle}{B^\varphi} \right) \\ &+ \delta(\eta_b - \eta) \left(\int_{\varphi_b}^{\varphi_s} \mathrm{d}\varphi' \frac{\eta \langle B^2 \rangle}{\langle |\lambda| \rangle} \frac{|\lambda|}{B^\varphi} + C_{\text{bou}} \right). \end{aligned} \tag{2.54}$$

Since this function can only be a constant, we must set C_{even} and C_{bou} so that they annihilate respective brackets multiplying the Heaviside function and δ-function

https://doi.org/10.1017/S0022377825000200 Published online by Cambridge University Press

which permits setting $\eta = \eta_b$ in the sub-integrand in the latter bracket. Finally, the remaining first term can be, as usual, absorbed into the equilibrium Maxwellian so that the whole final solution $g_0^{\text{even}} = g_{\text{asym}}^{\text{even}}$ is given by (2.53). The only difference of this solution from equation (12) of Helander *et al.* (2011) is the lower integration limit φ_s which is the second symmetry point (usually global minimum) instead of a global maximum point φ_0.

Substituting (2.46) and (2.53) for $g_{(3)} = g_{-1} + g_0$ in (2.11) we obtain the mono-energetic Ware-pinch coefficient as

$$\bar{D}_{13} = \frac{1}{3} v \rho_L B \lambda_{bB}^{\dagger}, \tag{2.55}$$

with the geometrical factor given by

$$\lambda_{bB}^{\dagger} = \frac{1}{2} \left\langle \int_0^{1/B} \mathrm{d}\eta \, g_0^{\text{even}} \frac{|\nabla r| k_G}{B} \frac{\partial}{\partial \eta} \left(3|\lambda| + |\lambda|^3 \right) \right\rangle. \tag{2.56}$$

Exchanging in this expression the integration order over η and φ and integrating by parts over φ within the motion domains $\varphi_{\text{beg}}(\eta) < \varphi < \varphi_{\text{end}}(\eta)$ we use conditions (2.15) to eliminate contribution from the integration limits. Thus, only the derivative $\partial g_0 / \partial \varphi$ can contribute. Integrating the result by parts over η in the term with $\Theta(\eta_b - \eta)$, one finally obtains $\lambda_{bB}^{\dagger} = \lambda_{bB}$ given by (2.43).

It should be noted that, in contrast to the solution of the direct problem, the solution of the adjoint problem (2.53) is regular at all class-transition boundaries and has a δ-like behavior only in the boundary layer at the trapped–passing boundary where finite collisionality scaling of g^{even} is $g^{\text{even}} \sim l_c^{1/2} \sim \nu^{-1/2}$. As shown below, interaction of this boundary layer with locally trapped particle domains is responsible for the 'anomalous' behavior of the Ware-pinch coefficient at finite collisionalities.

2.3. *Finite collisionality, numerical examples*

For the numerical tests, we use the drift kinetic equation solver NEO-2 (Kernbichler *et al.* 2008; Kasilov *et al.* 2014; Martitsch *et al.* 2016; Kernbichler *et al.* 2016; Kapper *et al.* 2016, 2018), which, generally, employs a full linearized collision operator including the relativistic effects (Kapper *et al.* 2018). Here, we restrict its collision operator to the Lorentz model only. The magnetic field model corresponds to a circular tokamak with concentric flux surfaces ($\beta = 0$) and with a toroidal ripple-like perturbation, given in Boozer coordinates by

$$B(r, \vartheta, \varphi) = B_0(r, \vartheta) \left(1 + \varepsilon_M \frac{B_0^2(r, \vartheta)}{B_{00}^2(r)} \cos(n\varphi) \right)^{-1/2}. \tag{2.57}$$

Here, $B_0(r, \vartheta)$ is the unperturbed field, $B_{00}(r)$ is the $(m, n) = (0, 0)$ harmonic of this field and ε_M is the modulation amplitude. It can be checked that this field fulfills "true surface" condition (2.41) at all rational flux surfaces, which is a property useful for the studies of bootstrap resonances briefly discussed in § 4.1. We fix $n = 3$ and $\varepsilon_M = 0.1$ and consider two cases of the rotational transform $\iota = 1/q$ with $\iota = 1/4$ and $\iota = 2/5$, where the field line is closed after one and two poloidal turns, respectively.

The normalized bootstrap coefficient (2.44) computed by NEO-2 for the above two cases as a function of the normalized collisionality $\nu_* = \pi R \nu_\perp / v = \pi R / (2 l_c) =$

https://doi.org/10.1017/S0022377825000200 Published online by Cambridge University Press

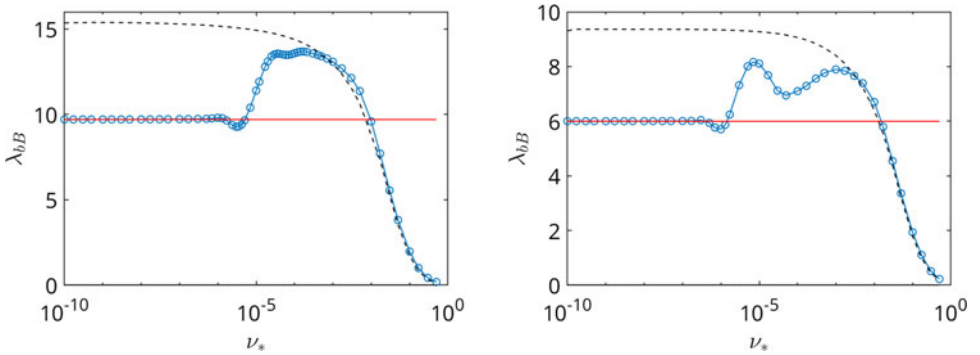

FIGURE 2. Geometrical factor λ_{bB} computed by NEO-2 (blue) for different normalized collisionalities ν_* and computed from the Shaing–Callen limit (2.43) evaluated by NEO (red) for $\iota = 1/4$ (left) and $\iota = 2/5$ (right). Black dashed lines show the result of NEO-2 for axisymmetric fields ($\varepsilon_M = 0$).

$\pi\iota\nu^*$, where R is the major radius of the magnetic axis and ν^* is the definition of Beidler *et al.* (2011), is compared with the Shaing–Callen limit (2.43) in figure 2. (The latter asymptotic limit is computed here using the code NEO (Nemov *et al.* 1999, 2004), which should not be confused with the drift kinetic code of Belli and Candy (Belli & Candy 2015) having the same name.) It can be seen that the asymptotic value is abruptly reached in both cases at rather low collisionalities $\nu_* \sim 10^{-6}$ with the collisional λ_{bB} dropping briefly below the Shaing–Callen limit prior to convergence. Naturally, the normalized Ware-pinch coefficient $\lambda^{\dagger}_{bB}$, (2.55), differs from bootstrap coefficient only by small numerical errors and cannot be distinguished in this plot. For the studies of the off-set of collisional bootstrap (Ware-pinch) coefficient from the asymptotic value seen at low but finite collisionality, we examine the distribution function computed by NEO-2 in the direct and adjoint problems separately.

2.3.1. Direct problem

An odd part of the distribution function perturbation g^{odd} responsible for the bootstrap current in the direct problem is shown in figure 3. One can observe the appearance of boundary layers around class-transition boundaries (but not at the trapped–passing boundary) with decreasing collisionality. It can be seen that, at lowest collisionality, $\nu_* = 10^{-6}$, where the asymptotic limit is reached in figure 2, the highest class-transition boundary layer corresponding to two highest local maxima becomes clearly separated from the trapped–passing boundary.

The distribution of the parallel equilibrium current in velocity space is better seen from figure 4, where an integral $\int_{\eta}^{1/B} \mathrm{d}\eta'\, g^{\mathrm{odd}}$ is shown at the middle of the field line ($\varphi = \varphi_b = 5\pi$). According to (2.38), the value of this integral at $\eta = 0$ up to a factor equals the parallel equilibrium current density. It can be seen that the contribution of the trapped particle region to the parallel current is independent of collisionality despite the varying width of the class-transition boundary layers which carry a significant amount of this current. Off-set of the current which depends on collisionality is produced in the passing particle region. Solution g^{odd} in this region is determined up to arbitrary constant, which should match then the solution in the trapped–passing

https://doi.org/10.1017/S0022377825000200 Published online by Cambridge University Press

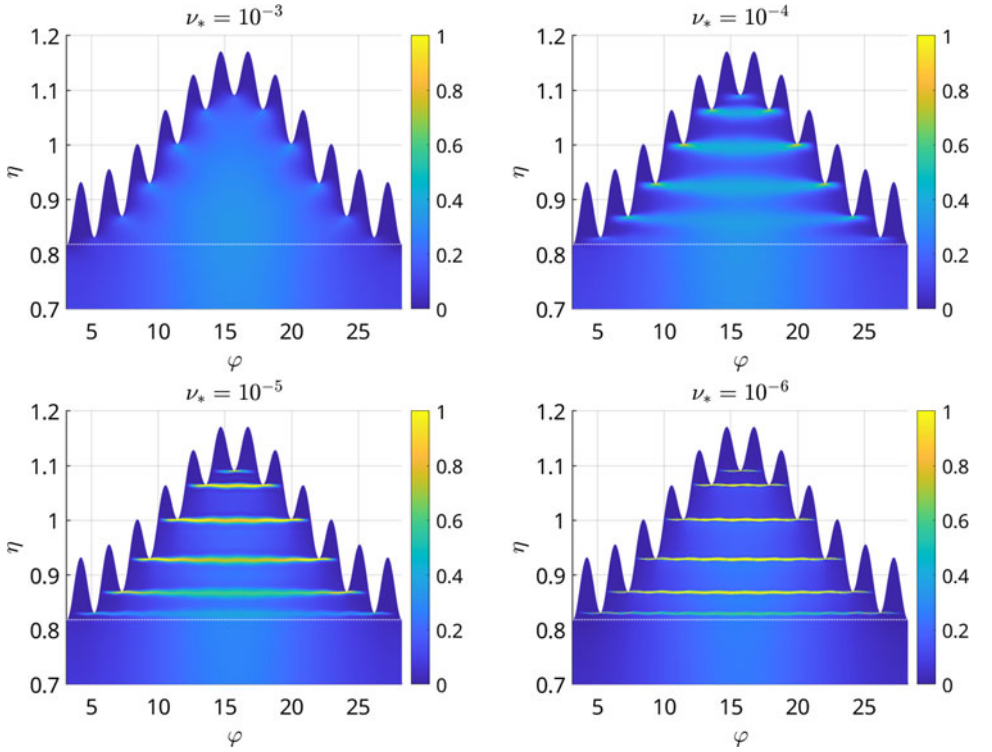

FIGURE 3. Odd part of the distribution function, $g^{\mathrm{odd}}(\varphi, \eta) = (g(\varphi, \eta, 1) - g(\varphi, \eta, -1))/2$, driven by $s_{(1)}$ for different normalized collisionalities ν_* (see the legend) in case $\iota = 1/4$. The trapped–passing boundary is shown by a white dotted line.

boundary layer. At sufficiently low collisionalities ($\nu_* < 10^{-5}$), where the bootstrap current is independent of collisionality, the nearest class-transition boundary layer is well separated from the trapped–passing boundary (see figure 5), and the boundary condition for passing particles is fully determined by the last trapped orbit nearest to the boundary between the trapped and passing particle domains (Boozer & Gardner 1990). The rest of trapped particle domain has no effect on the passing distribution, because 'particles' generated by bounce-averaged drift in the first local ripple fully annihilate in class-transition boundary layer with 'anti-particles' generated in the last local ripple where the sign of geodesic curvature is opposite to the sign in the first ripple. At higher collisionalities ($\nu_* \geqslant 10^{-5}$), where the trapped–passing boundary layer crosses the class-transition boundary, some part of the 'particles' generated in the first ripple (where source $s_{(1)} > 0$) and leaving this ripple with positive velocity (in the direction of a local maximum) when changing due to collisions their trapping class, can later cross the trapped–passing boundary without mirroring and enter a co-passing particle domain. Similarly, 'anti-particles' from the last ripple enter the counter-passing domain. Both create a current off-set of the same sign. Naturally, they cannot annihilate because they enter different domains.

Note that at some intermediate collisionality off-set changes sign (see figure 2). In this case, the class-transition layer is almost isolated from the trapped-passing boundary, so that the probability to enter the passing domain after a single pass along

https://doi.org/10.1017/S0022377825000200 Published online by Cambridge University Press

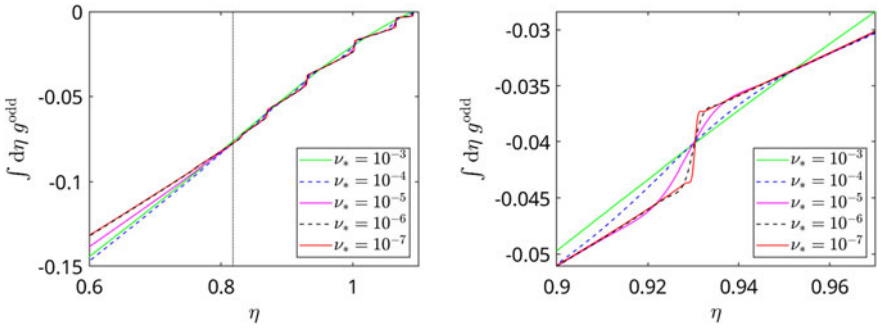

FIGURE 4. Integral $\int_{\eta}^{1/B} \mathrm{d}\eta'\, g^{\mathrm{odd}}$ as a function of the lower limit (left), and its zoom near one of the class-transition boundaries (right) for various plasma collisionalities (see the legend) at $\varphi = 5\pi$. The trapped–passing boundary is shown by a vertical dotted line.

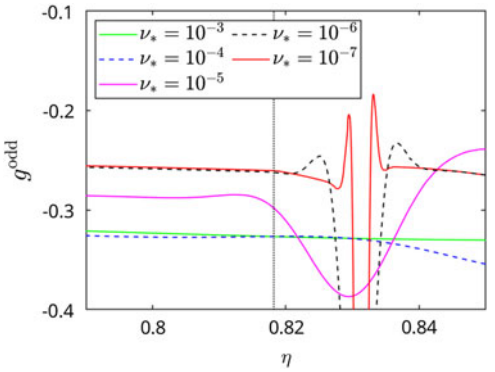

FIGURE 5. Odd part of the distribution function g^{odd} near the trapped–passing boundary (vertical dotted line) at $\varphi = 5\pi$ for various collisionalities (see the legend).

the boundary layer is lower than the probability to do that after the first reflection near the global maximum. In such a case, most 'particles' enter counter-passing domain ('anti-particles' – co-passing) which results in negative current off-set.

2.3.2. Adjoint problem

An even part of the distribution function perturbation g^{even} responsible for particle flux (Ware pinch) in the adjoint problem is shown in figure 6 for the same cases as in figure 3. As expected, the boundary layer appears at low collisionality only at the trapped–passing boundary. The structure of this layer well agrees with the complete analytical solution (2.53), i.e. g^{even} is an anti-symmetric function of φ with respect to the middle stellarator symmetry point φ_s.

Similar to the direct problem, if the trapped–passing boundary layer is well separated from the nearest class-transition boundary (lowest collisionality case, $\nu_* = 10^{-6}$) the Ware-pinch coefficient agrees with the asymptotic limit. At higher collisionalities where this boundary layer enters a class-transition boundary, one can observe

https://doi.org/10.1017/S0022377825000200 Published online by Cambridge University Press

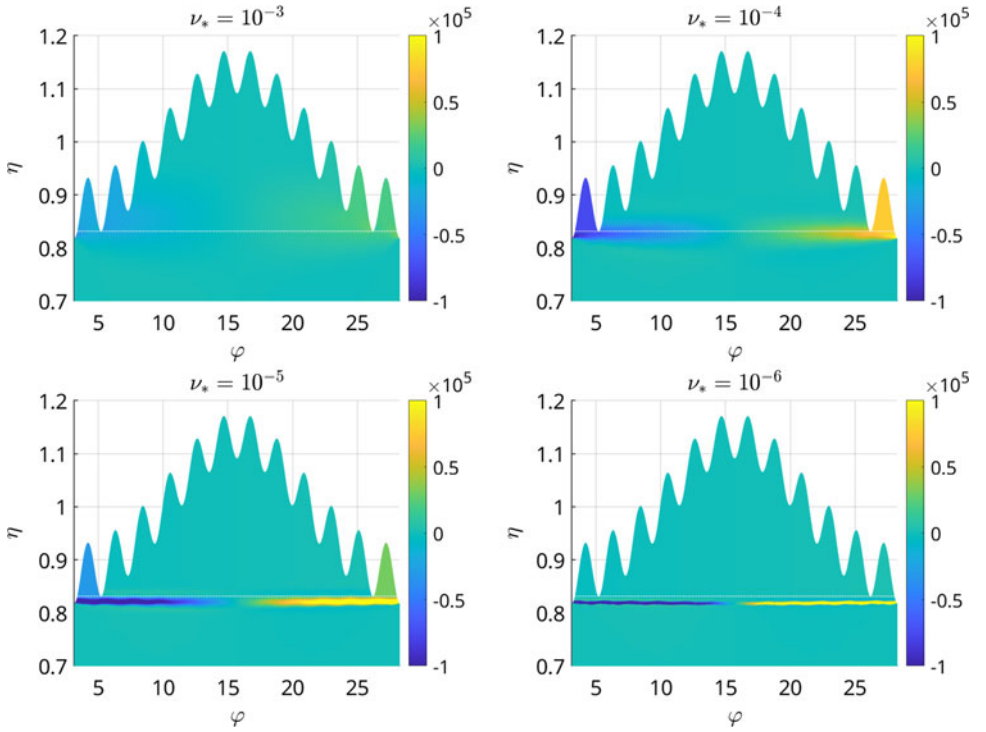

FIGURE 6. Even part of the distribution function, $g^{\text{even}}(\varphi, \eta) = (g(\varphi, \eta, 1) + g(\varphi, \eta, -1))/2$, driven by $s_{(3)}$ for the same cases as in figure 3. The transition boundary between the two highest trapping classes is shown by a white dotted line.

increased g^{even} in the local ripple wells whose lowest maximum determines this transition boundary. This accumulation of the particles in local ripples drives the off-set of Ware pinch since g^{even} there is anti-symmetric with respect to the mid-point $\varphi_b = 5\pi$, which is true also for geodesic curvature and, respectively, for the bounce-averaged radial drift velocity in these local ripples. Therefore, particles in both ripples drive the flux of the same sign. In the following, we will call such ripples 'off-set wells'. As one can see from figure 7, g^{even} is constant in most of the off-set well, and changes only in the vicinity of class-transition boundary. Therefore, we can characterize g^{even} in the whole off-set well by its value at the off-set well bottom, which will be denoted as g_{off}. It can be seen that g_{off} has similar feature to λ_{bB}, i.e. it changes sign with reducing collisionality before going to zero.

Properties of this distribution function off-set, which was also observed in GSRAKE modeling (Beidler 2020), will be studied in more detail in the next section. Here, we only show an extra example in figure 8 where more than one type of off-set wells is present simultaneously with different types of off-sets dominating at different collisionalities. In this example, both off-set wells containing only the lowest class of trapped particles who traverse a single minimum during their bounce period (as in figure 6) and an off-set wells containing many classes are shown. Note that trapped–passing boundary layer which has a standard (collisionless) form at lowest collisionality $\nu_* = 10^{-6}$ appears to be split into two independent layers at the intermediate collisionalities $\nu_* \leqslant 10^{-4}$ where mismatch of two local maxima located

https://doi.org/10.1017/S0022377825000200 Published online by Cambridge University Press

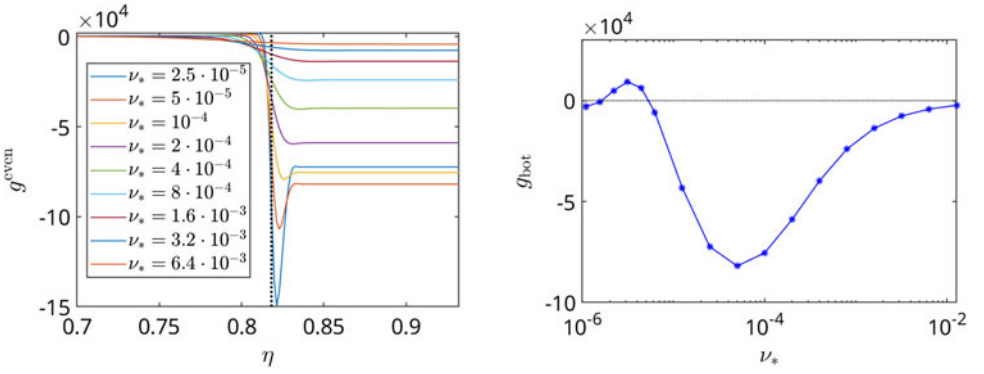

FIGURE 7. Even part of the distribution function g^{even} as a function of η in the middle of the left off-set well, $\varphi = 4\pi/3$ for various collisionalities (left) and $\iota = 1/4$. The trapped–passing boundary is shown by a vertical dotted line. The value of g^{even} at the off-set well bottom, g_{bot}, is shown as a function of ν_* in the right plot.

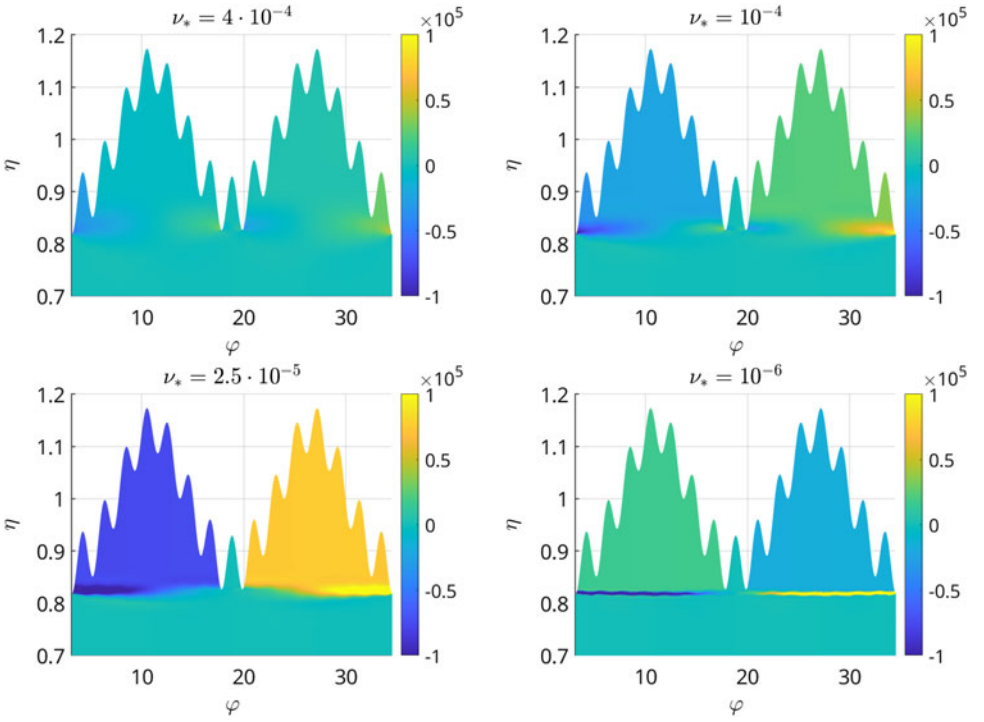

FIGURE 8. The same as in figure 6 for $\iota = 2/5$ and different collisionalities (see the legend).

near the middle of the field line with the global maximum becomes small compared with the typical boundary layer width (see the discussion of a few global maxima case after (2.53)). Thus, the off-set phenomenon has a rather high complexity even

https://doi.org/10.1017/S0022377825000200 Published online by Cambridge University Press

in the simple case of a closed field line which is, nevertheless, illustrative for realistic configurations. In particular, switching off-sets can be observed in figure 3 of Kernbichler *et al.* (2016) where bootstrap coefficient has been computed for W-7X down to collisionalities $\nu_* = 10^{-9}$.

3. Bootstrap/Ware-pinch off-set for a closed field line

Let us study the bootstrap/Ware-pinch off-set phenomenon in more detail. Since both effects are quantitatively the same due to the Onsager symmetry of the transport coefficients, we focus now on the Ware-pinch effect only.

3.1. *Boundary layer e-folding*

As we have seen from asymptotic solutions and numerical examples in both direct and adjoint problems, the distribution function g_0, which is independent of collisionality in most of the phase space, includes huge contributions localized in the boundary layers where they scale as $l_c^{1/2} \sim \nu^{-1/2}$ and formally become infinite in the collisionless limit manifested by δ-functions in the asymptotic solutions. To estimate the decay of these localized contributions outside the boundary layer, we consider the homogeneous kinetic equation (2.3) and use the ansatz which is only slightly different from the ansatz of Helander *et al.* (2011) and leads to the same approximation at the end. Namely, we replace in the trapped particle domain the independent variable φ with

$$\theta_H = \theta_H(\varphi, \eta, \sigma) = \frac{\pi\sigma}{I_j} \int_{\varphi_j^-}^{\varphi} \frac{\mathrm{d}\varphi' |\lambda|}{B^{\varphi}}, \tag{3.1}$$

where the integral $I_j = I_j(\eta)$ is defined in (2.26). Thus, particles with $\lambda > 0$ are described by $0 < \theta_H < \pi$, particles with $\lambda < 0$ are described by $-\pi < \theta_H < 0$ and continuity of the distribution function at both turning points is enabled by periodicity of g with θ_H. Formally presenting the homogeneous equation (2.3) in tensor form

$$\frac{\partial}{\partial z^i} \mathcal{J} \left(\mathcal{V}^i g - \mathcal{D}^{ij} \frac{\partial g}{\partial z^j} \right) = 0, \tag{3.2}$$

where $z^i = (\varphi, \eta)$, and transforming the contra-variant components of the phase space velocity $\mathcal{V}^i$ and diffusion tensor $\mathcal{D}^{ij}$ and the Jacobian $\mathcal{J}$ to the new phase space coordinates (θ_H, η) using tensor algebra rules, this equation takes the form

$$\frac{\partial g}{\partial \theta_H} = \left(\frac{\partial}{\partial \eta} + \frac{\partial}{\partial \theta_H} \frac{\partial \theta_H}{\partial \eta} \right) D_H \left(\frac{\partial g}{\partial \eta} + \frac{\partial \theta_H}{\partial \eta} \frac{\partial g}{\partial \theta_H} \right), \tag{3.3}$$

where differential operators $\partial/\partial\eta$ and $\partial/\partial\theta_H$ act on everything to the right, and

$$D_H = D_H(\eta) = \frac{\eta I_j}{\pi l_c}. \tag{3.4}$$

Expanding the distribution function in Fourier series over θ_H,

$$g(\theta_H, \eta) = \sum_{m=-\infty}^{\infty} g_{[m]}\, \mathrm{e}^{im\theta_H}, \tag{3.5}$$

https://doi.org/10.1017/S0022377825000200 Published online by Cambridge University Press

equation (3.3) turns into a coupled set of ordinary differential equations for Fourier amplitudes $g_{[m]}(\eta)$. It should be noted that terms with $\partial\theta_H/\partial\eta$ which lead to the coupling of Fourier modes are negligibly small in most of phase space except for the close vicinity of the boundary (sub-layer (Helander *et al.* 2011)) where due to the scaling $\partial^2\theta_H/\partial\eta^2 \sim \eta^{-1}(\eta-\eta_b)^{-1}$ their contribution is comparable to the left-hand side which means the sub-layer width $\eta-\eta_b \sim \nu_* \ll \sqrt{\nu_*}$. Thus, one can ignore the right-hand side terms with derivatives over θ_H outside the sub-layer, and the set decouples into

$$im g_{[m]} = \frac{\partial}{\partial\eta} D_H \frac{\partial g_{[m]}}{\partial\eta}. \tag{3.6}$$

Harmonic

$$g_{[0]} = \frac{1}{2I_j} \sum_{\sigma=\pm1} \int_{\varphi_j^-}^{\varphi_j^+} \mathrm{d}\varphi \frac{|\lambda| g}{B^\varphi}, \tag{3.7}$$

is actually zero in our case because δ-like terms in the direct problem are odd, and the solution of the adjoint problem is stellarator antisymmetric. Ignoring in (3.6), variation of D_H in the main boundary layer, $D_H(\eta) \approx D_H(\eta_b)$, which brings this equation in agreement with the result of the "rectangular well" ansatz of Helander *et al.* (2011), we look for solutions in the form $g_{[m]} \propto \exp(\kappa_m(\eta-\eta_b))$ with the $m=1$ harmonic being dominant with increasing $\eta-\eta_b$. Thus, boundary layer contribution decays outside the layer as

$$\Delta g_{\mathrm{fit}} \approx a \exp\left(\frac{\eta_b-\eta}{\delta\eta_e}\right)\left(\cos\left(\frac{\eta_b-\eta}{\delta\eta_e}+\phi\right)\cos\left(|\theta_H|\right) - \sigma\sin\left(\frac{\eta_b-\eta}{\delta\eta_e}+\phi\right)\sin\left(|\theta_H|\right)\right), \tag{3.8}$$

where $|\theta_H| = |\theta_H(\varphi,\eta)|$, and $\delta\eta_e$ is boundary layer e-folding length,

$$\delta\eta_e = \sqrt{2D_H(\eta_b)} = \sqrt{\frac{2\eta_b I_j(\eta_b)}{\pi l_c}} \sim \eta_b \left(\frac{\Delta B}{B}\right)^{1/4} \left(\frac{\nu_*\Delta\varphi}{2\pi}\right)^{1/2}, \tag{3.9}$$

estimated in the last expression via typical variation of B in the magnetic well ΔB and toroidal extent of the boundary layer $\Delta\varphi$.

In figures 9 and 10, the boundary layer contribution represented by the difference $\Delta g = g - g_0$ between the numerical (NEO-2) and analytical (2.47) solutions of the adjoint problem is compared with the asymptotic boundary layer solution Δg_{fit} given by (3.8) with amplitude a and phase ϕ fitted to match Δg in the upper left plot of figure 9. Oscillations of Δg with η in figure 9 result from interchanging dominance of "particles' and "anti-particles" which enter the trapping domain and become mirrored there once (twice, etc.). Since the observation point in the last three plots is in the region $\varphi_s < \varphi < \varphi_N$, "particles" dominate there over "anti-particles" in the first peak (see also figure 6) which they produce before the first reflection. The above mechanism results in helical structures in $g(\varphi,\lambda)$ distribution formed in the trapped particle domain (see figure 10). They are produced by the combination of the collisionless phase space flow (which is clockwise in this domain) and the flow

https://doi.org/10.1017/S0022377825000200 Published online by Cambridge University Press

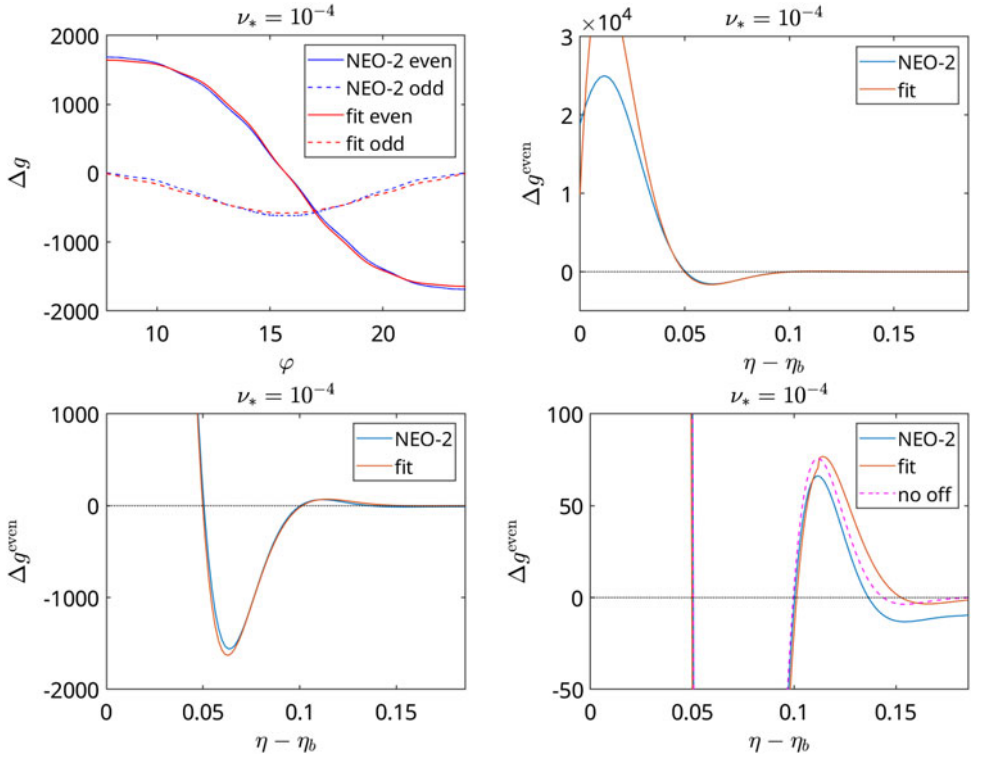

FIGURE 9. Difference Δg and the fit $\Delta g_{\rm fit}$, (3.8) for the case $\nu_* = 10^{-4}$ in figure 6. Upper left – even and odd parts as functions of φ for $\eta - \eta_b = 0.07$. Upper right – even parts as functions of η for $\varphi = 19\pi/3$ (7th local maximum). Lower panel – zooms of the upper right plot over the Y-axis. Dashed line in the last zoom corresponds to the NEO-2 result for $g^{\rm even} - g_{\lambda=0}$, where $g_{\lambda=0}$ is $g^{\rm even}$ for standing particles with $\eta = 1/B$. Function $g_{\lambda=0}$ differs here from $g_0 = g_0^t$ by an exponentially small off-set.

driven by the collisional diffusion (directed over λ to the trapped particle domain from the co- and counter-passing particle domains, where sources of "particles" and "anti-particles" are located, respectively).

Note that oscillatory behavior similar to that in figure 9 is seen also in the class-transition boundary layers in figure 5 and is reflected then in the small bootstrap off-set oscillation in figure 2 at low collisionality, where it decreases exponentially.

3.2. *Propagator method, leading-order solution*

For more detailed analysis of boundary layer effects on bootstrap/Ware-pinch off-set, we use propagator method. We look for the solution of the adjoint problem in the whole phase space in the form

$$g_{(3)}(\varphi, \eta, \sigma) = \Theta(\eta_b - \eta) g_{-1}(\eta) + g_0^t(\varphi) + g_{\rm bou}(\varphi, \eta, \sigma), \tag{3.10}$$

where g_{-1} and g_0^t are given by (2.46) and (2.47), respectively. The kinetic equation (2.3) corresponding to the source $s_{(3)}$ transforms to

$$\hat{L} g_{\rm bou} = s_{\rm bou} + \Delta s, \tag{3.11}$$

https://doi.org/10.1017/S0022377825000200 Published online by Cambridge University Press

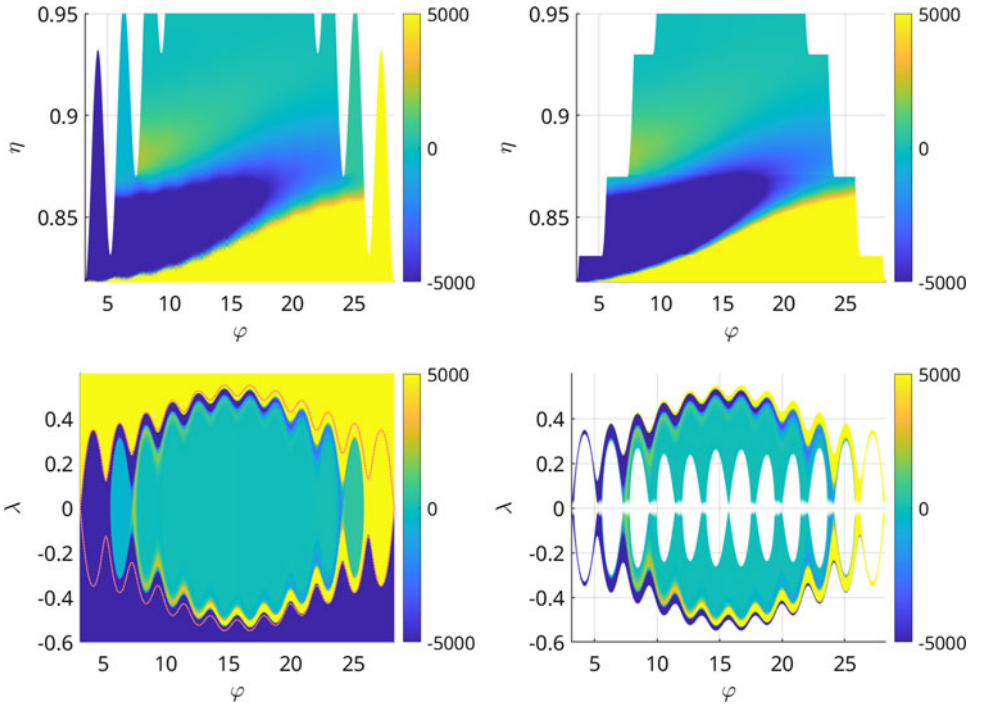

FIGURE 10. Difference Δg (left) and its fit $\Delta g_{\rm fit}$ (right) as functions of (φ, η) and $\sigma = 1$ (upper panel) and (φ, λ) (lower panel) for the same case as in figure 9. Saturation of color scale at $|\Delta g| \geqslant 5000$ occurs in the whole passing particle region. Fit $\Delta g_{\rm fit}$ is plotted excluding passing particle domains and local trapping domains where $\Delta g_{\rm fit}$ is not defined. Red dotted line in $\Delta g(\varphi, \lambda)$ plot shows the trapped–passing boundary where transient particles move clockwise.

where the source terms are

$$s_{\rm bou} = \sigma l_c \delta(\eta_b - \eta) \frac{D_\eta \langle B^2 \rangle}{\langle |\lambda| \rangle}, \tag{3.12}$$

$$\Delta s = -\sigma l_c \Theta(\eta_b - \eta) \frac{\partial}{\partial \eta} \frac{D_\eta \langle B^2 \rangle}{\langle |\lambda| \rangle} - \sigma l_c \frac{\partial}{\partial \eta} \left(\delta(\eta_b - \eta) D_\eta \int_\eta^{\eta_b} {\rm d}\eta' \frac{\langle B^2 \rangle}{\langle |\lambda| \rangle} \right). \tag{3.13}$$

In the following, we use a formal solution of (3.11) in terms of its Green's function, which makes it evident that the last term in (3.13) does not contribute to the solution since η-integral of this term weighted with any function with finite derivative over η is zero. The remaining term, as we check later, provides a correction of the order $\delta\eta_e$ to the solution driven by $s_{\rm bou}$, (3.12). Thus, we ignore Δs fully in the leading-order solution. Note that $g_{\rm bou}$ is an aperiodic function in the passing region due to aperiodicity of g_o^t in the definition (3.10). The leading-order solution is treated nevertheless as periodic, with the aperiodic term included in the ignored correction driven by Δs. It should be noted that correction terms ignored here may become important in a special case where the leading-order solution tends to vanish. These cases are discussed below in §§ 3.3 and 4.3.

https://doi.org/10.1017/S0022377825000200 Published online by Cambridge University Press

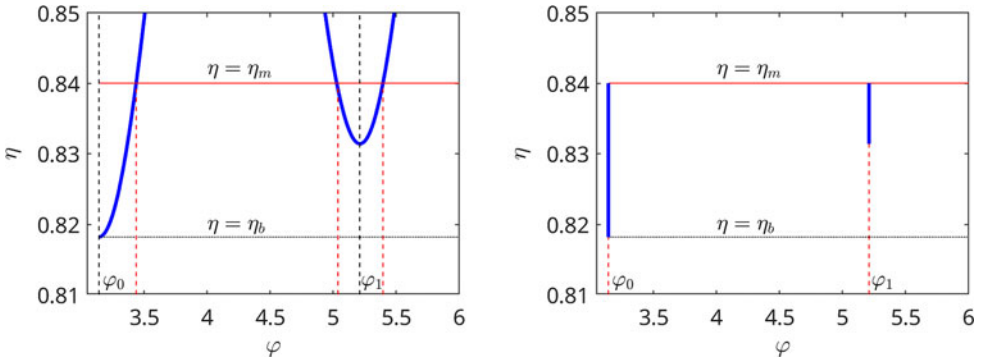

FIGURE 11. Computation domain before (left) and after (right) simplifying transformation. Trapped–passing boundary $\eta = \eta_b$ and matching boundary $\eta = \eta_m$ are shown by black dotted and red solid line, respectively. Original domain boundary $\eta = 1/B(\varphi)$ (solid blue), field maxima φ_j (dashed black) and boundaries of interface regions $\varphi_j \pm \delta\varphi$ (dashed red) are shown in the left plot. Reflecting (solid) and transparent (dashed) boundaries of the transformed domain are shown in the right plot.

We make the following simplifications. As follows from the analysis in § 3.1, solutions driven by sources located in the passing region or at the trapped–passing boundary tend exponentially to constants of η at some sufficiently large distance from the trapped–passing boundary, $\eta > \eta_m$, where matching boundary η_m satisfies $\delta\eta_e \ll \eta_m - \eta_b \ll \eta_b$. Generally, these constants can be different in different ripple wells in case they are bounded on both sides by the maxima fulfilling $\eta_m B(\varphi_j) > 1$, see figures 6 and 7. Thus, we solve (3.11) only in the domain $\eta < \eta_m$ imposing at the matching boundary zero flux condition, $\partial g_{\mathrm{bou}}(\varphi, \eta_m, \sigma)/\partial\eta_m = 0$. The boundary $\eta = \eta_m$ serves then as an upper boundary in most trapped particle domain, except the interface regions near the global maximum and local maxima fulfilling $\eta_m B(\varphi_j) > 1$, where $\eta_m B(\varphi) > 1$, see figure 11. Since the widths of these regions $\delta\varphi$ are small at low collisionalities, $\delta\varphi \sim B\delta\eta_e^{1/2}\left(\partial^2 B/\partial\varphi^2\right)^{-1/2} \propto l_c^{-1/4}$, we ignore the collision and source terms there, which leads in such a leading-order solution to an error of the order $|\lambda|\delta\varphi \sim (\delta\eta_e B)^{1/2}\delta\varphi \sim \delta\eta_e B^{3/2}\left(\partial^2 B/\partial\varphi^2\right)^{-1/2} \propto l_c^{-1/2}$, being of the same order as an error introduced by ignoring the sub-layer in § 3.1. (For this error estimate in the main boundary layer, $|\eta - \eta_b| \sim \delta\eta_e$, we compared the variance $2\int \mathrm{d}\varphi D_\eta$ in particle η introduced by the collisions when traversing the interface region with such variance for the whole trapping region assuming in the latter for simplicity that both, λ and the region extent in φ are of the order one. The error of the above model is of the order of one within the sub-layers, where effect of collisions on λ becomes comparable to the effect of mirroring force, but the overall contribution of these narrow sub-layers is similarly small.)

The solution is trivial in the interface regions, and we can express it via mapping between the boundaries $\varphi_j \pm \delta\varphi$ where φ_j is maximum point

$$g_{\mathrm{bou}}(\varphi_j \pm \delta\varphi, \eta, \pm 1) = g_{\mathrm{bou}}(\varphi_j \mp \delta\varphi, \eta, \pm 1), \qquad \eta B(\varphi_j) < 1,$$
$$g_{\mathrm{bou}}(\varphi_j \pm \delta\varphi, \eta, \pm 1) = g_{\mathrm{bou}}(\varphi_j \pm \delta\varphi, \eta, \mp 1), \qquad \eta B(\varphi_j) > 1. \tag{3.14}$$

https://doi.org/10.1017/S0022377825000200 Published online by Cambridge University Press

Similar to § 3.1, we ignore the dependence of the diffusion coefficient on η, setting $D_\eta(\varphi, \eta) \to D_\eta(\varphi, \eta_b)$ and, finally, ignore the extent of interface regions, $\delta\varphi \to 0$, with each of these steps introducing an error of the order $B\delta\eta_c \sim l_c^{-1/2}$, as before. Thus, we have transformed our computation domain to a set of rectangular domains $0 < \eta < \eta_m$, $\varphi_j < \varphi < \varphi_{j+1}$, limited by relevant field maxima, $\eta_m B(\varphi_j) > 1$ (see figure 11). This transformation leads to similar simplifications of the kinetic equation as the transformation used in § 3.1 for the main trapping region (or for the whole field line in case of vanishing boundary layer width) and is the same as the transformation of Helander *et al.* (2011) extended here to multiple local trapping regions.

Introducing Green's function $G_\sigma(\varphi, \eta, \varphi', \eta')$ which satisfies, with respect to (φ, η) variables, the homogeneous equation (3.11) with $D_\eta = D_\eta(\varphi, \eta_b)$, boundary conditions at the strongly passing and the matching boundary

$$\left(\frac{\partial}{\partial\eta} G_\sigma(\varphi, \eta, \varphi', \eta')\right)_{\eta=0} = \left(\frac{\partial}{\partial\eta} G_\sigma(\varphi, \eta, \varphi', \eta')\right)_{\eta=\eta_m} = 0, \tag{3.15}$$

and initial condition $G_\sigma(\varphi', \eta, \varphi', \eta') = \delta(\eta - \eta')$ at the starting point φ', we can formally express the leading-order solution to (3.11) within a single trapping domain, $\varphi_j < \varphi, \varphi' < \varphi_{j+1}$, as

$$g_{\mathrm{bou}}(\varphi, \eta, \sigma) = \int_0^{\eta_m} \mathrm{d}\eta' G_\sigma(\varphi, \eta, \varphi', \eta') g_{\mathrm{bou}}(\varphi', \eta', \sigma) + Q_\sigma(\varphi, \varphi', \eta), \tag{3.16}$$

where $\varphi > \varphi'$ for $\sigma = 1$ and $\varphi < \varphi'$ for $\sigma = -1$, and where

$$\begin{aligned} Q_\sigma(\varphi, \varphi', \eta) &= \sigma \int_{\varphi'}^{\varphi} \mathrm{d}\varphi'' \int_0^{\eta_m} \mathrm{d}\eta' G_\sigma(\varphi, \eta, \varphi'', \eta') s_{\mathrm{bou}}(\varphi'', \eta', \sigma) \\ &= C_0 \int_{\varphi'}^{\varphi} \mathrm{d}\varphi'' D_\eta(\varphi'', \eta_b) G_\sigma(\varphi, \eta, \varphi'', \eta_b), \end{aligned} \tag{3.17}$$

with a constant

$$C_0 = l_c \left(\frac{\langle B^2 \rangle}{\langle |\lambda| \rangle}\right)_{\eta=\eta_b}. \tag{3.18}$$

Introducing the fundamental solution in the unbounded η-region

$$G_\infty(\delta\eta, \eta - \eta') = \frac{1}{\sqrt{2\pi}\delta\eta} \exp\left(-\frac{(\eta - \eta')^2}{2\delta\eta^2}\right), \tag{3.19}$$

where

$$\delta\eta = \delta\eta(\varphi, \varphi') = \left| 2 \int_{\varphi'}^{\varphi} \mathrm{d}\varphi'' \, D_\eta(\varphi'', \eta_b) \right|^{1/2}, \tag{3.20}$$

https://doi.org/10.1017/S0022377825000200 Published online by Cambridge University Press

we can construct Green's function satisfying boundary conditions (3.15) as

$$G_\sigma(\varphi, \eta, \varphi', \eta') = G_\infty\left(\delta\eta, \eta - \eta'\right) + G_\infty\left(\delta\eta, \eta + \eta'\right) + G_\infty\left(\delta\eta, \eta + \eta' - 2\eta_m\right) + \mathcal{O}\left(\exp\left(-\frac{\eta_m^2}{2\delta\eta^2}\right)\right), \tag{3.21}$$

with the last term being negligibly small in the long mean free path regime where $\delta\eta \ll \eta_m$. By our assumption, $\delta\eta < \delta\eta_e \ll (\eta_m - \eta_b)$, and, of course, $\delta\eta \ll \eta_b$. Therefore, the second and third terms in (3.21) provide similarly exponentially small contributions to the source term (3.17) which can be expressed then as

$$Q_\sigma(\varphi, \varphi', \eta) = \frac{\sigma C_0 \delta\eta(\varphi, \varphi')}{\sqrt{8}} \Phi\left(\frac{\eta - \eta_b}{\sqrt{2}\delta\eta(\varphi, \varphi')}\right), \tag{3.22}$$

where

$$\Phi(x) = \frac{2}{\sqrt{\pi}} \int_0^1 \mathrm{d}t \, \exp\left(-\frac{x^2}{t^2}\right). \tag{3.23}$$

We can estimate now the next-order correction to the source term ΔQ driven by Δs, (3.13), in the trapped particle domain as $\Delta Q / Q_\sigma \sim B\delta\eta \log(B\delta\eta) \ll 1$, where the logarithm is due to the scaling of the bounce time with the distance to the trapped–passing boundary.

Since non-trivial behavior of the solution driven by s_{bou} is localized in the region $|\eta - \eta_b| \leqslant \delta\eta_e$ while g_{bou} tends to constant elsewhere, we can formally extend the domain $0 < \eta < \eta_m$ to an infinite domain $-\infty < \eta < \infty$ with boundary conditions $\lim_{\eta \to \pm\infty} \partial g_{\mathrm{bou}} / \partial\eta = 0$. Respectively, one should retain only the first term in Green's function (3.21) and use infinite limits of η' integration in (3.16). Thus, mapping between the distribution function $g^{\pm}_{j(\mathrm{in})}$ of particles which enter the trapping domain $\varphi_j < \varphi < \varphi_{j+1}$ and which leave this domain, $g^{\pm}_{j(\mathrm{out})}$,

$$\begin{aligned} g^{+}_{j(\mathrm{in})}(\eta) &= g_{\mathrm{bou}}(\varphi_j, \eta, 1), \qquad g^{+}_{j(\mathrm{out})}(\eta) = g_{\mathrm{bou}}(\varphi_{j+1}, \eta, 1), \\ g^{-}_{j(\mathrm{in})}(\eta) &= g_{\mathrm{bou}}(\varphi_{j+1}, \eta, -1), \qquad g^{-}_{j(\mathrm{out})}(\eta) = g_{\mathrm{bou}}(\varphi_j, \eta, -1), \end{aligned} \tag{3.24}$$

follows from (3.16) as

$$g^{\pm}_{j(\mathrm{out})}(\eta) = \int_{-\infty}^{\infty} \mathrm{d}\eta' G_\infty(\delta\eta_j, \eta - \eta') g^{\pm}_{j(\mathrm{in})}(\eta') + Q_{\mathrm{off}}(\delta\eta_j, \eta), \tag{3.25}$$

where

$$\delta\eta_j = \delta\eta(\varphi_j, \varphi_{j+1}) = \left(2\eta_b I_j(\eta_b)\right)^{1/2} I_c^{-1/2}, \qquad Q_{\mathrm{off}}(\delta\eta_j, \eta) = Q_\sigma(\varphi_j, \varphi_{j+1}, \eta), \tag{3.26}$$

and $I_j(\eta)$ is given by (2.26) so that $\delta\eta_j = \pi^{1/2}\delta\eta_e$, see (3.9). Conditions (3.14) with $\delta\varphi \to 0$ link the incoming distributions $g^{\pm}_{j(\mathrm{in})}$ to the outgoing $g^{\pm}_{j(\mathrm{out})}$ as follows:

$$\begin{aligned} g^{+}_{j(\mathrm{in})}(\eta < \eta_j) &= g^{+}_{j-1(\mathrm{out})}(\eta < \eta_j), \qquad g^{+}_{j(\mathrm{in})}(\eta > \eta_j) = g^{-}_{j(\mathrm{out})}(\eta > \eta_j), \\ g^{-}_{j(\mathrm{in})}(\eta < \eta_{j+1}) &= g^{+}_{j+1(\mathrm{out})}(\eta < \eta_{j+1}), \qquad g^{-}_{j(\mathrm{in})}(\eta > \eta_{j+1}) = g^{+}_{j(\mathrm{out})}(\eta > \eta_{j+1}), \end{aligned} \tag{3.27}$$

https://doi.org/10.1017/S0022377825000200 Published online by Cambridge University Press

where $\eta_j = 1/B(\varphi_j)$. Substitution of $g^{\pm}_{j(\mathrm{in})}$ into the mapping (3.25) via (3.27) leads to a coupled set of Wiener–Hopf-type integral equations for $g^{\pm}_{j(\mathrm{out})}$. Introducing a dimensionless variable x and dimensionless distribution function $\alpha^{\pm}_j$ as follows:

$$x = \frac{\eta_b - \eta}{\sqrt{2}\delta\eta_{\mathrm{ref}}}, \qquad g^{\pm}_{j(\mathrm{out})}(\eta) = \frac{C_0 \delta\eta_{\mathrm{ref}}}{\sqrt{8}} \alpha^{\pm}_j(x), \tag{3.28}$$

where $\delta\eta_{\mathrm{ref}}$ is some reference boundary layer width which is set in case of a closed field line to the largest $\delta\eta_j$, this set is of the form

$$\alpha^{\pm}_j(x) = \frac{A_j}{\sqrt{\pi}} \int_{-\infty}^{\infty} \mathrm{d}x' \, \mathrm{e}^{-A_j^2(x-x')^2} \left(\Theta\left(x^{\mp}_j - x'\right) \alpha^{\mp}_j\left(x'\right) + \Theta\left(x' - x^{\mp}_j\right) \alpha^{\pm}_{j\mp 1}\left(x'\right) \right)$$
$$\pm \frac{1}{A_j} \Phi(A_j x), \tag{3.29}$$

where mis-alignments of relevant maxima $x^{\pm}_j < 0$ and aspect ratios A_j are

$$x^{+}_j = \frac{\eta_b - \eta_{j+1}}{\sqrt{2}\delta\eta_{\mathrm{ref}}}, \qquad x^{-}_j = \frac{\eta_b - \eta_j}{\sqrt{2}\delta\eta_{\mathrm{ref}}}, \qquad A_j = \frac{\delta\eta_{\mathrm{ref}}}{\delta\eta_j}. \tag{3.30}$$

It should be noted that solution of set (3.29) is determined up to the null space of the original operator $\hat{L}$, (2.3), which is an arbitrary constant, i.e. $\alpha^{\pm}_j = \mathrm{const}$, and which produces no particle flux or parallel current but only re-defines the equilibrium Maxwellian.

3.3. *Alignment of maxima, equivalent ripples*

An obvious consequence of (3.29) is the configuration where the leading-order off-set is absent. Namely, coupled set (3.29) reduces to two coupled equations in the case that all trapping domains are equivalent, which means that all relevant maxima are aligned with a global maximum, $x^{\pm}_j = 0$, and all aspect ratios are the same (equal to one), $A_j = 1$. The first condition means that global maximum is reached on a line (lines) rather than at a point (points). The second condition means that all $\delta\eta_j$ are the same, i.e. the integral (3.20) between maximum points is the same for all trapping domains. In other words, this means that the value of the first integral (2.26) at the trapped–passing boundary $\eta = \eta_b$ does not depend on field line parameter ϑ_0,

$$\frac{\partial I_j(\vartheta_0, \eta_b)}{\partial \vartheta_0} = 0, \qquad I_j(\vartheta_0, \eta) = \frac{1}{2} \oint \frac{\mathrm{d}l}{B} \lambda = \frac{1}{2v} \oint \frac{\mathrm{d}l}{B} v_{\parallel}. \tag{3.31}$$

Thus, $\alpha^{\pm}_j(x) = \alpha^{\pm}$, and the set (3.29), respectively, closes to the form

$$\alpha^{\pm}(x) = \frac{1}{\sqrt{\pi}} \int_{-\infty}^{\infty} \mathrm{d}x' \, \mathrm{e}^{-(x-x')^2} \left(\Theta\left(x'\right) \alpha^{\pm}\left(x'\right) + \Theta\left(-x'\right) \alpha^{\mp}\left(x'\right) \right) \pm \Phi(x), \tag{3.32}$$

corresponding to quasi-symmetry (Nührenberg & Zille, 1988) (omnigeneity (Cary & Shasharina 1997; Helander & Nührenberg, 2009)). Obviously, the even part of the

https://doi.org/10.1017/S0022377825000200 Published online by Cambridge University Press

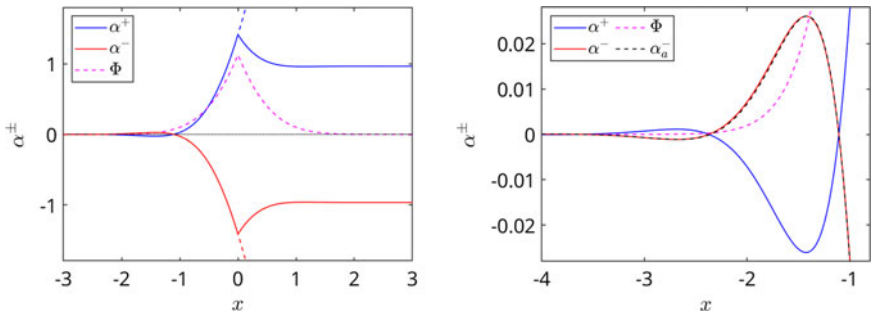

FIGURE 12. Normalized distribution functions α^+ (blue), α^- (red) and source function Φ (magenta). Full normalized distribution functions, $\alpha^\pm + \alpha^\pm_{1/\nu}$, are shown with dashed lines. The right picture is a zoom to the trapped region, where also the asymptotic solution (3.34) is shown (black dashed).

solution $\alpha^+ + \alpha^-$ satisfies a homogeneous equation and thus is constant, which we set to zero. Expressing $\alpha^- = -\alpha^+$, set (3.32) is reduced to a single Wiener–Hopf-type integral equation

$$\alpha^+(x) = \frac{1}{\sqrt{\pi}} \int_{-\infty}^{\infty} \mathrm{d}x' \, \mathrm{e}^{-(x-x')^2} \, \mathrm{sign}\left(x'\right) \alpha^+\left(x'\right) + \Phi(x). \tag{3.33}$$

Obviously, deep in the trapped region $x \to -\infty$ where $\Phi(x) \to 0$ and $\alpha^+ \to \mathrm{const}$, this equation reduces to $\alpha^+ = -\alpha^+$, i.e. it results in zero off-set $\alpha^\pm = 0$. Actually, as shown in (Helander *et al.* 2011), the ripple equivalence condition (3.31), which is fulfilled for a perfectly quasi-isodynamic stellarator where the magnetic field is omnigeneous, allows reduction of the boundary layer problem to a tokamak-like problem up to the same degree of accuracy as the analysis here (essentially, we use the integral representation of the same problem as in Helander *et al.* 2011).

Solutions to the equation set (3.32) are shown in figure 12 together with asymptotic solution (3.8) expressed in terms of normalized variables using $\delta\eta_j = \delta\eta_{\mathrm{ref}} = \sqrt{\pi}\delta\eta_e$ as

$$\alpha_a^\pm(x) = \pm\alpha_0 \exp\left(\sqrt{2\pi}\, x\right) \cos\left(\sqrt{2\pi}\, x + \phi\right), \tag{3.34}$$

where $\alpha_0 = \mathrm{const}$. They agree well because the latter solution must actually be the same as $\alpha^\pm$ in the region where the source term is negligible. We can recover the full solution if we add to $\alpha^\pm(x)$ the rescaled leading-order term (2.46) expanded to the linear order in $\eta - \eta_b$,

$$\alpha^\pm_{1/\nu}(x) = \frac{\sqrt{8}}{C_0 \delta\eta_{\mathrm{ref}}} \Theta(\eta_b - \eta) g_{-1}(\eta) \approx \pm 4x\Theta(x). \tag{3.35}$$

Naturally, full solution $\alpha^\pm(x) + \alpha^\pm_{1/\nu}(x)$ has a continuous derivative at the trapped–passing boundary.

Note that alignment of maxima, $x_j^\pm = 0$, is not sufficient on its own, without conditions of equal aspect ratios, $A_j = 1$, for avoiding the leading-order off-set. This

https://doi.org/10.1017/S0022377825000200 Published online by Cambridge University Press

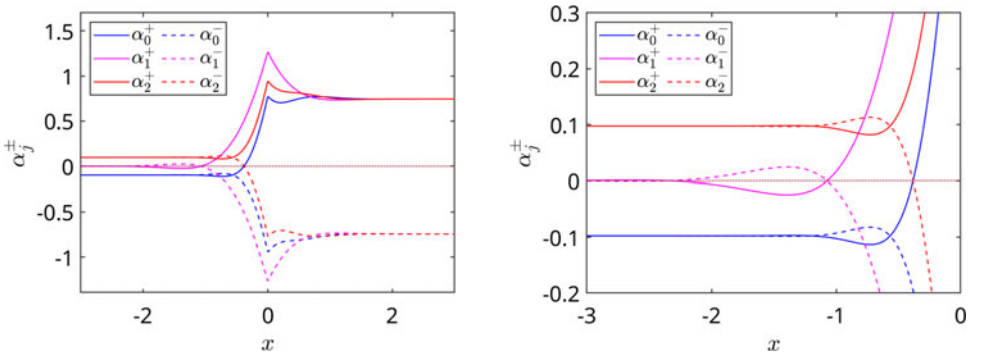

FIGURE 13. Normalized distribution functions α_j^+ (solid) and α_j^- (dashed) in the case of three relevant trapping domains per closed field line. The right picture is a zoom to the trapped particle domain.

can be seen from figure 13, where a solution to (3.29) is shown for the case of three relevant trapping domains and aligned maxima but different aspect ratios, $A_0 = A_2 = 2$ and $A_1 = 1$ (i.e. $2\delta\eta_0 = 2\delta\eta_2 = \delta\eta_1 \equiv \delta\eta_{\rm ref}$). A finite off-set in the first and last domains, $\alpha_2^{\pm}(-\infty) = -\alpha_0^{\pm}(-\infty)$, can be clearly seen. In such a case, the function $g_{\rm bou}$ in the trapped particle domain and, respectively, bootstrap coefficient, diverge at low collisionality as $\lambda_{bB} \sim \nu^{-1/2}$ (see the normalization (3.18) and (3.28)).

A particular example of configurations where the bootstrap coefficient diverges in the $1/\nu$ regime in this way is a family of 'anti-sigma optimized' configurations, i.e. configurations where sigma optimization (Mynick *et al.* 1982; Shaing & Hokin 1983) is applied to align maxima instead of minima. A magnetic field strength for a particular family of such configurations with dominant toroidal ripple is of the form

$$B(\vartheta, \varphi) = B_0 \left(1 + \varepsilon_0 \cos\left(N_{\rm tor}\varphi\right) + f(\vartheta)\left(1 - \cos\left(N_{\rm tor}\varphi\right)\right)\right), \tag{3.36}$$

where B_0 and ε_0 are constant parameters, $N_{\rm tor}$ is the number of field periods and $f(\vartheta) < \varepsilon_0$. For the computations with NEO-2, we use the following simple form of this function:

$$f(\vartheta) = \varepsilon_1 \cos\vartheta + \varepsilon_3 \cos(3\vartheta), \tag{3.37}$$

with $\varepsilon_0 = 0.125$, $\varepsilon_1 = 0.05$ and two values of ε_3. We set $N_{\rm tor} = 1$ and $\iota = 1/4$ to get 4 relevant domains (ripples) on a closed field line passing through the point $(\vartheta, \varphi) = (0, 0)$. In the case $\varepsilon_3 = 0$ (case 1), condition $A_j = 1$ does not hold, and a strong off-set of the bootstrap coefficient $\lambda_{bB} \propto \nu^{-1/2}$ is seen in figure 14. In the case $\varepsilon_3 = 0.06994425$ (case 2) all four ripples are equivalent, $A_j = 1$, and the leading-order off-set is absent. However, there still remains a residual off-set driven by source Δs, (3.13), which includes constant and logarithmic parts, $\delta\lambda_{bB} \to C_1 + C_2 \log(\nu_*)$, see the previous section. It should be noted that $\nu^{-1/2}$ divergence of λ_{bB} in the case of aligned maxima but non-equivalent ripples is not a property of a closed field line. A similar behavior is seen also for the case $\varepsilon_3 = 0$ at the irrational flux surface with $\iota = (1 + \sqrt{5})/20 \approx 0.1618$ labeled there as case 3.

https://doi.org/10.1017/S0022377825000200 Published online by Cambridge University Press

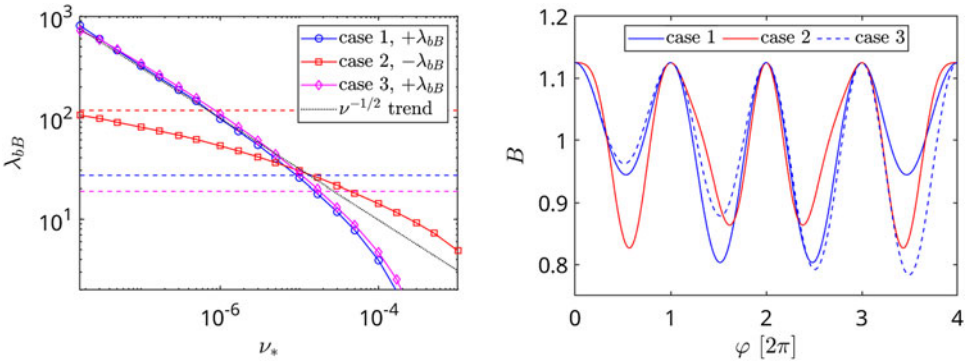

FIGURE 14. Left: normalized bootstrap coefficient λ_{bB}, (2.44), computed by NEO-2 for "anti-sigma optimized" configurations in cases 1, 2 and 3 (see the legend) as function of normalized collisionality ν_*. For each case, the Shaing–Callen limit (2.43) is shown with a dashed line of the respective color. Sign of λ_{bB} (but not of the respective asymptotic) is reversed in case 2. Right: magnetic field strength $B(\varphi)$, (3.36) for these cases plotted along the field line within the first four toroidal periods.

3.4. *Non-aligned maxima, large aspect ratio*

Let us consider now a more typical situation where local field maxima are not aligned. For simplicity, we consider a configuration with short ripples located near a global maximum adjacent to a long ripple, as in the case of the first rippled tokamak configuration (2.57) with $\iota = 1/4$ illustrated in figures 3 and 6. Besides the global maximum, there are only two relevant maxima at low collisionalities. They separate two short and shallow trapping domains, called below 'off-set domains', from a wide domain in between, called below the 'main region'. Setting $\delta\eta_{\rm ref} = \delta\eta_1$ so that $A_1 = 1$, aspect ratios for off-set domains are the same, $A_0 = A_2 \equiv A_o$. Respective value $A_o \approx 23.7 \gg 1$ will be called below the 'off-set aspect ratio', or simply 'aspect ratio'. To keep an example more general than the configuration with $\iota = 1/4$, we do not assume that the local maxima separating the main region from two off-set domains are the same (thus allowing broken stellarator symmetry). For the present example, it is convenient to change the general notation in (3.29) as follows, $\alpha_0^\pm \equiv \alpha_{-o}^\pm$, $\alpha_1^\pm \equiv \alpha_{mr}^\pm$ and $\alpha_2^\pm \equiv \alpha_{+o}^\pm$, so that subscripts '$+o$' and '$-o$' denote the left and right off-set domains, respectively, and subscript 'mr' stands for the main region. Respective normalized mis-alignments of local maxima we re-notate as follows, $x_1^+ = x_2^- \equiv x_{-o}$ and $x_3^- = x_2^+ \equiv x_{+o}$, see schematic figure 15. Thus, we cast the closed set of six equations (3.29) to

$$\alpha_{mr}^\pm(x) = \frac{1}{\sqrt{\pi}} \int_{-\infty}^{\infty} {\rm d}x'\ {\rm e}^{-(x-x')^2} \left(\Theta\left(x_{\mp o} - x'\right) \alpha_{mr}^\mp\left(x'\right) + \Theta\left(x' - x_{\mp o}\right) \alpha_{\mp o}^\pm\left(x'\right)\right) \pm \Phi(x),$$

$$\alpha_{\mp o}^\pm(x) = \frac{A_o}{\sqrt{\pi}} \int_{-\infty}^{\infty} {\rm d}x'\ {\rm e}^{-A_o^2(x-x')^2} \left(\Theta\left(-x'\right) \alpha_{\mp o}^\mp\left(x'\right) + \Theta\left(x'\right) \alpha_{\pm o}^\pm\left(x'\right)\right) \pm \frac{\Phi(A_o x)}{A_o},$$

https://doi.org/10.1017/S0022377825000200 Published online by Cambridge University Press

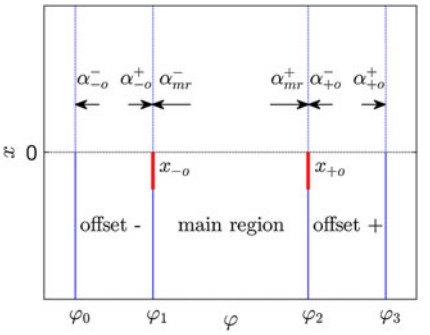

FIGURE 15. Locations of normalized outgoing particle distributions $\alpha^{\pm}_{\pm o}$ and $\alpha^{\pm}_{mr}$ in the respective off-set domains and the main region. Positions of relevant maxima φ_j are shown with blue lines. Normalized misalignments $x_{\pm o}$ are shown with red lines.

$$\alpha^{\pm}_{\pm o}(x) = \frac{A_o}{\sqrt{\pi}} \int_{-\infty}^{\infty} \mathrm{d}x' \, \mathrm{e}^{-A_o^2(x-x')^2} \left(\Theta\left(x_{\pm o} - x'\right) \alpha^{\mp}_{\pm o}\left(x'\right) + \Theta\left(x' - x_{\pm o}\right) \alpha^{\pm}_{mr}\left(x'\right) \right) \pm \frac{\Phi(A_o x)}{A_o}, \tag{3.38}$$

where notation $\alpha^{\pm}_{\mp o}$ means that either α^{+}_{-o} or α^{-}_{+o} should be taken, and $\alpha^{\pm}_{\pm o}$ means that either α^{+}_{+o} or α^{-}_{-o} should be taken.

Due to $A_o \gg 1$, source terms $\Phi(A_o x)/A_o$ can be ignored in the last two pairs of equations since $\alpha^{\pm}_{\mp o} \sim \alpha^{\pm}_{\pm o} \sim \alpha^{\pm}_{mr} \sim \Phi \gg \Phi/A_o$. Since $\alpha^{\pm}_{mr}(x)$, which varies on the scale $x \sim 1$, changes little compared with the exponent in the sub-integrand of the last pair of equations, we can set there $\alpha^{\pm}_{mr}(x') \approx \alpha^{\pm}_{mr}(x)$. Thus, the last pair of (3.38) takes the approximate form

$$\alpha^{\pm}_{\pm o}(x) \approx \frac{A_o}{\sqrt{\pi}} \int_{-\infty}^{x_{\pm o}} \mathrm{d}x' \, \mathrm{e}^{-A_o^2(x-x')^2} \alpha^{\mp}_{\pm o}\left(x'\right) + \tilde{\Theta}\left(A_o(x - x_{\pm o})\right) \alpha^{\pm}_{mr}(x), \tag{3.39}$$

where we introduced a "smooth step" function as

$$\tilde{\Theta}(x) \equiv \frac{1}{2}\left(1 + \mathrm{erf}(x)\right), \qquad \lim_{A_o \to \infty} \tilde{\Theta}(A_o x) = \Theta(x). \tag{3.40}$$

Further analysis is strongly simplified if we restrict ourselves to the most probable case of strong mis-alignment of local maxima where boundary layers in both off-set domains associated with these maxima are well separated from the trapped–passing boundary, $\delta\eta_0 \ll |\eta_b - \eta_1|$ and $\delta\eta_2 \ll |\eta_b - \eta_2|$. In normalized variables, these conditions mean $A_o|x_{\pm o}| \gg 1$. Since the first term in (3.39) is exponentially small in the region $A_o(x - x_{\pm o}) \gg 1$ where also $\Theta\left(A_o(x - x_{\pm o})\right) \approx 1$, (3.39) results there in $\alpha^{\pm}_{\pm o}(x) \approx \alpha^{\pm}_{mr}(x)$. Thus, the second pair of (3.38) with the source term ignored approximately is

https://doi.org/10.1017/S0022377825000200 Published online by Cambridge University Press

$$\alpha^{\pm}_{\mp o}(x) \approx \frac{A_o}{\sqrt{\pi}} \int_{-\infty}^{\infty} \mathrm{d}x'\ \mathrm{e}^{-A_o^2(x-x')^2} \left(\Theta\left(-x'\right) \alpha^{\mp}_{mr}\left(x'\right) + \Theta\left(x'\right) \alpha^{\pm}_{mr}\left(x'\right)\right), \quad A_o(x - x_{\mp o}) \gg 1. \tag{3.41}$$

Moreover, due to slow variation of $\alpha^{\pm}_{mr}(x')$ compared with the exponent, one can further simplify this expression to

$$\alpha^{\pm}_{\mp o}(x) \approx \Theta\left(-x\right) \alpha^{\mp}_{mr}\left(x\right) + \Theta\left(x\right) \alpha^{\pm}_{mr}\left(x\right), \tag{3.42}$$

which is valid in the region $x > x_{\mp o}$ except for small vicinities of class boundary, $|x - x_{\mp o}| \leqslant 1/A_o$, and trapped–passing boundary $|x| \leqslant 1/A_o$, which contain local boundary layers of the off-set domains (layers of the width $\delta\eta_0 \sim \delta\eta_2 \ll \delta\eta_1$). Contribution of these vicinities to the integral in the first pair of (3.38) is of the order of $1/A_o$, and, therefore, this pair can be closed as follows:

$$\alpha^{\pm}_{mr}(x) = \frac{1}{\sqrt{\pi}} \int_{-\infty}^{\infty} \mathrm{d}x'\ \mathrm{e}^{-(x-x')^2} \left(\Theta(x')\alpha^{\pm}_{mr}\left(x'\right) + \Theta\left(-x'\right) \alpha^{\mp}_{mr}\left(x'\right)\right) \pm \Phi(x) + O(A_o^{-1}). \tag{3.43}$$

Obviously, in the leading order over A_o^{-1}, these equations are the same as (3.32) for equivalent ripples.

For the solution in local trapping regions of the off-set domains, $x \leqslant x_{\pm o}$, Heaviside functions in the sub-integrands of the second pair of (3.38) can be replaced by their values at $x' < 0$ which turns this pair (with the source term ignored) into

$$\alpha^{\pm}_{\mp o}(x) = \frac{A_o}{\sqrt{\pi}} \int_{-\infty}^{\infty} \mathrm{d}x'\ \mathrm{e}^{-A_o^2(x-x')^2} \alpha^{\mp}_{\mp o}\left(x'\right). \tag{3.44}$$

Substituting this result in (3.39), we note also that variation of the last term in (3.39) is determined in the region of interest by $\tilde{\Theta}$ while the factor $\alpha^{\pm}_{mr}$ varies slowly and can be replaced by its value at $x = x_{\pm o}$. Introducing the new independent variable $y = A_o(x - x_{\pm o})$, equation set for $\alpha^{\pm}_{\pm o}$ reduces to two independent equations

$$\alpha^{\pm}_{\pm o}\left(x(y)\right) \approx \frac{1}{\pi} \int_{-\infty}^{0} \mathrm{d}y' \int_{-\infty}^{\infty} \mathrm{d}y''\ \mathrm{e}^{-(y-y')^2-(y'-y'')^2} \alpha^{\pm}_{\pm o}\left(x(y'')\right) + \tilde{\Theta}\left(y\right) \alpha^{\pm}_{mr}\left(x_{\pm o}\right), \tag{3.45}$$

which have constant solutions

$$\alpha^{\pm}_{\pm o}\left(x(y)\right) = \alpha^{\pm}_{mr}\left(x_{\pm o}\right), \qquad \alpha^{\mp}_{\pm o} = \alpha^{\pm}_{\pm o}. \tag{3.46}$$

Thus, we obtained an intuitively clear result that

- The distribution function in the main region (long ripple) is weakly affected by off-set domains (short ripples) which provide only a correction of the order of A_o^{-1}.

https://doi.org/10.1017/S0022377825000200 Published online by Cambridge University Press

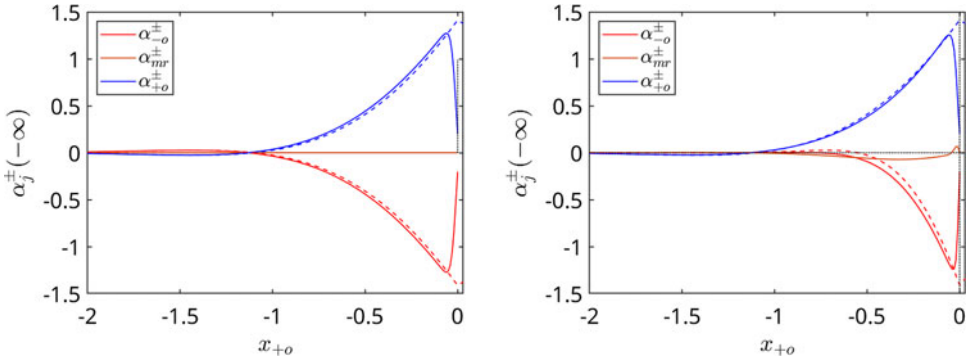

FIGURE 16. Off-sets in three local wells as functions of the normalized mis-match parameter x_{+o} for the symmetric case, $x_{-o} = x_{+o}$, (left) and for the destroyed stellarator symmetry, $x_{-o} = 2x_{+o}$, (right). Solid – results of direct solution of (3.29), dashed – approximation (3.46).

- The distribution function in the off-set well takes the value of the distribution function in the main region at the local minimum point (φ_j, η_j) separating the main region and the off-set domain (see also figure 6).

The last conclusion can be easily generalized to the case where a short off-set domain is separated from two long main regions by local maxima on both sides. Assuming that solutions in both main regions are known, the off-set is determined by the solution in the main region separated from the off-set domain by the lower local maximum (this local maximum determines the class-transition boundary η_c limiting the region $\eta > \eta_c$ with particles trapped in the off-set domain).

The large aspect ratio approximation, $A_o = 23.7$, is checked in figure 16, where the left picture corresponds to the stellarator-symmetric case of figure 6 and in the right picture symmetry of local maxima is destroyed by setting $x_{-o} = 2x_{+o}$. It can be seen that approximation (3.46) is good in its validity domain and is violated for small mis-match parameter values $x_{\pm o} \leqslant A_o^{-1}$. The finite off-set value for aligned maxima, $x_{\pm o} = 0$, is the result of $A_o \neq 1$. Note that left figure 16 corresponds to collisionality dependence of the off-sets in case of fixed magnetic field geometry. This dependence for the first local ripple is shown for the dimensional distribution function (3.28) in figure 17 where it is compared with the NEO-2 result. Since g_{bou} is given there by propagator method in the leading order only, we added error bars to the result of (3.29) showing the order of magnitude estimate of the omitted correction term Δg_{bou} driven by the source Δs in (3.11). According to (3.12), this correction term is driven by the sources in the passing particle region and is of the order of g_0^t at the trapped–passing boundary (and in the whole boundary layer) because Δg_{bou} must restore periodicity in the passing region. Since there are no sources in the trapped particle region, Δg_{bou} decays exponentially outside the boundary layer, as follows from (3.8) and from the solution $\alpha^+(x)$ for equivalent ripples, (3.33), where x is defined in (3.28). Therefore, we extend the estimate of the correction term to the whole trapped particle region by using $\Delta g_{\mathrm{bou}} \sim g_0^t \alpha^+(x)$. This simple estimation gives an error bar $g_0^t \alpha^+(x_{\pm o})$ that decreases when $x_{\pm o} \propto \nu_*^{-1/2}$ increases.

https://doi.org/10.1017/S0022377825000200 Published online by Cambridge University Press

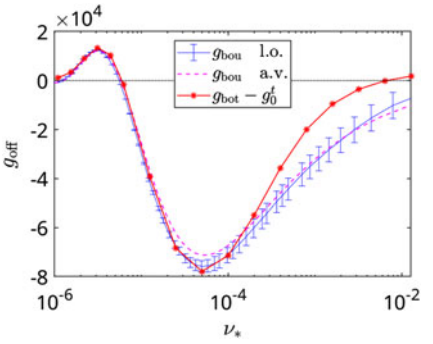

FIGURE 17. Distribution function off-set $g_{\rm off} = g_{(3)} - g_0^t$ at the bottom of the first local well, $j = 0$, as a function of collisionality parameter ν_* for configuration in figure 7. Blue – leading-order solution for $g_{\rm bou}$ via (3.29), magenta – its large aspect ratio approximation (3.46), red – off-set $g_{\rm off} = g_{\rm bot} - g_0^t$ via the result of NEO-2 shown in figure 7.

3.5. *Weakly non-equivalent ripples*

An important case is that of weakly non-equivalent ripples where the conditions of alignment of local maxima, $\eta_j = \eta_b$, and of equal aspect ratios, $A_j = 1$, are only slightly violated. Assuming infinitesimal mis-alignments $\eta_j - \eta_b$ and aspect ratio perturbations $\Delta A_j = A_j - 1$ and looking for the solution of (3.29) in the form $\alpha_j^\pm = \alpha^\pm + \Delta\alpha_j^\pm$, where $\alpha^+ = -\alpha^-$ are the solution to (quasi-symmetric) (3.32), the equation for the linear-order correction $\Delta\alpha_j^\pm$ is

$$\Delta\alpha_j^\pm(x) = \frac{1}{\sqrt{\pi}} \int_{-\infty}^{\infty} {\rm d}x' \, {\rm e}^{-(x-x')^2} \left(\Theta\left(-x'\right) \Delta\alpha_j^\mp\left(x'\right) + \Theta\left(x'\right) \Delta\alpha_{j\mp1}^\pm\left(x'\right)\right)$$
$$\mp x_j^\mp \, \Phi_B(x) \pm \Delta A_j \, \Phi_A(x). \tag{3.47}$$

Here, the first source term is due to small mis-alignment of maxima $|x_j^\mp| \ll 1$ with

$$\Phi_B(x) = \mp \lim_{|x_j^\mp|\to 0} \frac{2}{\sqrt{\pi} x_j^\mp} \int_{x_j^\mp}^{0} {\rm d}x' \, {\rm e}^{-(x-x')^2} \alpha^\pm\left(x'\right) = \frac{2\alpha^+(0)}{\sqrt{\pi}} \, {\rm e}^{-x^2}, \tag{3.48}$$

and the second source term is due to small differences in boundary layer widths $|\Delta A_j| \ll 1$ with

$$\Phi_A(x) = \frac{1}{\sqrt{\pi}} \int_{-\infty}^{\infty} {\rm d}x' \, {\rm e}^{-(x-x')^2} \left(1 - 2(x-x')^2\right) \, {\rm sign}\left(x'\right) \alpha^+\left(x'\right) - \frac{2}{\sqrt{\pi}} \, {\rm e}^{-x^2}. \tag{3.49}$$

Let us assume now an infinite number of ripples, $-\infty < j < \infty$, with only the first maximum mis-aligned, $\eta_1 - \eta_b = \Delta\eta \neq 0$, while the rest are aligned perfectly. Then

https://doi.org/10.1017/S0022377825000200 Published online by Cambridge University Press

the non-zero normalized mis-alignments are $x_0^+ = x_1^- = -\Delta x \equiv -\Delta\eta/(\sqrt{2}\delta\eta_{\mathrm{ref}})$ and the rest $x_j^\pm = 0$. In the absence of $\Delta A_j = 0$, solution to (3.47) is anti-symmetric with respect to the mis-aligned maximum, $\Delta\alpha_0^\pm = -\Delta\alpha_1^\mp$, $\Delta\alpha_{-1}^\pm = -\Delta\alpha_2^\mp$, etc. Thus, ripples $j \leqslant 0$ are eliminated from the set (3.47), where the only inhomogeneous equation is

$$\Delta\alpha_1^+(x) = \frac{1}{\sqrt{\pi}} \int_{-\infty}^{\infty} \mathrm{d}x'\ \mathrm{e}^{-(x-x')^2} \left(\Theta\left(-x'\right) \Delta\alpha_1^-\left(x'\right) - \Theta\left(x'\right) \Delta\alpha_1^+\left(x'\right)\right) + \Delta x\ \Phi_B(x), \tag{3.50}$$

while equations for $\Delta\alpha_1^-$ and $\Delta\alpha_j^\pm$ with $j > 1$ are given by the homogeneous set (3.47) with $x_j^\pm = \Delta A_j = 0$.

In the other case of perfectly aligned maxima, $x_j^\pm = 0$, and only one perturbed aspect ratio, $\Delta A_0 \neq 0$ and $\Delta A_j = 0$ for $j \neq 0$, solutions are anti-symmetric with respect to ripple $j = 0$, i.e. $\Delta\alpha_{-j}^\pm = -\Delta\alpha_j^\mp$. Thus, solutions with $j < 0$ are again eliminated from the set where the only inhomogeneous equation is

$$\Delta\alpha_0^+(x) = -\frac{1}{\sqrt{\pi}} \int_{-\infty}^{\infty} \mathrm{d}x'\ \mathrm{e}^{-(x-x')^2} \left(\Theta\left(-x'\right) \Delta\alpha_0^+\left(x'\right) + \Theta\left(x'\right) \Delta\alpha_1^-\left(x'\right)\right) + \Delta A_0\ \Phi_A(x), \tag{3.51}$$

while the rest $\Delta\alpha_j^\pm$ are given by the homogeneous set (3.47) for $j > 0$.

Off-set factors $\Delta_j^{A,B} = \Delta\alpha_j^+(-\infty) = \Delta\alpha_j^-(-\infty)$ as functions of ripple index j are shown in figure 18. Factors Δ_j^B are due to mis-alignment of a single local maximum between ripples 0 and 1 ($\Delta x = 1$ and $\Delta A_0 = 0$) and Δ_j^A are due to violation of the aspect ratio in ripple 0 ($\Delta x = 0$ and $\Delta A_0 = 1$). Off-set Δ_j^B is mainly produced in ripples 0 and 1 adjacent to the mis-aligned maximum, but it also propagates via the passing particle region to the distant maxima, decaying there as $\propto j^{-1}$. The effect on adjacent ripples can be understood in terms of 'particles' (produced by the inductive field in the passing region with positive velocities and having positive weight) and 'anti-particles' (negative velocities and weight). Some of the 'particles' entering the trapped region in ripple 0 from the passing region penetrate through the gap $\Delta\eta$ to the trapped region in ripple 1, thus producing a positive off-set there. Similarly, some of the 'anti-particles' entering ripple 1 produce a negative off-set in ripple 0. The effect on distant ripples is because some of the particles which penetrated the trapped region in ripple 1 return to the passing region and thus create the asymmetry of the boundary layer in those distant ripples. For the off-set Δ_j^A only the second mechanism is possible: if the boundary layer width in ripple 0 is larger than in other ripples (longer or deeper ripple), 'particles' which enter this ripple from the passing region have more chance to return, thus dominating the 'anti-particles' in the boundary layers of ripples with $j > 0$. Respectively, 'anti-particles' dominate in ripples with $j < 0$. Due to the symmetry, none are prevailing in ripple 0, where the off-set is absent in this case. Note that $\Delta A_0 > 0$ means a more narrow boundary layer, which is the reason for the negative Δ_j^A at $j > 0$ in figure 18.

https://doi.org/10.1017/S0022377825000200 Published online by Cambridge University Press

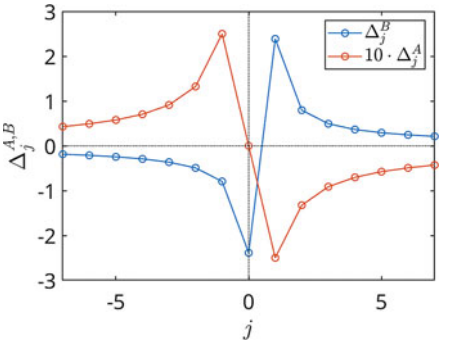

FIGURE 18. Factors Δ_j^B (blue) and Δ_j^A (red) as functions of the ripple index j.

The corresponding dimensional off-set for the ripple j related in the general case to the dimensionless off-set via (3.28) as follows:

$$g_{\rm off}^{(j)} \equiv g_{j({\rm out})}^{+}(\infty) = g_{j({\rm out})}^{-}(\infty) = \frac{C_0 \delta\eta_{\rm ref}}{\sqrt{8}} \alpha_j^{\pm}(-\infty), \tag{3.52}$$

is expressed in the present case via the off-set factors as

$$g_{\rm off}^{(j)} = \frac{l_c}{4} \left(\frac{\langle B^2 \rangle}{\langle |\lambda| \rangle} \right)_{\eta=\eta_b} \left(\Delta_j^B \Delta\eta + \sqrt{2} \Delta_j^A \Delta A_o \delta\eta_{\rm ref} \right). \tag{3.53}$$

One can see that an off-set due to maxima scales as $1/\nu$ and an off-set due to aspect ratios scales as $1/\sqrt{\nu}$, i.e. with reducing collisionality the role of the first one increases. Note that the linear approximation employed in this section requires $\Delta\eta \ll \delta\eta_{\rm ref}$. If the opposite limit is reached, ripples 0 and 1 combine into a ripple with $\Delta A_{0+1} \sim 1$, which strongly violates the alignment of aspect ratios, leading to much stronger off-set typical of the anti-sigma configurations discussed in § 3.3.

3.6. *Off-set of Ware-pinch coefficient*

We define the off-set in the normalized Ware-pinch (bootstrap) coefficient as follows, $\lambda_{\rm off} \equiv \lambda_{bB} - \lambda_{bB}^{\infty}$, where $\lambda_{bB} = \lambda_{bB}^{\dagger}$ is defined by (2.55) via mono-energetic $\bar{D}_{13}$ for finite collisionality and λ_{bB}^{∞} denotes its asymptotic ($l_c \to \infty$) value (2.43). Thus, $\lambda_{\rm off}$ is given by (2.55) with the replacement $g_{(3)} \to g_{\rm off} = g_{(3)} - g_{(3)}^{\infty}$ in the definition (2.11) of $\bar{D}_{13}$, where $g_{(3)}^{\infty}$ is the asymptotic solution g_0 derived in § 2.2.2. Splitting in (2.11) the integration interval $[\varphi_0, \varphi_N]$ into sub-intervals $[\varphi_j, \varphi_{j+1}]$ separated by relevant maxima φ_j (points of highest local maxima $\eta_j B(\varphi_j) = 1$ contained within the matching boundary η_m, $\eta_j < \eta_m$, see § 3.2), these intervals correspond to off-set domains or main regions where the even part of the distribution function $g_{\rm off}$ is essentially different from zero in the trapped particle domain and is close to a constant $g_{\rm off}^{(j)}$ approximated using propagator techniques by (3.52) in each interval $\varphi_j < \varphi < \varphi_{j+1}$ where we set $g_{\rm off}(\varphi, \eta) \approx \Theta(\eta - \eta_{\rm loc}^{(j)}) \Theta(\eta B(\varphi) - 1)\, g_{\rm off}^{(j)}$ with $\eta_{\rm loc}^{(j)} = \max(\eta_j, \eta_{j+1})$, we obtain the off-set coefficient as

$$\lambda_{\rm off} \approx \sum_j g_{\rm off}^{(j)} w_{\rm off}^{(j)}. \tag{3.54}$$

https://doi.org/10.1017/S0022377825000200 Published online by Cambridge University Press

Here, weighting factors are

$$w_{\rm off}^{(j)} = \frac{3}{2\rho_L B}\left(\int_{\varphi_0}^{\varphi_N}\frac{{\rm d}\varphi}{B^\varphi}\right)^{-1}\int_{\varphi_{(j)}^-}^{\varphi_{(j)}^+}{\rm d}\varphi\int_{\eta_{\rm loc}^{(j)}}^{1/B}{\rm d}\eta\, s_{(1)}^\dagger = -\frac{3}{2\rho_L B}\left(\int_{\varphi_0}^{\varphi_N}\frac{{\rm d}\varphi}{B^\varphi}\right)^{-1} H_j\left(\eta_{\rm loc}^{(j)}\right), \tag{3.55}$$

where $H_j(\eta)$ is given by (2.26), $\varphi_{(j)}^\pm = \varphi_j^\pm(\eta_{\rm loc}^{(j)})$ are coordinates of banana tips (turning points, see the definition of $\varphi_j^\pm(\eta)$ below (2.14)) of the transient orbit separating locally trapped orbits in the offset well from the rest of the phase space (one of the tips $\varphi_{(j)}^\pm$ is located at the point of lowest local maximum, φ_j or φ_{j+1}) and we assume here the closed field line (i.e. finite φ_N).

Using for $s_{(1)}$ the first definition (2.3) and exchanging the integration order, we can express weighting factors in terms of the bounce-averaged radial drift velocity and bounce time

$$\langle v_g^r\rangle_{bk} = \frac{2}{\tau_{bk}}\int_{\varphi_k^-(\eta)}^{\varphi_k^+(\eta)}\frac{{\rm d}\varphi B v_g^r}{|v_\parallel|B^\varphi}, \qquad \tau_{bk} = 2\int_{\varphi_k^-(\eta)}^{\varphi_k^+(\eta)}\frac{{\rm d}\varphi B}{|v_\parallel|B^\varphi}, \tag{3.56}$$

where $\varphi_k^\pm$ are the turning points defined below (2.14),

$$w_{\rm off}^{(j)} = -\frac{3}{2\rho_L B}\left(\int_{\varphi_0}^{\varphi_N}\frac{{\rm d}\varphi}{B^\varphi}\right)^{-1}\int_{\eta_{\rm loc}^{(j)}}^{1/B_{\rm min}^{(j)}}{\rm d}\eta\sum_{k\in{\rm off}(j)}\tau_{bk}\langle v_g^r\rangle_{bk}. \tag{3.57}$$

Here, $B_{\rm min}^{(j)}$ is the minimum value of B in the segment $[\varphi_j, \varphi_{j+1}]$, and the notation $k\in{\rm off}(j)$ means all segments satisfying $[\varphi_k^-(\eta), \varphi_k^+(\eta)]\in[\varphi_j, \varphi_{j+1}]$. As follows from (3.57), large off-set in the distribution function does not necessarily mean large off-set in the bootstrap/Ware-pinch coefficient. In the devices with minimized bounce-averaged radial drift such as, e.g. devices optimized for quasi-symmetry, the off-set of bootstrap current is also minimized.

Less demonstrative but more practical expressions are obtained by evaluating the integral over η in (3.55) with the help of the second definition (2.3) of $s_{(1)}$ and (2.5). Thus, weighting factors are expressed directly via the geodesic curvature

$$w_{\rm off}^{(j)} = -\frac{1}{2}\left(\int_{\varphi_0}^{\varphi_N}\frac{{\rm d}\varphi}{B^\varphi}\right)^{-1}\int_{\varphi_{(j)}^-}^{\varphi_{(j)}^+}{\rm d}\varphi\frac{|\nabla r|k_G}{BB^\varphi}\left(4-\eta_{\rm loc}^{(j)}B\right)(1-\eta_{\rm loc}^{(j)}B)^{1/2}. \tag{3.58}$$

In field aligned Boozer coordinates, we replace $B^\varphi = B^2(\iota B_\vartheta + B_\varphi)^{-1}$ with covariant field components being the flux functions, and use the last expression (2.6) for

https://doi.org/10.1017/S0022377825000200 Published online by Cambridge University Press

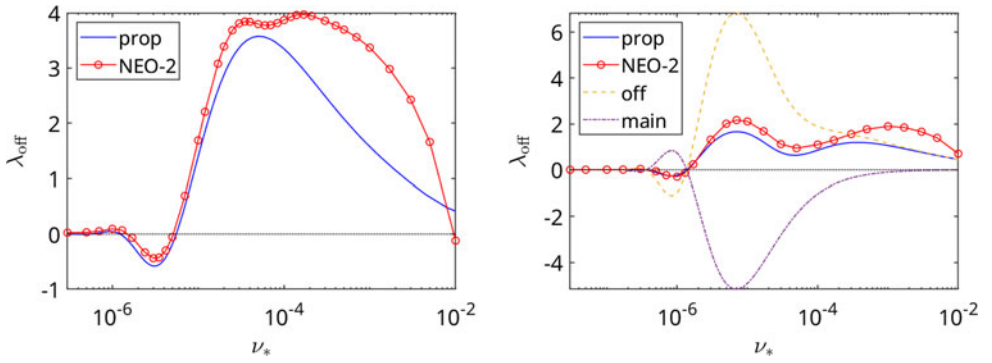

FIGURE 19. Off-set of the geometrical factor, λ_{off}, from the propagator method via (3.54) (blue) and from NEO-2 results shown in figure 2 (red) for $\iota = 1/4$ (left) and $\iota = 2/5$ (right). In the case of $\iota = 2/5$, also shown are summary contributions to (3.54) of the off-set domains (dashed) and of the main regions (dashed-dotted).

$|\nabla r| k_G$ to get

$$w^{(j)}_{\rm off} = \frac{{\rm d}r}{{\rm d}\psi}\left(\int_{\varphi_0}^{\varphi_N}\frac{{\rm d}\varphi}{B^2}\right)^{-1} I^{(j)}_{\mathcal{V}}, \qquad I^{(j)}_{\mathcal{V}} = \int_{\varphi^-_{(j)}}^{\varphi^+_{(j)}} {\rm d}\varphi \mathcal{V}, \tag{3.59}$$

where

$$\mathcal{V} = \frac{1}{2B^3}\frac{\partial B}{\partial \vartheta_0}\left(4 - \eta^{(j)}_{\rm loc} B\right)(1 - \eta^{(j)}_{\rm loc} B)^{1/2} = -\left[\frac{\partial}{\partial \vartheta_0}\frac{(1-\eta B)^{3/2}}{B^2}\right]_{\eta=\eta^{(j)}_{\rm loc}}. \tag{3.60}$$

It should be noted that the off-set (3.54) ignores the contribution of the trapped–passing boundary layer, where the distribution function is the largest and strongly depends on φ. This kind of off-set, which scales with the width of this layer, $\propto \nu^{1/2}$, is present also in axisymmetric devices and has been studied by Helander *et al.* (2011).

The result of (3.54) and (3.59) with $g^{(j)}_{\rm off}$ obtained by propagator method (figure 17) is compared with the NEO-2 result in figure 19. For the configuration with $\iota = 1/4$, the off-set is fully determined by the first (and last) off-set well, $g^{(0)}_{\rm off}$, since $g^{(1)}_{\rm off} = 0$ and $g^{(2)}_{\rm off} = -g^{(0)}_{\rm off}$ due to stellarator symmetry. For the configuration with $\iota = 2/5$, both the off-set well, $g^{(0)}_{\rm off}$, and the main region, $g^{(1)}_{\rm off}$, are contributing (with $g^{(3)}_{\rm off} = -g^{(1)}_{\rm off}$ and $g^{(4)}_{\rm off} = -g^{(0)}_{\rm off}$ just doubling the result due to stellarator symmetry). Off-set wells merge with the main regions (0 with 1 and 3 with 4) at $\nu_* < 10^{-4}$, therefore we used $\eta^{(j)}_{\rm loc}$ for such combined regions in individual $w^{(j)}_{\rm off}$. It can be seen that the contribution of the off-set wells is slightly larger than of the main regions, despite the much smaller toroidal extent, which is natural for bounce-averaged drift (the longer the orbit, the smaller is this drift). These two contributions tend to compensate for each other at lower collisionalities, which is a general trend due to the respective increase of the off-set domain length studied in more detail in § 4.2.

https://doi.org/10.1017/S0022377825000200 Published online by Cambridge University Press

As it could be expected, relatively good agreement between the propagator method and NEO-2 is obtained at very low collisionalities while at $\nu_* > 10^{-4}$ direct off-set due to boundary layer discussed by Helander *et al.* (2011) becomes also important.

4. Bootstrap/Ware-pinch off-set at irrational surfaces

As we have seen from the example of the 'anti-sigma' configuration in § 3.3, the Shaing–Callen limit cannot be reached in the case of perfectly aligned maxima where the bootstrap/Ware-pinch coefficient diverges as $1/\sqrt{\nu}$. This, however, is the ideal case, which cannot be realized exactly. As follows from (3.53), due to the strong $(1/\nu)$ scaling of maxima mis-alignment term with collisionality, sooner or later small mis-alignments of local maxima will prevail, and configuration will turn into a general one with a single global maximum. Therefore, we have to consider this general case now.

4.1. *Long field lines*

The field line integration technique employed in analytical asymptotic models and in NEO-2 assumes that the representative field line covers the flux surface densely enough so that the result does not depend on its length anymore. There are at least two ways to do so, in a way the ends of the field line are identical (and the solution is periodic) at the irrational surface. One way (standard in NEO-2) is to follow the line until there is a good match with the starting point, and then slightly modify $B(\varphi)$ in the last field period for a smooth field line closure. The result can be verified then by using another starting point at the same flux surface. Another way (employed here) is to replace ι with a rational number of a high-order well approximating the original irrational ι and start from the global maximum. Thus, within stellarator symmetry, one can always keep quasi-Liouville's theorem fulfilled exactly. Within this second approach, we consider now five different field lines for the magnetic field model used in § 2.3 with $\iota = 0.44 = 11/25$, $\iota = 0.43 = 43/100$, $\iota = 0.435 = 87/200$, $\iota = 0.438 = 219/500$ and $\iota = 0.442 = 221/500$ which cover the field period with 75, 300, 600 and 1500 passes, respectively.

The resulting normalized bootstrap coefficients (2.44) are shown in figure 20. They are weakly dependent on ι for collisionalities $\nu_* > 10^{-5}$ (in the first hill), and follow this trend down to $\nu_* = 10^{-6}$ in the second hill, with only the curve $\iota = 0.43$ departing from the other four. As one can see from the ι scan in this figure, this transition is smooth, in contrast to the Shaing–Callen limit which shows well-known 'bootstrap resonances' briefly discussed in § 4.4. To analyze this behavior, we plot the Ware-pinch distribution function $g_{(3)}(\vartheta, \varphi, \lambda)$ (mono-energetic generalized Spitzer function) for particles with zero parallel velocity ($\lambda = 0$) as function of angles for two cases of $\iota = 0.435$ and $\iota = 0.43$ and two different collisionalities, $\nu_* = 3 \cdot 10^{-4}$ (figure 21) and $\nu_* = 10^{-6}$ (figure 23). Since the distribution function in the trapped particle domain is almost independent of pitch parameter (equivalently of η), the plotted quantity characterizes well the radial particle flux. Obviously, this function is stellarator antisymmetric, $g_{(3)}(\vartheta, \varphi, 0) = -g_{(3)}(-\vartheta, -\varphi, 0)$, and retains all other relevant features seen for the short field line examples in § 2.3.2. Namely, 'hot spots' around the global maximum ($\vartheta = \pi$, $\varphi = \pi/3$), where $g_{(3)}$ is the largest, correspond to the contact region with the boundary layer (see the left figure 7). These spots are responsible for the tokamak-like off-set studied by Helander *et al.* (2011). One can

https://doi.org/10.1017/S0022377825000200 Published online by Cambridge University Press

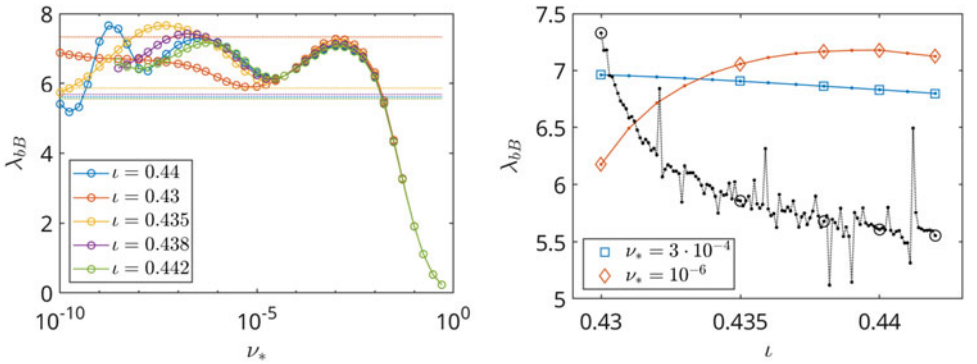

FIGURE 20. Normalized bootstrap coefficient (2.44) for five ι values vs. normalized collisionality ν_* (left) and its dependence on ι for two selected collisionalities shown in the legend (right). Shaing–Callen limit (2.43) is shown with dotted lines (data points – with dots). Abscissa values for markers in the right plot correspond to the legend in the left plot.

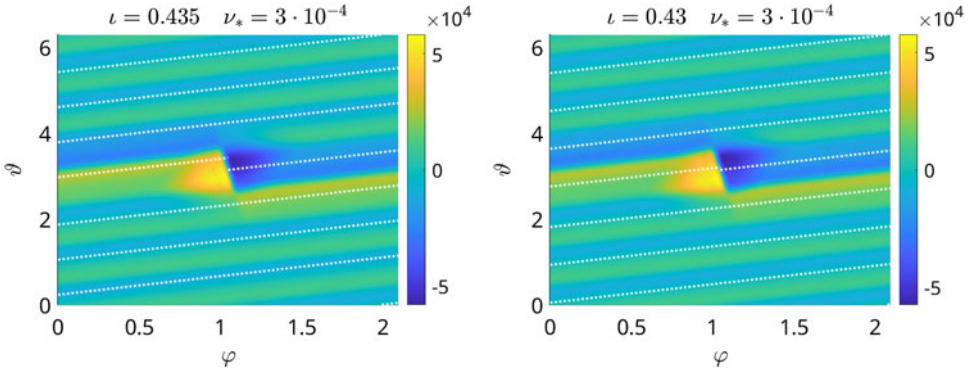

FIGURE 21. Generalized Spitzer function $g_{(3)}(\vartheta, \varphi, \lambda)$ for standing particles ($\lambda = 0$) at the flux surface with $\iota = 0.435$ (left) and $\iota = 0.43$ (right) for $\nu_* = 3 \cdot 10^{-4}$. White dotted lines show the field line starting from the global maximum and making 7 toroidal turns.

clearly see in figure 21 also the off-set domains (blue and yellow) in the ripples adjacent to the global maximum (mainly contributing to the off-set at this collisionality) as well as the widely extending 'main region' (green). Thus, this case is rather similar to figure 6 for $\nu_* = 10^{-4}$. Remarkably, results for two different ι are almost indistinguishable, which explains the close values of λ_{bB} in figure 20 at this collisionality. Since the radial guiding center velocity v_g^r is stellarator antisymmetric as well, the resulting normalized radial trapped particle flux distribution over the angles γ given with good accuracy by $\gamma(\vartheta, \varphi) = \mathcal{V}(\vartheta, \varphi) g_{(3)}(\vartheta, \varphi, 0)$, where $\mathcal{V}$ is the sub-integrand in (3.59), is stellarator symmetric. It is shown for $\nu_* = 3 \cdot 10^{-4}$ in figure 22, where the contribution of the off-set domain ($2 < \vartheta < 4$) is positive, which agrees with the first hill in figure 20. Note that the direct contribution of the boundary layer is already small at this collisionality, which is also seen from vanishing hot spots in figure 22.

Off-set in adjacent toroidal ripples vanishes completely for the lower collisionality case $\nu_* = 10^{-6}$ shown in figure 23. The visible difference between $\iota = 0.435$ and

https://doi.org/10.1017/S0022377825000200 Published online by Cambridge University Press

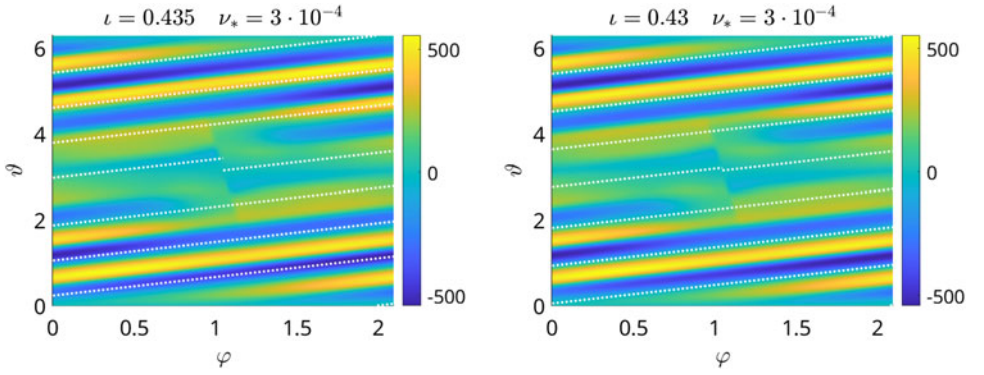

FIGURE 22. Normalized distribution over the angles of trapped particle radial flux $\gamma(\vartheta, \varphi)$ at the flux surface with $\iota = 0.435$ (left) and $\iota = 0.43$ (right) for $\nu_* = 3 \cdot 10^{-4}$. White dotted lines – the same as in figure 21.

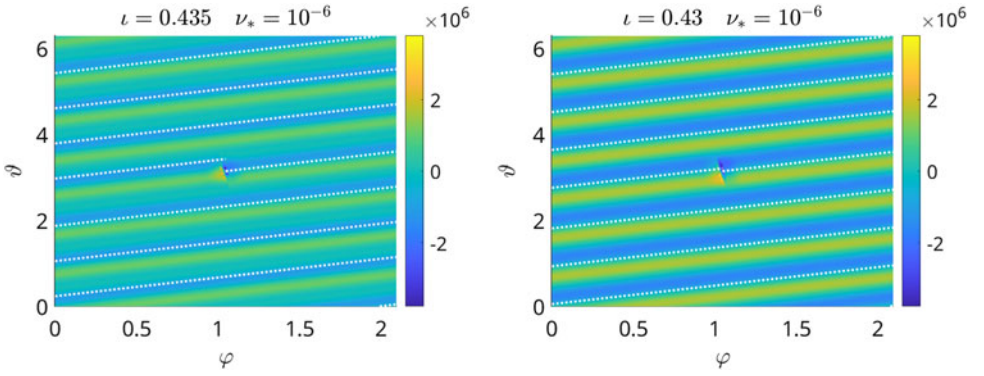

FIGURE 23. The same as figure 21 for $\nu_* = 10^{-6}$.

$\iota = 0.43$ is different amplitudes of straps on $g_{(3)}$ which, in fact, is higher for $\iota = 0.43$ where the off-set of λ_{bB} is smaller (see figure 20). Less visible is the split of the straps into the off-set domain and the main region for $\iota = 0.435$. Actually, this split is responsible for the lower amplitude of the straps in this case. Note that the strap structure and difference in its amplitude for two ι values transfers also to the angular distribution of radial particle flux shown in figure 24. Despite the factor 1.5 higher amplitude of the flux density modulation, the value of λ_{bB} is only 14 % different (and is lower) for $\iota = 0.43$ than for $\iota = 0.435$. The reason is the relatively low contribution of the strap structure dominating the plot to the radial transport because this contribution is mostly averaged to zero. Namely, change of $g_{(3)}$ along the straps (more precisely, along the field lines) is rather slow, but not slow is the change of local guiding center velocity which, at the end, results in much smaller bounce-averaged value actually contributing to the flux.

The appearance of strap structure on the generalized Spitzer function $g_{(3)}$, which only emerges in figure 21 and becomes dominant in figure 23, is connected with a certain paradox of the asymptotic solution of Helander *et al.* (2011) for trapped

https://doi.org/10.1017/S0022377825000200 Published online by Cambridge University Press

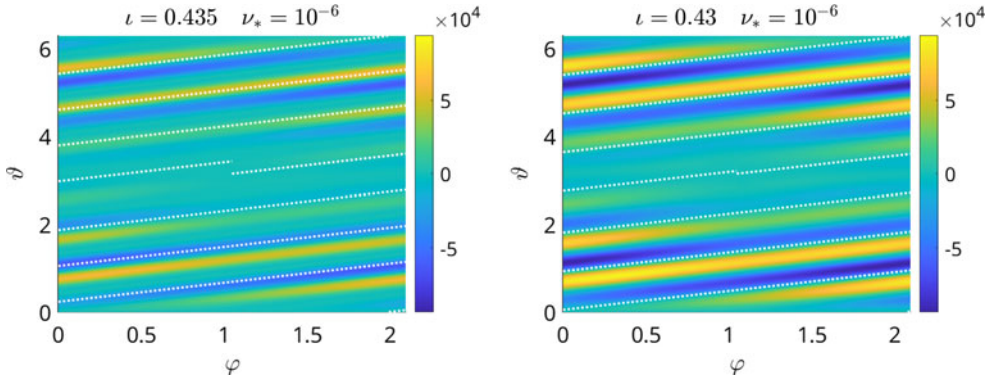

FIGURE 24. The same as figure 22 for $\nu_* = 10^{-6}$.

particles, g_0^t, given by (2.47) in § 2.2.2. Being perfectly correct and accurately reproduced at short field lines and the lowest collisionalities by NEO-2, it does not result in smooth distributions over irrational flux surfaces, but rather in the fractal structure with an infinite amplitude. Since two arbitrarily close points on the flux surface can be connected in the $1/\nu$ regime only along the field line, the connecting segment of the field line is in general infinite, which results in infinite values of the integral (2.47). As we saw already in § 2.3.2, this paradox is resolved for finite collisionality. Namely, whenever the field line enters the 'hot spot' (boundary layer), it starts a new segment which should be treated independently from the rest. Thus, the problem becomes local at finite collisionalities even at the irrational surfaces. With reducing ν_* the size of the 'hot spot' is reduced, and, at some point there will be a transition from a 7 strap structure to another structure with more straps. Finally, in the zero collisionality limit, the fractal structure of the solution of Helander *et al.* (2011) will be recovered. Of course, within this simple splitting approach combined with an asymptotic model, the fractal structure will not appear anymore but the off-set effect will naturally be different from the one in the collisional model.

The actual 'splitting' of the collisional solution for $\nu_* = 3 \cdot 10^{-4}$ is shown in figure 25, where the same distribution functions as in figure 21 are plotted along two field lines as functions of the number of toroidal turns $(\varphi - \varphi_0)/(2\pi)$. The first line starts from the global maximum $(\vartheta_0, \varphi_0) = (\pi, \pi/3)$, and the second one starts from the close point with $\vartheta = \vartheta_0 + \delta\vartheta$. Together with solutions of NEO-2 for two ι values, also plotted is the asymptotic solution of Helander *et al.* (2011), (2.47), which has the form of a straight line in Boozer coordinates, $g_0^t = (\iota B_\vartheta + B_\varphi)(\varphi - \varphi_0)$. In the left plot, one can observe the same pattern consisting of the 'main region' and two off-set domains (this case is similar to the one in figure 6) repeated three times, which corresponds to a 'resonance' with $\iota = 3/7$ (note that $0.435 - 3/7 \approx 0.0064$ and $0.43 - 3/7 \approx 0.0014$). One can also see that g_0^t well represents the solution within each domain up to a constant shift introduced by splitting in the boundary layers. Spikes on $g_{(3)}$ correspond to the contact with the trapped–passing boundary layer ('hot spots'), and one can see nearly no spikes at the transitions between the off-set domains and the main region, which correspond to the boundary layers between trapped particle classes. One can also see slow accumulation of a different type of off-set in the main regions, which results in a different $g_{(3)}$ pattern in the long run (see the right plot). This off-set, however, has a much smaller effect on λ_{bB} (see

https://doi.org/10.1017/S0022377825000200 Published online by Cambridge University Press

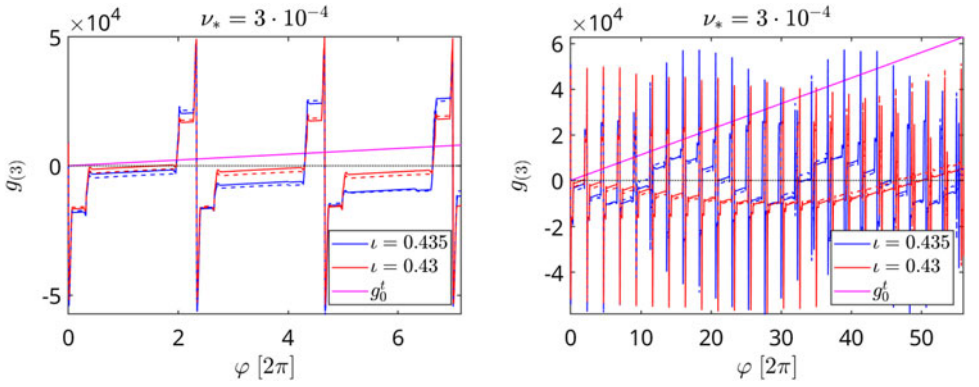

FIGURE 25. Generalized Spitzer function $g_{(3)}$ along the field line starting from global maximum (solid) and from the close point displaced by $\Delta\vartheta = 0.03$ (dashed) for $\iota = 0.435$ (blue) and $\iota = 0.43$ (red) and $\nu_* = 3 \cdot 10^{-4}$. The magenta line shows the asymptotic solution g_0^t, (2.47), at the first field line. Left and right plots show the same for 7 and 56 periods, respectively.

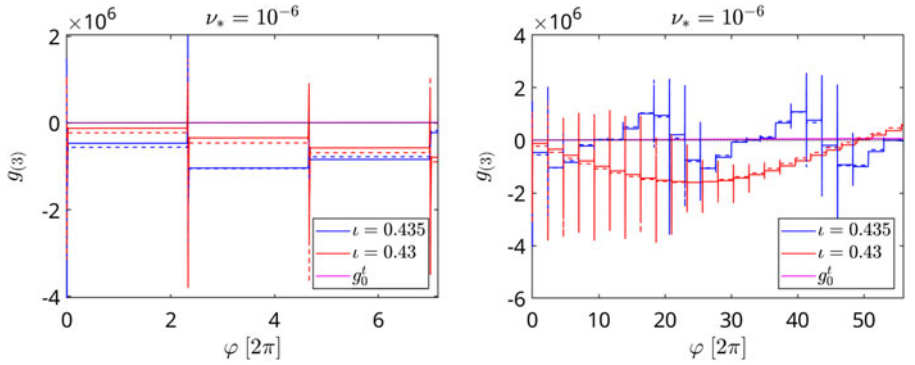

FIGURE 26. The same as figure 25 for $\nu_* = 10^{-6}$ and $\Delta\vartheta = 0.01$.

figure 20) because the bounce-averaged velocity for relatively long 'main regions' is much smaller than for the short off-set domains.

Short off-set domains fully disappear at lower collisionality $\nu_* = 10^{-6}$, as shown in figure 26. There, the off-set pattern in the long run determines λ_{bB}, which shows then in figure 20 a significant difference for the two ι values under examination here. We see that this pattern is formed by sub-domains with toroidal extent corresponding to a full poloidal turn of the field line. For the case $\iota = 0.435$, the pattern is repeated twice in the long run and is formed by the 'main region' consisting of 3 sub-domains (field line misses the boundary layer during these full poloidal turns), and there are 3 off-set domains on each side of the main region with the opposite off-set value in each triple (field line visits the boundary layer within these sub-domains at opposite sides for each triple). One can see also 'symmetric' sub-domains with nearly no off-set, which separate the patterns approximately repeated after 25 toroidal turns. In contrast, for $\iota = 0.43$, almost a harmonic structure is formed with a period determined by $\Delta\iota = 0.44 - 0.43 = 0.01$.

https://doi.org/10.1017/S0022377825000200 Published online by Cambridge University Press

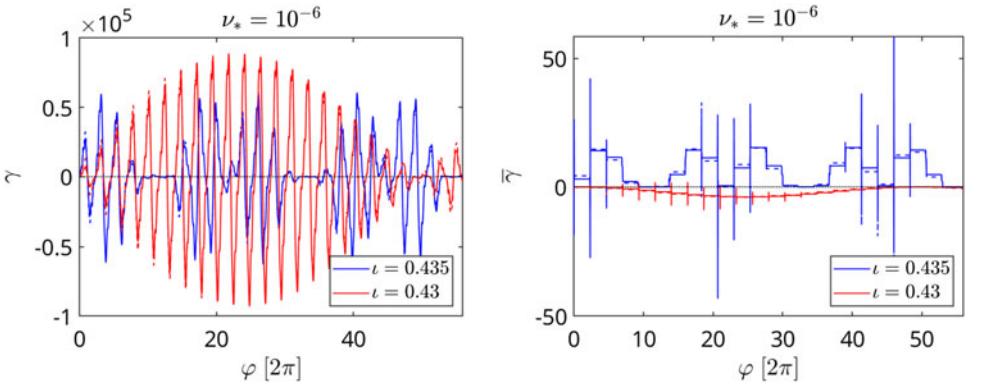

FIGURE 27. Normalized trapped particle radial flux angular density γ (left) and sub-domain average $\bar{\gamma}$ (right) for the distribution functions shown in figure 26.

Finally, the normalized trapped particle radial flux distribution over the angles $\gamma = \mathcal{V} g_{(3)}$ (the same quantity as in figure 24) and the sub-domain average $\bar{\gamma} = \langle \mathcal{V} \rangle_\vartheta g_{(3)}$m where $\langle \mathcal{V} \rangle_\vartheta$ are averages over the field line segments corresponding to one poloidal turn (i.e. these are integrals in (3.59) normalized by $\varphi_{j+1} - \varphi_j$ with $[\varphi_j, \varphi_{j+1}]$ being the sub-domain) are shown in figure 27 for the same field lines as in figure 26 and $\nu_* = 10^{-6}$. It can be seen that large oscillations on the local flux density γ are mostly averaged off within sub-domains, and the resulting sub-domain average $\bar{\gamma}$ which is determined mainly by the bounce-averaged radial drift shows the significant positive contribution of the off-set domains for $\iota = 0.435$ and a smaller negative contribution for $\iota = 0.43$ (in agreement with the trend in figure 20).

4.2. *Asymptotic behavior at irrational surfaces*

For estimation of the λ_{bB} trend with $\nu_* \to 0$ we analyze the nearly periodic pattern seen in right plots of figures 26 and 27 (such a pattern is seen also in the left plot of figure 25 while the right plot shows the overlay of two patterns). This pattern is formed if the field line starting in close vicinity to the global maximum point $(\vartheta_{\max}, \varphi_{\max})$, i.e. at the point $(\vartheta_0, \varphi_0) = (\vartheta_{\max} + \Delta\vartheta_0, \varphi_{\max})$ where $\Delta\vartheta_0 \ll \delta\vartheta$ and $\delta\vartheta$ is the poloidal boundary layer width (width of 'hot spots' in figures 21 and 23), returns after N turns back to this vicinity, $(\vartheta_N, \varphi_N) = (\vartheta_{\max} + \Delta\vartheta_N, \varphi_{\max})$ with $\Delta\vartheta_N \ll \delta\vartheta$. The off-set pattern is formed if within these N turns at least one approximate match occurs at some $(\vartheta, \varphi) = (\vartheta_{\max} + \Delta\vartheta, \varphi_{\max})$ with $\Delta\vartheta_0 \ll \Delta\vartheta \leqslant \delta\vartheta$. By the symmetry argument (one can make N turns backwards), such matches come in pairs, thus forming one 'main region' and at least two off-set domains with positive and negative off-sets, respectively (see the left plot in figure 25 and the right plots in figures 26 and 27 where six off-set domains are formed for $\iota = 0.435$).

Expanding the magnetic field around the global maximum point

$$B(\vartheta_{\max} + \Delta\vartheta, \varphi_{\max} + \Delta\varphi) \approx B_{\max} + \frac{1}{2\beta} \frac{\partial^2 B}{\partial \vartheta^2} \left(\beta \Delta\vartheta^2 + \Delta\varphi^2 \right),$$
$$\beta = \frac{\partial^2 B}{\partial \vartheta^2} \left(\frac{\partial^2 B}{\partial \varphi^2} \right)^{-1}, \tag{4.1}$$

https://doi.org/10.1017/S0022377825000200 Published online by Cambridge University Press

where the second derivatives correspond to the global maximum point, and the mixed derivative there is zero for our example (2.57), we can relate the distance $\Delta\eta$ between class-transition boundary $\eta = \eta_c = 1/B_{\max}^{\mathrm{loc}}$ and trapped–passing boundary $\eta = \eta_b = 1/B_{\max}$ to the poloidal distance $\Delta\vartheta$ between the respective local maximum and the global maximum as

$$\Delta\eta \approx \frac{1+\iota^2\beta}{2B_{\max}^2}\left|\frac{\partial^2 B}{\partial\vartheta^2}\right|\Delta\vartheta^2. \tag{4.2}$$

We have expressed here the toroidal distance between these maxima as $\Delta\varphi = -\iota\beta\Delta\vartheta$, which follows from the local maximum condition $\mathbf{h}\cdot\nabla B = 0$ and (4.1). Assuming that rational numbers $0 < m/n < 1$ with $n < N_{\max}$ are distributed uniformly in this interval (which is generally not true but gives a correct order of magnitude estimate), we obtain for the best match at some $n = N$ that

$$\min_{m,n\leqslant N_{\max}} |\iota n - m| \sim 1/N_{\max} \sim 1/N. \tag{4.3}$$

Thus, a field line starting at a global maximum will be displaced from this maximum after N toroidal turns by $\Delta\vartheta_N \sim 2\pi/N$ and, according to (4.2), pass through the local maximum with respective class boundary η_c displacement $\Delta\eta_N = \eta_c - \eta_b$ given by

$$\Delta\eta_N \approx \frac{2\pi^2\varepsilon_t\eta_b}{N^2}, \tag{4.4}$$

where we denoted $\varepsilon_t \equiv (1+\iota^2\beta)\eta_b\left|\partial^2 B/\partial\vartheta^2\right|$ well represented by field modulation in an axisymmetric tokamak. The trapped–passing boundary layer width corresponding to N toroidal turns is given by (3.20) with $\varphi = \varphi_0$ and $\varphi' = \varphi_0 + 2\pi N$ resulting in the estimate

$$\delta\eta \approx 4\pi^{-1/2}(2\varepsilon_t)^{1/4}\eta_b\,(\nu_* N)^{1/2}, \tag{4.5}$$

obtained here for $\varepsilon_M \ll \varepsilon_t \ll 1$ (see (2.57)) and using $\iota B_\vartheta + B_\varphi \approx R/\eta_b$. Since the poloidal width of the boundary layer $\delta\vartheta$ and boundary layer width $\delta\eta$ are related by (4.2) with replacement $\Delta \to \delta$, the best match after N turns completing the off-set pattern means $\Delta\eta_N \ll \delta\eta$, which, according to (4.4) and (4.5), results in

$$N \gg \frac{\pi\varepsilon_t^{3/10}}{\sqrt{2}\nu_*^{1/5}}, \qquad \delta\eta \gg 4\eta_b\,(\varepsilon_t\nu_*)^{2/5}. \tag{4.6}$$

The last expression (4.6) agrees with the ν_* scaling of the boundary layer width obtained by a similar argument in Helander, Parra & Newton (2017). Since $\Delta\eta_N/\delta\eta \sim N^{-5/2}$ rapidly decays with N, strong inequality (4.6) is achieved even if one only doubles the N value given by the right-hand side. Therefore, we use (4.6) further, as order of magnitude estimates rather than strong conditions. Assuming for simplicity then only one pair of off-set domains is formed with local minimum mis-match of the order of the boundary layer width in the main region, $\Delta\eta \sim \delta\eta_{\mathrm{ref}}$ and estimating this width in the large aspect ratio limit as $\delta\eta_{\mathrm{ref}} \sim \delta\eta \sim 4\eta_b\,(\varepsilon_t\nu_*)^{2/5}$, we obtain the distribution function in the off-set domains with the help of (3.52), (3.46) and estimate $\alpha_{mr}^{\pm} \sim 1$ due to $x_{\pm 0} \sim \Delta\eta/\delta\eta_{\mathrm{ref}} \sim 1$ as

$$g_{\mathrm{off}}^{(j)} \sim RB_0\varepsilon_t^{-1/10}\nu_*^{-3/5}, \tag{4.7}$$

https://doi.org/10.1017/S0022377825000200 Published online by Cambridge University Press

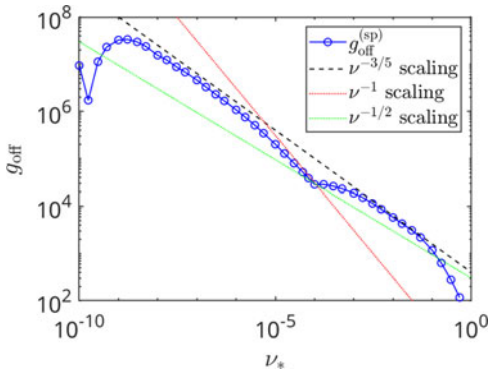

FIGURE 28. Span of the generalized Spitzer function $g_{\rm off}^{\rm (sp)} \equiv (\max(g_{(3)}) - \min(g_{(3)}))/2$ for standing particles, $\lambda = 0$, at $\varphi = 0$ as a function of collisionality (case $\iota = 0.435$ in figure 20). Scalings $\nu_*^{-3/5}$, $1/\nu_*$ and $1/\sqrt{\nu_*}$ are shown by black dashed, red and green dotted lines, respectively.

where $B_0 = B_{\max}$, and constant (3.18) has been estimated as $C_0 \sim R B_0^2/(\nu_* \varepsilon_t^{1/2})$. Note that scaling (4.7) is reproduced up to a factor 2 by the relation between the color ranges in figures 21 and 23 and is in good agreement with collisionality dependence of the span $g_{\rm off}^{\rm (sp)}$ of the generalized Spitzer function which corresponds to the maximum off-set at $\varphi = 0$ line (in particular, in figures 21 and 23), see figure 28.

It remains now to estimate the weighting factors $w_{\rm off}^{(j)}$ in (3.54) which results, for our near-periodic pattern with two similar off-set domains, in $\lambda_{\rm off} \sim g_{\rm off}^{(j)} w_{\rm off}^{(j)}$ with $j = 0$. Expanding the sub-integrand $\mathcal{V}$ in (3.59) in Fourier series over periodic Boozer angles

$$\mathcal{V}(\vartheta, \varphi) = \sum_{m=1}^{\infty} \sum_{n=-\infty}^{\infty} \mathcal{V}_{mn}^s(\eta) \sin(m\vartheta + n\varphi), \tag{4.8}$$

with $\eta = \eta_{\rm loc}^{(j)}$, this series has no $m = 0$ terms due to the last (3.60), where the derivative over ϑ_0 is the same as the derivative over ϑ. Here, we placed the origin of angles at the global B maximum to avoid cosine harmonics in stellarator-symmetric fields. Introducing the number of toroidal turns per off-set domain, $N_o \lesssim N$, we present $\iota = \iota_o + \delta\iota$, where $\iota_o = M_o/N_o$, M_o is the number of poloidal turns and $\delta\iota \ll 1$. The field line segment with the off-set domain starts at $(\vartheta, \varphi) = (\Delta\vartheta_0, 0)$ and ends at $(\vartheta, \varphi) = (2\pi M_o + \Delta\vartheta_N, 2\pi N_0)$, where $\Delta\vartheta_N = \Delta\vartheta_0 + 2\pi N_o \delta\iota$, and the tips of the transient banana orbit are located at $\left(\vartheta_{(j)}^-, \varphi_{(j)}^-\right) = (\Delta\vartheta_0 + \iota\delta\varphi_0, \delta\varphi_0)$ and $\left(\vartheta_{(j)}^+, \varphi_{(j)}^+\right) = (2\pi M_o + \Delta\vartheta_N + \iota\delta\varphi_N, 2\pi N_o + \delta\varphi_N)$, where $\delta\varphi_{0,N} \sim \max(|\Delta\vartheta_0|, |\Delta\vartheta_N||) \ll 1$ are toroidal shifts of those banana tips from the global maximum points, see figure 29. Replacing in $I_{\mathcal{V}}^{(j)}$, (3.59), the integrand $\mathcal{V}$ with $\mathcal{V}_b$ which is given by the same (3.60) with the replacement $\eta_{\rm loc}^{(j)} \to \eta_b$, extending there the integration interval to the whole off-set segment $0 < \varphi < 2\pi N_o$ and thus ignoring the shifts $\delta\varphi_{0,N}$, and expanding $\mathcal{V}_b$ around the helical line $\vartheta = \iota_o\varphi$ we get

https://doi.org/10.1017/S0022377825000200 Published online by Cambridge University Press

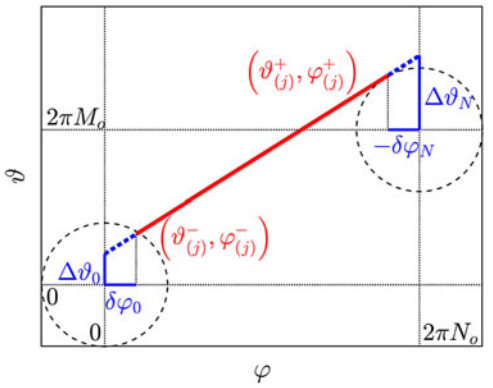

FIGURE 29. Field line segment containing the off-set domain (blue dotted) covered by transient banana orbit (red) in case the lower local field maximum is on the right, $\eta^{(j)}_{\rm loc} = \eta_{j+1}$. Dashed black ellipses correspond to the contour $\eta^{(j)}_{\rm loc} B(\vartheta, \varphi) = 1$.

$$I^{(j)}_{\mathcal{V}} = \int\limits_{\varphi^-_{(j)}}^{\varphi^+_{(j)}} \mathrm{d}\varphi\, \mathcal{V}\left(\Delta\vartheta_0 + \iota\varphi, \varphi\right) \tag{4.9}$$

$$\approx \int\limits_0^{2\pi N_o} \mathrm{d}\varphi \left(\mathcal{V}_b(\iota_o\varphi, \varphi) + \mathcal{V}'_b(\iota_o\varphi, \varphi)(\Delta\vartheta_0 + \delta\iota\,\varphi) + \frac{1}{2}\mathcal{V}''_b(\iota_o\varphi, \varphi)(\Delta\vartheta_0 + \delta\iota\,\varphi)^2 \right),$$

where $\mathcal{V}'_b$ and $\mathcal{V}''_b$ denote the first and second derivatives of $\mathcal{V}_b(\vartheta, \varphi)$ over ϑ. The first two approximations in (4.9) skip negligibly small terms of the order of $\Delta\vartheta^3_{0,N}$. To check that we notice that derivative $\partial B/\partial\vartheta_0$ in (3.60) vanishes at the global maximum and, therefore, scales in the additional integration intervals $0 < \varphi < \varphi^-_{(j)}$ and $\varphi^+_{(j)} < \varphi < 2\pi N_o$ as $\partial B/\partial\vartheta_0 \propto \Delta\vartheta_{0,N}$. The same scaling is true there for the square root term $(1 - \eta_b B)^{1/2} \propto \Delta\vartheta_{0,N}$. Thus, due to the scaling $\mathcal{V} \propto \Delta\vartheta^2_{0,N}$ in those intervals whose size is $|\delta\varphi_{0,N}|$, their overall contribution has a cubic scaling with $\Delta\vartheta_{0,N}$. The difference $\delta\mathcal{V} = \mathcal{V} - \mathcal{V}_b$ can be estimated as $\delta\mathcal{V} \propto \eta^{(j)}_{\rm loc} - \eta_b \propto \Delta\vartheta^2_{0,N}$ in the whole integration interval including the vicinity of its ends where $\delta\mathcal{V} \sim \mathcal{V}_b \propto \Delta\vartheta^2_{0,N}$. However, in the case of stellarator symmetry, $\delta\mathcal{V}$ is essentially an odd function of $\varphi - \pi N_o$, which does not contribute to the integral, while its even part $\delta\mathcal{V}^{even} \propto \Delta\vartheta^3_{0,N}$ respectively provides a negligible contribution $\propto \Delta\vartheta^3_{0,N}$. Since in the case of stellarator symmetry quantities $\mathcal{V}_b$ and $\mathcal{V}''_b$ are odd functions of $\varphi - \pi N_o$ while $\mathcal{V}'_b$ is an even function, we get

$$I^{(j)}_{\mathcal{V}} \approx \Delta\vartheta_{\rm mid} \int\limits_0^{2\pi N_o} \mathrm{d}\varphi \left(\mathcal{V}'_b(\iota_o\varphi, \varphi) + \delta\iota\,\mathcal{V}''_b(\iota_o\varphi, \varphi)(\varphi - \pi N_o) \right)$$

$$= 2\pi N_o \Delta\vartheta_{\rm mid} \sum_{m=1}^{\infty} \sum_{n=-\infty}^{\infty} m\mathcal{V}^s_{mn}(\eta_b) \left(\delta_{\rm res} + \frac{mN_o\delta\iota}{mM_o + nN_o}(1 - \delta_{\rm res}) \right), \tag{4.10}$$

https://doi.org/10.1017/S0022377825000200 Published online by Cambridge University Press

where $\delta_{\rm res}=1$ if $mM_o-nN_o=0$ and is zero otherwise, and $\Delta\vartheta_{\rm mid}=(\Delta\vartheta_0+\Delta\vartheta_N)/2$. Since only the resonant harmonics with $(m,n)=(N_ok,-M_ok)$ and $k=1,2,\ldots$ contribute to the first term, one can estimate $\sum\sum m\mathcal{V}^s_{mn}\delta_{\rm res}\sim N_o\mathcal{V}^s_{N_o,-M_o}$. For high harmonic indices, $m,n\to\infty$, spectrum of $\mathcal{V}$ is determined by the vicinity of the global maximum,

$$\mathcal{V}^s_{mn}(\eta_b)\approx\frac{9\beta^{1/2}\eta_b^{7/2}}{\sqrt{8}\pi}\left|\frac{\partial^2 B}{\partial\vartheta^2}\right|^{3/2}\frac{mN_{\rm tor}}{(m^2+\beta n^2)^{5/2}},\tag{4.11}$$

where $N_{\rm tor}$ is the number of toroidal field periods and $\mathcal{V}^s_{mn}=0$ for n which are not multiples of $N_{\rm tor}$, see Appendix A. Therefore, contribution of the first term $N_o\mathcal{V}^s_{N_o,-M_o}\sim N_o^{-3}$ is negligibly small compared with that of the second term which does not scale with N_o but contains small $\delta\iota$. Using $2\pi N_o\delta\iota=\Delta\vartheta_N-\Delta\vartheta_0$ and the definition of $\Delta\vartheta_{\rm mid}$, we obtain the scaling $I^{(j)}_{\mathcal{V}}\propto(\Delta\vartheta_N^2-\Delta\vartheta_0^2)\propto N_o^{-2}\propto N^{-2}$ and respective estimates

$$w^{(j)}_{\rm off}\sim\frac{\varepsilon_t^{3/2}}{N^3}\frac{{\rm d}r}{{\rm d}\psi}\sim(\varepsilon_t\nu_*)^{3/5}\frac{{\rm d}r}{{\rm d}\psi},\qquad\lambda^{\rm max}_{\rm off}\sim\varepsilon_t^{1/2}RB_0\frac{{\rm d}r}{{\rm d}\psi}\sim\iota\lambda^{\rm tok}_{bB},\tag{4.12}$$

where we assumed the maximum distribution function off-set (4.7), used (4.6) and assumed $\varepsilon_M\sim\varepsilon_t$ and $\beta\sim1$. Thus, off-set of bootstrap coefficient $\lambda_{\rm off}$ in stellarator-symmetric fields does not decrease with reducing collisionality but has an aperiodic oscillatory behavior with oscillation amplitude $\lambda^{\rm max}_{\rm off}$ of the order of λ_{bB} for the equivalent tokamak (Boozer & Gardner 1990; Beidler *et al.* 2011),

$$\lambda^{\rm tok}_{bB}=1.46\iota^{-1}\varepsilon_t^{1/2}RB_0\frac{{\rm d}r}{{\rm d}\psi}=1.46\iota^{-1}\varepsilon_t^{-1/2},\tag{4.13}$$

see figure 20 where the factor $1.46\iota^{-1}\approx3.4$ agrees well with the relative off-set amplitude.

The off-set pattern corresponding to N toroidal turns is replaced by the pattern with a larger number of turns if collisionality decreases by a significant factor, and further collisionality decrease triggers another pattern change, etc. Respectively, the off-set of the bootstrap coefficient oscillates aperiodically with changing $\log\nu_*$ as seen in figure 20. This behavior is due to the structure of the off-set pattern which is formed at the field line segment between two local field maxima $j=0,N$ fulfilling strong alignment conditions $(\Delta\eta_0,\Delta\eta_N)\ll\delta\eta$ with $\delta\eta$ given by (4.5) and which necessarily contains one or more internal local maxima fulfilling a weak alignment condition $\Delta\eta\lesssim\delta\eta$ (they split the segment into off-set domains, e.g. two off-set domains and the main region in the simplest case). With decreasing collisionality, weakly aligned internal maxima become non-aligned, $\Delta\eta\gg\delta\eta$, which makes the variation of the distribution function off-set $g_{\rm off}$ within the segment and respective contribution of the given pattern to the off-set of λ_{bB} exponentially small. Consequently, the whole segment of the old pattern turns into a single off-set domain of the new, longer pattern limited at the ends by even better aligned local maxima such that they stay well aligned when one (or both) maxima at the ends of the former segment become only weakly aligned at some lower collisionality. The above transition is well seen in figures 25 and 26 where three complete off-set patterns at higher

https://doi.org/10.1017/S0022377825000200 Published online by Cambridge University Press

collisionality (left figure 25) turn into three off-set domains of a longer pattern at lower collisionality (left figure 26). Note that those domains contribute simultaneously to both off-sets, $g_{\rm off}^{\rm short}$ and $g_{\rm off}^{\rm long}$ with the first one being dominant at higher and the second one at lower collisionality. A kink on the collisionality dependence of a summary function $g_{\rm off}^{\rm (sp)} = \max(g_{\rm off}^{\rm short}, g_{\rm off}^{\rm long})$ shown in figure 28 is at the transition point $\nu_* = 10^{-4}$ where $g_{\rm off}^{\rm short} = g_{\rm off}^{\rm long}$. At this point, internal maxima of the long off-set domain are still well aligned, so that $g_{\rm off}^{\rm long}$ scaling with ν_* is similar to (3.53) which includes $1/\nu$ and $1/\sqrt{\nu}$ terms. Note that $g_{\rm off}^{\rm (sp)}$ in figure 28 by definition shows only the largest off-set within the pattern which generally contains more than two off-set domains (see figure 26). Therefore, location of $g_{\rm off}^{\rm (sp)}$ maximum at ν_* dependence needs not coincide with the location of respective λ_{bB} maximum, which is at lower ν_* in figure 20. The reason is that contributions of most off-set domains within the pattern tend to saturate and then vanish with decreasing ν_* earlier than $g_{\rm off}^{\rm (sp)}$ which is determined then by the off-set domain bounded by the best aligned local maxima. One should also note that another kink on $g_{\rm off}^{\rm (sp)}$ located in figure 28 at $\nu_* = 1.7 \cdot 10^{-10}$ is not the transition point of different off-set patterns but a point where the off-set for the same pattern changes sign due to the mirroring within trapped-passing boundary layer discussed, in particular, in § 3.1. As a result, the respective off-set of λ_{bB} in figure 20 changes sign too (similar to figure 2).

According to (4.2), better alignment of maxima at the off-set segment ends means smaller poloidal displacements $\Delta\vartheta_0$ and $\Delta\vartheta_N$ of these ends, which requires a decrease with the pattern length N of the difference $|\Delta\vartheta_N - \Delta\vartheta_0| = 2\pi|\iota N_p - M|$ where $N_p = N N_{\rm tor}$ is the (integer) number of toroidal field periods within the off-set pattern and integer M is the nearest to ιN_p. Thus, the increasing sequence of N_p corresponds to the sequence of the best Diophantine approximations M/N_p of (generally irrational) ι. These approximations are the convergents of ι representation by a simple continued fraction (see, e.g., Hardy & Wright (1985)). Therefore, an overall trend of the N_p series $N_p^{(k)}$, $k = 1, 2, \ldots$, is similar to that of geometrical progression, $N_p^{(k+1)} = b_k N_p^{(k)}$ with $b_k > 1$ such that $b_k - 1 \gtrsim 1$. Thus, due to $\nu_* \propto N_p^{-5}$ following from (4.6), a series of collisionalities $\nu_*^{(k)}$ corresponding to the dominance of pattern k in the off-set has similar geometrical trend, and a significant change in the off-set of λ_{bB} requires such a change of $\log \nu_*$.

Finally, in view of the off-set (4.12) being of the same order as the collisionless asymptotic (2.43), let us estimate the role of the correction term driven by the source (3.13) which has been ignored in the present analysis and estimated to have a vanishing effect with decreasing collisionality in a short field line example in § 3.4. Comparison of the asymptotic and numerical solutions in figure 25 shows an obvious feature which cannot be described by the leading-order off-set. Namely, instead of the continuous linear growth of g_o^t, numerical solution tends to a nearly periodic behavior with the period of the order of the off-set pattern length. In other words, finite collisionality provides an aperiodic correction term which nearly balances the aperiodic behavior of g_0^t (while the leading-order off-set provides only a nearly periodic correction contained in the off-set domains within the pattern). One can formally present this next-order correction as a 'staircase function', $\Delta g_{\rm off}^{\rm (tr)} = \sum_k C_k^{\rm (tr)} \Theta\left(\varphi - \varphi_k^{\rm (op)}\right)$, where $\varphi_k^{\rm (op)}$ are the boundaries of the off-set pattern

https://doi.org/10.1017/S0022377825000200 Published online by Cambridge University Press

(points of well aligned relevant maxima) and $C_k^{(\mathrm{tr})} = g_0^t\left(\varphi_{k-1}^{(\mathrm{op})}\right) - g_0^t\left(\varphi_k^{(\mathrm{op})}\right)$. Being of the same order as g_0^t which, due to its dependence on φ, makes an independent of collisionality contribution to λ_{bB} within each off-set pattern, the staircase function is constant within the pattern and, according to the first estimate (4.12), its contribution scales with collisionality. Namely, replacing the distribution function off-set $g_{\mathrm{off}}^{(j)}$ with $\Delta g_{\mathrm{off}}^{(\mathrm{tr})} \sim N N_{\mathrm{pt}}$ where N_{pt} is the number of patterns per closed field line (and N, as before, is the number of toroidal turns within the pattern), respective contribution to the bootstrap coefficient scales as $\Delta\lambda_{bB} \approx w_{\mathrm{off}}^{(j)} \Delta g_{\mathrm{off}}^{(\mathrm{tr})} \sim N_{\mathrm{pt}} N^{-2} \sim N_{\mathrm{pt}} \nu_*^{2/5}$.

Another feature demonstrated for the short field line in figure 8 is a split of the boundary layer caused by a strong alignment of relevant maxima. This split can also be formally described by a staircase function $\Delta g_{\mathrm{off}}^{(\mathrm{bl})} = \sum_k C_k^{(\mathrm{bl})} \Theta\left(\varphi - \varphi_k^{(\mathrm{op})}\right) \delta_{(\mathrm{b})}(\eta_b - \eta)$ where $\delta_{(\mathrm{b})}$ tends with vanishing collisionality to a δ-function and is localized within the boundary layer width $\delta\eta$ where it scales as $\delta\eta^{-1}$ at finite collisionality, whereas constants $C_k^{(\mathrm{bl})}$ are given by the integral in parentheses in (2.52) with the change of lower and upper limits to $\varphi_k^{(\mathrm{op})}$ and $\varphi_{k-1}^{(\mathrm{op})}$, respectively. Since $\Delta g_{\mathrm{off}}^{(\mathrm{bl})}$ is also a constant of φ within the pattern, its contribution to λ_{bB} can be estimated as $\Delta\lambda_{bB} \sim \Delta w_{\mathrm{off}}^{(j)} \Delta g_{\mathrm{off}}^{(\mathrm{bl})}$ where $\Delta g_{\mathrm{off}}^{(\mathrm{bl})} \sim N N_{\mathrm{pt}} \delta\eta^{-1}$, and the estimate $\Delta w_{\mathrm{off}}^{(j)} \sim N^{-1} \Delta I_{\mathcal{V}}^{(j)}$ follows from (3.59), where $\Delta I_{\mathcal{V}}^{(j)} \sim \delta\vartheta^3 \sim N^{-3}$ is the contribution of the boundary layer to the integral $I_{\mathcal{V}}^{(j)}$ (this estimate is similar to the estimate of the error due to the finite $\eta_{\mathrm{loc}}^{(j)} - \eta_b$ below (4.9)). Finally, we obtain $\Delta\lambda_{bB} \sim N_{\mathrm{pt}} N^{-3} \delta\eta^{-1} \sim N_{\mathrm{pt}} N^{-1} \sim N_{\mathrm{pt}} \nu_*^{1/5}$ where we used (4.6) treated again as an approximate equality instead of a strong inequality. Thus, despite a visible effect on the generalized Spitzer function $g_{(3)}$, the ignored correction provides to the bootstrap coefficient a contribution which is converging to zero with decreasing collisionality.

It should be noted that scaling $\Delta\lambda_{bB} \propto N_{\mathrm{pt}}$ with the number of off-set patterns within the closed field line is the result of the 'worst case' estimate allowing for 'bootstrap resonances' discussed below in § 4.4. Such a crude 'worst case' estimate of the collisionless asymptotic $\lambda_{bB}^{\dagger}$ in the form (2.56) results in a similar scaling with the field line length which, in turn, does not contain the collisionality dependence.

4.3. *Off-set of bootstrap/Ware-pinch coefficient in case of (nearly) aligned maxima*

In the advanced stellarator configurations aiming at good confinement of fusion alpha particles, global magnetic field maxima tend to be aligned. This is the case in ideal quasi-symmetric configurations (Nührenberg & Zille, 1988) and also in quasi-isodynamic configurations with poloidally closed contours $B = \mathrm{const}$ (Mikhailov *et al.* 2002; Subbotin *et al.* 2006). If these configurations are not realized exactly, poloidal (helical in the general case of quasi-symmetry) closure of $B = \mathrm{const}$. contours is destroyed, in particular, near the field maximum where these contours split into islands centered around the global maxima reached at one or few points instead of lines. Local maxima $\mathbf{h} \cdot \nabla B = 0$, nevertheless, stay on poloidally closed contours defined in periodic Boozer coordinates by $\varphi = \varphi_k^{\mathrm{loc}}(\vartheta)$ where $\varphi_k^{\mathrm{loc}}(\vartheta) = \varphi_0^{\mathrm{loc}}(\vartheta) + 2\pi k / N_{\mathrm{tor}}$ with k being an integer, and where $\varphi_0^{\mathrm{loc}}(\vartheta)$ is periodic. For simplicity, we restrict our analysis here to the case of poloidally closed contours where also the family of anti-sigma configurations (3.36) belongs as a sub-class with

https://doi.org/10.1017/S0022377825000200 Published online by Cambridge University Press

$\varphi_0^{\rm loc}(\vartheta)=0$. We assume that these local maxima are close to global such that perturbation $\Delta B_{\rm loc}(\vartheta)\equiv B(\vartheta,\varphi_0^{\rm loc}(\vartheta))-\bar{B}_{\max}$ of the global maximum $\bar{B}_{\max}$ achieved in the ideal (unperturbed) configuration on a line is small. Since $(\vartheta,\varphi)=(0,0)$ is a stellarator symmetry point associated with field maximum, function $\varphi_0^{\rm loc}(\vartheta)$ is odd and $\Delta B(\vartheta)$ is even.

It is convenient now to label the field lines by the poloidal angle in the middle of the first field period where $\varphi=\varphi_s\equiv\pi/N_{\rm tor}$ such that $(\vartheta,\varphi)=(0,\varphi_s)$ is a stellarator symmetry point associated with field minimum of the ideal configuration. Namely, we label them with $\vartheta_0=\vartheta-\iota(\varphi-\varphi_s)=\vartheta-\iota\varphi+\iota_p$ where $\iota_p=\iota\varphi_s$. Positions of local maxima on the so labeled field line, $\varphi_k=\varphi_k(\vartheta_0)$, being the solutions to $\varphi_k=\varphi_k^{\rm loc}\,(\vartheta_0+\iota(\varphi_k-\varphi_s))$ for $-\infty<k<\infty$ can all be expressed via the left maximum of the first period φ_0 on the re-labeled field line as $\varphi_k(\vartheta_0)=\varphi_0\left(\vartheta_0+2k\iota_p\right)+2k\varphi_s$. Respective perturbations $\Delta B_{(k)}(\vartheta_0)$ of global maximum at these points can be expressed via such perturbation $\Delta B_{(0)}$ of the left maximum in the first period as $\Delta B_{(k)}(\vartheta_0)=\Delta B_{(0)}(\vartheta_0+2k\iota_p)$. Finally, integrals (2.26) where $\varphi_j^-=\varphi_j$ and $\varphi_j^+=\varphi_{j+1}$ can be mapped to the first period similarly, $I_k(\vartheta_0,\eta)=I_0(\vartheta_0+2k\iota_p,\eta)$.

Due to stellarator symmetry, function $\varphi_0(\vartheta_0)$ is odd with respect to $\vartheta_0-\iota_p$, i.e. $\varphi_0(2\iota_p-\vartheta_0)=-\varphi_0(\vartheta_0)$, while function $\Delta B_{(0)}$ is even. It convenient to express the latter via an even function of the argument $\Delta B(\vartheta')$ as $\Delta B_{(0)}(\vartheta_0)=\Delta B(\vartheta_0-\iota_p)$, such that for anti-sigma configurations we have an identity $\Delta B(\vartheta)=\Delta B_{\rm loc}(\vartheta)=B(\vartheta,0)-\bar{B}_{\max}$. We fix $\bar{B}_{\max}$ by the condition of zero average, $\overline{\Delta B}=0$ such that an even function $\Delta\eta(\vartheta)=-\Delta B(\vartheta)/\bar{B}_{\max}^2$ has zero average too. Using definition (3.30) of the aspect ratio, its perturbation is given by $\Delta A_o(\vartheta_0)=(I_{\rm ref}/I_0(\vartheta_0,\eta_b))^{1/2}-1$ being an even function with $I_{\rm ref}$ determined by the condition of zero average $\overline{\Delta A_o}$.

Mapping to the first period of the distribution function off-set given by (3.53) for small $\Delta A_o\ll 1$ and $\Delta\eta\ll\delta\eta_{\rm ref}$ is similar to that of the other quantities, $g_{\rm off}^{(0)}(\vartheta_0)=g_{\rm off}^{(k)}(\vartheta_0-2k\iota_p)$. Since (3.53) gives the off-set in open-ended system with sources located in a single period, solution for the closed (periodic) system with sources in each period is an odd function given by the sum over all periods of the open ended system

$$g_{\rm off}(\vartheta)=\sum_{k=-\infty}^{\infty}g_{\rm off}^{(k)}(\vartheta_0-2k\iota_p),\tag{4.14}$$

which is expressed via even functions ΔA_o and $\Delta\eta$ as

$$g_{\rm off}(\vartheta_0)=\frac{l_c}{4}\left(\frac{\langle B^2\rangle}{\langle|\lambda|\rangle}\right)_{\eta=\eta_b}\sum_{k=1}^{\infty}\Big(\sqrt{2}\delta\eta_{\rm ref}\Delta_k^A\left(\Delta A_o\left(\vartheta_0-2\iota_p k\right)-\Delta A_o\left(\vartheta_0+2\iota_p k\right)\right)$$
$$+\,\Delta_k^B\left(\Delta\eta\left(\vartheta_0-\iota_p(2k-1)\right)-\Delta\eta\left(\vartheta_0+\iota_p(2k-1)\right)\right)\Big).\tag{4.15}$$

Respectively, the off-set of the Ware-pinch coefficient (3.54) is expressed in the limit of infinite (irrational) field-line length via $g_{\rm off}$ as follows:

https://doi.org/10.1017/S0022377825000200 Published online by Cambridge University Press

$$\lambda_{\rm off}\int\limits_0^{2\pi} {\rm d}\vartheta_0 \int\limits_0^{2\pi/N_{\rm tor}} \frac{{\rm d}\varphi}{B^2} \approx \frac{{\rm d}r}{{\rm d}\psi}\int\limits_0^{2\pi} {\rm d}\vartheta_0\, g_{\rm off}(\vartheta_0) I_{\mathcal V}(\vartheta_0) = \pi \frac{{\rm d}r}{{\rm d}\psi}\sum_{m=1}^{\infty} g_m I_{\mathcal V}^m, \tag{4.16}$$

where an odd function $I_{\mathcal V}(\vartheta_0)$ is given by the second (3.59) with $\varphi_{(j)}^- = \varphi_0(\vartheta_0)$ and $\varphi_{(j)}^+ = \varphi_1(\vartheta_0)$, and we used (an odd) Fourier series expansion

$$(g_{\rm off}(\vartheta_0),\, I_{\mathcal V}(\vartheta_0)) = \sum_{m=1}^{\infty}(g_m,\, I_{\mathcal V}^m)\,\sin(m\vartheta_0). \tag{4.17}$$

Coefficients g_m are expressed via coefficients of (an even) Fourier series expansion

$$(\Delta A_o(\vartheta),\, \Delta B(\vartheta)) = \sum_{m=1}^{\infty}(\Delta A_o^m,\, \Delta B_m)\cos(m\vartheta), \tag{4.18}$$

as follows:

$$g_m = \frac{l_c}{2}\left(\frac{\langle B^2\rangle}{\langle|\lambda|\rangle}\right)_{\eta=\eta_b}\left(\sqrt{2}\delta\eta_{\rm ref} S_A(m\iota_p)\Delta A_o^m - \eta_b^2 S_B(m\iota_p)\Delta B_m\right), \tag{4.19}$$

where

$$S_A(\phi) = \sum_{k=1}^{\infty}\Delta_k^A \sin(2k\phi)\,, \qquad S_B(\phi) = \sum_{k=1}^{\infty}\Delta_k^B \sin((2k-1)\phi)\,. \tag{4.20}$$

These functions have period 2π and are well approximated in the interval $-\pi < \phi < \pi$ by $S_A(\phi) \approx 0.26\,(\phi - (\pi/2){\rm sign}(\phi))$ and $S_B(\phi) \approx 1.85\,{\rm sign}(\phi)$.

For the estimates, we apply general expressions (4.15)–(4.19) to the anti-sigma configuration (3.36) which corresponds to the perturbed case 3 with $\varepsilon_0 = \varepsilon_M \ll 1$, $\varepsilon_1 = \varepsilon_t \ll \varepsilon_M$ and $\varepsilon_3 = 0$

$$B(\vartheta,\varphi) = B_0\,(1 + \varepsilon_M\cos(N_{\rm tor}\varphi) + \varepsilon_t\cos\vartheta\,(1 - \cos(N_{\rm tor}\varphi))) + \Delta B_1\cos\vartheta. \tag{4.21}$$

In the leading order over $\varepsilon_t/\varepsilon_M$ and $\Delta B_1/B_0$, only $A_o^1 \approx \varepsilon_t/(2\varepsilon_M)$ harmonic and ΔB_1 harmonic contribute to $\lambda_{\rm off}$ because of the dominance in the $I_{\mathcal V}$ spectrum of harmonic $I_{\mathcal V}^1 \approx -8\varepsilon_t(2\varepsilon_M)^{1/2}(B_0^2 N_{\rm tor})^{-1}$. Estimating $l_c = \pi R/(2\nu_*)$, $\langle B^2\rangle \approx B_0^2$, $\eta_b \approx 1/B_0$, $\langle|\lambda|\rangle_{\eta=\eta_b} \approx \pi^{-1}(8\varepsilon_M)^{1/2}$ and $\delta\eta_{\rm ref} \sim 4\pi^{-1/2}(2\varepsilon_M)^{1/4}(\nu_*/N_{\rm tor})^{1/2}B_0^{-1}$ we get

$$\begin{aligned}\lambda_{\rm off} &\approx -\varepsilon_t R B_0 \frac{{\rm d}r}{{\rm d}\psi}\left(\left(\frac{2\pi}{\nu_* N_{\rm tor}}\right)^{1/2}\frac{\varepsilon_t S_A(\iota_p)}{(2\varepsilon_M)^{3/4}} - \frac{\pi\Delta B_1 S_B(\iota_p)}{4\nu_* B_0}\right)\\ &\approx \lambda_{bB}^{\rm tok}\left(\frac{0.42\,|\iota|\,\varepsilon_t^{3/2}}{(\nu_* N_{\rm tor})^{1/2}\,\varepsilon_M^{3/4}}\left(1 - \frac{2|\iota|}{N_{\rm tor}}\right) + \frac{|\iota|\,\varepsilon_t^{1/2}\Delta B_1}{\nu_* B_0}\right).\end{aligned} \tag{4.22}$$

The black dotted line showing the trend in figure 14 actually corresponds to the result of this formula for case 3.

It should be reminded here that the off-set (4.22) due to violation of ripple equivalence appears only for relatively strong alignment of maxima,

https://doi.org/10.1017/S0022377825000200 Published online by Cambridge University Press

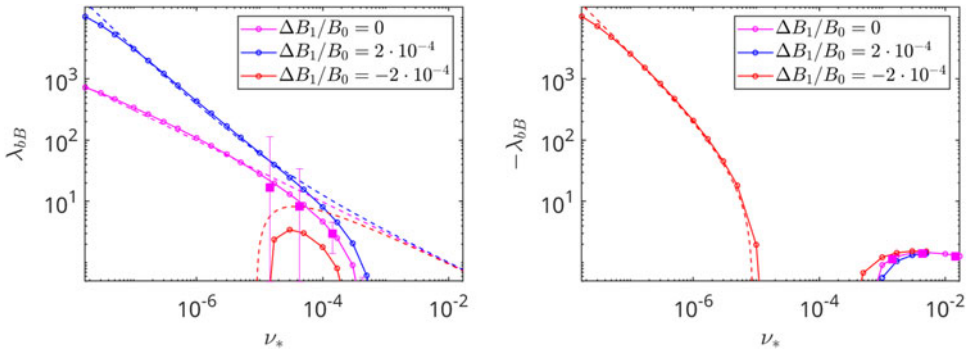

FIGURE 30. Geometrical factor λ_{bB} computed by NEO-2 (circles) and DKES (filled squares) vs ν_*. Three different maximum-B perturbations are marked with colors (see the legend). Dashed lines correspond to the asymptotic (4.22). Negative λ_{bB} are shown in the right plot.

$\Delta B/B_0 \lesssim (\nu_*/N_{\rm tor})^{1/2}\varepsilon_M^{1/4}$, and the validity of estimate (4.22) requires the respective strong inequality. In the marginal case where an approximate equality is realized, the largest off-set, $\lambda_{\rm off} \sim \lambda_{bB}^{\rm tok}\, \varepsilon_t^{1/2}\varepsilon_M^{1/4}\, (\nu_* N_{\rm tor})^{-1/2}$ occurs. The result of a small misalignment of maxima due to a finite perturbation ΔB_1 in (4.21) is shown in figure 30. Note that the validity condition of a linear asymptotic (4.22) becomes violated for finite ΔB_1 at $\nu_* = 1.7 \cdot 10^{-8}$ where $\Delta\eta = \delta\eta_{\rm ref}$, and the case of nearly aligned maxima starts a transition to the usual case of a global maximum reached at a point.

4.4. *Bootstrap resonances*

As one can conclude from figure 20, resonance structure of ι (equivalently, of radial) dependence of bootstrap coefficient is absent in finite collisionality cases (see also figure 16 of Landreman *et al.* 2022). This, however, does not mean that these resonances never play a role. The reason for them is the following (see also the Appendix of Boozer & Gardner 1990). By our assumption, the magnetic configuration has embedded flux surfaces everywhere so that magnetic islands are absent at any rational magnetic surface, which is manifested by a true surface condition (2.41). Although these configurations constitute a set of measure zero, they are physically possible. It is straightforward to check that the first term (representing the Pfirsch–Schlüter current) in (2.43) is never resonant as long as conditions (2.41) are fulfilled. However, this is not the case for the second term. Up to a flux surface function, the sub-integrand of the field line integral there is the derivative over η of the source term $s_{(1)}$, (2.3), which fulfills the quasi-Liouville theorem (2.15) at our representative field line, but not necessarily on the other field lines from the same rational surface. In other words, the amplitudes of resonant harmonics fulfilling $\iota m + n = 0$ for our rational surface are generally finite, but these are harmonics of $\sin(m\vartheta + n\varphi) = \sin(m\vartheta_0 + n\varphi_0 + (\iota m + n)(\varphi - \varphi_0))$ which are identical zeros for the starting point (ϑ_0, φ_0) being a stellarator symmetry point. Would those amplitudes be all zero, the integral over any field line would be a single-valued function fulfilling then a quasi-Liouville theorem (2.15) for passing particles and, as a consequence, conditions $\oint \mathrm{d}l\, v_\parallel = \text{const}$ evaluated for passing particles along closed field lines (see the discussion by Shaing & Callen (1983) after equation (44*b*)), which actually mean 'true surface' conditions for the effective magnetic field $\mathbf{B}^*$ (Morozov &

https://doi.org/10.1017/S0022377825000200 Published online by Cambridge University Press

Solov'ev 1966), i.e. for drift surfaces. The latter, however, need not have the same topology as the magnetic surfaces (see, e.g. Heyn *et al.* 2012) and, at best, can be made embedded for one particular η value for the cost of destroyed magnetic surfaces and drift surfaces with different η (actually, true drift surface conditions reduce for $\eta = 0$ to true magnetic surface conditions). Thus, drift islands are generally present at any rational drift surface (see, e.g. Smirnova 1997), and, due to the increased spectral width of $s_{(1)}$ near the trapped–passing boundary (Boozer & Gardner 1990) where the exponential decay of $s_{(1)}$ spectrum is replaced with a power law, $(mB_\varphi - nB_\vartheta)(m^2 + \beta n^2)^{-3/2}$ estimated similarly to (4.11), drift islands overlap near this boundary ($s_{(1)} = -\,\mathrm{d}r/\,\mathrm{d}\varphi$ along the orbits by definition (2.4)). This leads to barely trapped alpha particle losses observed in realistic stellarator configurations (Albert *et al.* 2020*a*,*b*, 2023; Chambliss, Paul & Hudson 2024), which do not ideally fulfill the quasi-symmetry conditions.

Due to our choice of reference field lines, respective drift orbits correspond to invariant axes (X or O points of drift islands), i.e. exact resonance does not destroy their closure and, therefore, does not affect collisionless λ_{bB}. However, neighboring resonances result in near resonant contributions to the collisionless $\lambda_{bB} \propto (\iota m - n)^{-1}$ where the denominator is rather close to zero, $\min(\iota m - n) = m\Delta\iota \lesssim 1/n$. One should note that exponential decay of the spectrum is restored from the power law decay for passing particles displaced from the separatrix by $\Delta\eta = \eta - \eta_b$ and mode numbers fulfilling $m^2 + \beta n^2 > (\eta_b^2/\Delta\eta)\partial^2 B/\partial\vartheta^2$. Therefore, contribution of near-resonant modes with high m and n to the integral over η in (2.43) scales with a maximum $\Delta\eta$ which still allows the power law decay, i.e. it is $\propto m^{-1}\Delta\iota^{-1}(m^2 + \beta n^2)^{-2}(mB_\varphi - nB_\vartheta) \propto \Delta\iota^{-1}m^{-4}$. Would the rational numbers be evenly distributed over the real axis as we assumed for simplicity in § 4.2, then $\Delta\iota \sim 1/m^2$, and the contribution of near-resonant modes is $\propto m^{-2}$, i.e. it is relatively small. However, uniform distribution is not the case in reality (see, e.g. figure 5 in Kasilov *et al.* 2002). Namely, if λ_{bB} asymptotic is evaluated at a high-order rational surface with $\iota m_h + n_h = 0$, the distance to the low-order resonance $\iota m_l + n_l = 0$ can be as small as $\Delta\iota \sim 1/m_h^2$, which results in the contribution scaling as m_h^2/m_l^4, i.e. it tends to infinity if the evaluation is at the irrational surface with ι arbitrarily close to $-n_l/m_l$. As a result, λ_{bB} asymptotic has a fractal dependence on ι, as seen from the right plot in figure 20. On the contrary, if λ_{bB} asymptotic is evaluated at low-order rational field lines, there are no other low-order rationals in the neighborhood, and the resulting data points appear to belong to the smooth curve (see the respective markers in the left plot of figure 20 which correspond to rational ι with numerators not larger than 500 while the rest of the data points have numerators up to 10 000).

Finite collisionality limits the effect of bootstrap resonances by modifying η and thus moving passing particles into the trapped particle region or deeper to the passing particle region, where the Fourier spectrum of $s_{(1)}$ decays exponentially. Therefore, only a finite ('collisionless') segment of its orbit corresponding to N toroidal turns stays in resonance with a given Fourier amplitude of $s_{(1)}$ limiting the resonant denominator to $\max(m\Delta\iota, (2\pi N)^{-1})$. We can estimate N equating the width of power law decay region $\Delta\eta \sim \eta_b\varepsilon_t(1 + \iota^2\beta)^{-1}m^{-2}$ (see above) to the boundary layer width corresponding to N turns, (4.5). Ignoring the numerical factor and $1 + \iota^2\beta \sim 1$, scaling of near-resonant contributions changes from $m^{-4}\Delta\iota^{-1}$ to $m^{-4}(\max(\Delta\iota, m^3\nu_*\varepsilon_t^{3/2}))^{-1}$. For the examples in figure 20 where the lowest-order rational number present in the ι range has $m = 11$, near-resonant contributions remain small by this estimate as long as $\nu_* > 10^{-8}$, which results in a smooth λ_{bB}

https://doi.org/10.1017/S0022377825000200 Published online by Cambridge University Press

dependence on ι in collisional cases. Since bootstrap resonances are mostly an artifact of the collisionless asymptotic limit, they are avoided in practical computations either by removal of respective near-resonant spectral modes, see, e.g. Nakajima *et al.* (1989) or by introducing a Gaussian factor in the field line integration (Boozer & Gardner 1990) which effectively mimics the collisional attenuation discussed above.

5. Effect of particle precession

As we saw from the previous analysis, off-set of the trapped particle distribution function $g_{\mathrm{off}} = g - g_0^t$ is determined in the 'well trapped' domain beyond the matching boundary η_m introduced in § 3.2, $\eta > \eta_m$, where g_{off} is essentially a constant, by the collisional solution in region containing the boundary layer, $\eta < \eta_m$, which is the consequence of the absence of a source term in the trapped particle region. This remains the case in the presence of particle precession caused by the magnetic drift and finite radial electric field if the typical relaxation rate in the 'well trapped' particle domain $\eta > \eta_m$ stays small compared with (essentially parallel) relaxation in the region $\eta_b < \eta < \eta_m$ (case of mild rotations). Since the latter region is rather narrow, $|\eta_b - \eta_m| \sim \delta\eta$, effect of the precession on the solution in this trapped particle domain and in the whole passing particle region is relatively small (Beidler 2020) as long as Mach numbers for the $\mathbf{E}\times\mathbf{B}$ drift, $v_E^* = v_E/v = \Omega_E r/v$, are small enough, $\Omega_E\tau_b/\delta\vartheta \sim v_E^* N^2 \varepsilon_t^{-3/2} \sim v_E^* \varepsilon_t^{-9/10} \nu_*^{-2/5} \ll 1$, where we estimated bounce time as the largest within the off-set pattern extending for N toroidal turns (4.6), $\tau_b \sim NR/(v\sqrt{\varepsilon_t})$, and the width of the off-set region as $\delta\vartheta \sim 1/N$. Since $v_E^* \sim \rho_L/r \ll 1$ and the respective Mach number due to magnetic drift v_B^* is even smaller, $v_B^* \sim \varepsilon_t v_E^*$, this condition is fulfilled even at very low collisionalities typical for a reactor. Therefore, we can obtain the solution in 'well trapped' particle domain $\eta > \eta_m$ from the homogeneous problem driven by Dirichlet boundary condition at $\eta = \eta_m$ where g_{off} is determined by the solution of collisional problem in the $1/\nu$ regime.

Since the trapped–passing boundary layer is excluded from the well trapped domain $\eta > \eta_m$, and class-transition boundary layers are rather narrow in the long mean free path regime, we can use for g_{off} a homogeneous bounce-average equation. In the conservative form required for proper handling of boundary conditions at class-transition boundaries and omitting the class index j for simplicity, this equation using the total energy $w = mv^2/2 + e\Phi$ and perpendicular adiabatic invariant $J_\perp = mv_\perp^2/(2\omega_c) = cm^2v^2\eta/(2e)$ as momentum space variables is

$$\frac{\partial}{\partial r}\left(J_b\langle v_g^r\rangle_b g_{\mathrm{off}}\right) + \frac{\partial}{\partial\vartheta_0}\left(J_b\langle v_g^{\vartheta_0}\rangle_b g_{\mathrm{off}}\right) = \frac{\partial}{\partial J_\perp}\left(J_b\langle D^{J_\perp J_\perp}\rangle_b \frac{\partial g_{\mathrm{off}}}{\partial J_\perp}\right), \tag{5.1}$$

where g_{off} is independent of φ. The Jacobian J_b and bounce-averaged pitch-angle diffusion coefficient $\langle D^{J_\perp J_\perp}\rangle_b = (\partial J_\perp/\partial\eta)^2\langle D^{\eta\eta}\rangle_b$ are

$$J_b = \frac{e}{c}\frac{\mathrm{d}\psi}{\mathrm{d}r}\tau_b, \qquad \langle D^{\eta\eta}\rangle_b = \frac{2\eta I_j}{l_c\tau_b}, \tag{5.2}$$

with I_j defined in the first (2.26), and bounce time τ_b together with bounce-averaged radial drift velocity $\langle v_g^r\rangle_b$ are given by (3.56) with the omission of class index k.

It should be noted that, due to the use of field aligned (Clebsch-like) spatial variables, both, $\langle v_g^r\rangle_b$ and $\langle v_g^{\vartheta_0}\rangle_b$ can be evaluated here along the field lines (see

https://doi.org/10.1017/S0022377825000200 Published online by Cambridge University Press

(Shaing 2015; Calvo *et al.* 2017; d'Herbemont *et al.* 2022)). On the contrary, for the non-aligned variables (periodic flux coordinates) tangential components of the bounce-averaged drift should be evaluated over the real bounce orbit with finite Larmor radius, which is in contrast to $\langle v_g^r\rangle_b$ where this results only in a ρ_L correction to (3.56). Such an evaluation is required to retain in the resulting precession frequency the effect of magnetic shear which is of the order one if $\Omega_E \lesssim \Omega_B$ (see (Shaing 2015; Albert *et al.* 2016; Martitsch *et al.* 2016)). A way equivalent to bounce averaging velocity components is to use equation (3.48) of Morozov & Solov'ev (1966) resulting in $\langle v_g^r\rangle_b = J_b^{-1}\partial J_\parallel/\partial\vartheta_0$ and $\langle v_g^{\vartheta_0}\rangle_b = -J_b^{-1}\partial J_\parallel/\partial r$, where $J_\parallel = m\oint \mathrm{d}l\, v_\parallel$ is the parallel adiabatic invariant computed along the field line, which makes the Liouville theorem $\partial(J_b\langle v_g^r\rangle_b)/\partial r + \partial(J_b\langle v_g^{\vartheta_0}\rangle_b)/\partial\vartheta_0 = 0$ obvious.

Equation (5.1) means that off-set effect is generally non-local, i.e. radial transport due to entrapping of passing particles at some given surface is produced in some radial range δr_c (radial correlation length) which in the $1/\nu$ regime is of the order $\delta r_c \sim \tau_d\langle v_g^r\rangle_b$, where $\tau_d \sim \varepsilon_M/\nu$ is the de-trapping time, and, at lower collisionalities, where $\langle v_g^{\vartheta_0}\rangle_b > 1/\tau_d$ and mild electric fields, $\Omega_E \leqslant \Omega_B$, is of the size of radial deviation of precessing trapped orbit which does not scale with Larmor radius and is fully determined by the magnetic field geometry. Thus, local ansatz (2.1) has a limited validity in the latter case where transport coefficients and bootstrap current need a non-local treatment, e.g. by Monte Carlo methods (Sasinowski & Boozer 1995; Satake, Kanno & Sugama 2008) (an exception is weakly perturbed tokamak equilibria where a quasi-local ansatz (Martitsch *et al.* 2016) can be used retaining the boundary layer effects). Of course, δr_c must be small compared with the plasma radius for the magnetic fields intended for the reactor, however, it is not necessarily small compared with the radial variation scale of the off-set which is quite sensitive to small modulations of the field and ι changes. One consequence of this non-locality is discussed in more details in § 6.

Equation (5.1) should be solved as is if the off-set is produced in the wide poloidal range containing the trapped–passing boundary layer, which is the case of almost aligned maxima discussed in §§ 3.3, 3.5 and 4.3. However, in a more typical case with a distinct global maximum (or two global maxima, which are also possible in stellarator symmetry), the width of the off-set region $\delta\vartheta$ is small (this is a typical width of a single strap in figures 21–24). Therefore, convective term with $\langle v_g^{\vartheta_0}\rangle_b$ dominates over $\langle v_g^r\rangle_b$ which, therefore, can be ignored in (5.1) together with the dependence on ϑ_0 of $\langle v_g^{\vartheta_0}\rangle_b \equiv \Omega^\vartheta$, J_b and $D^{J_\perp J_\perp}$, which should be taken at the global maximum point $\vartheta_0 = \vartheta_{\max}$, thus reducing (5.1) to

$$\frac{\partial g_{\mathrm{off}}}{\partial\vartheta_0} = \frac{1}{\tau_b\Omega^\vartheta}\frac{\partial}{\partial\eta}\left(\tau_b\langle D^{\eta\eta}\rangle_b\frac{\partial g_{\mathrm{off}}}{\partial\eta}\right). \tag{5.3}$$

This can be done because g_{off} is localized in ϑ_0 due to essentially trivial boundary conditions over η at $|\vartheta_0 - \vartheta_{\max}| \gg \delta\vartheta$. Therefore, solution to (5.3) in the infinite domain $-\infty < \vartheta_0 < \infty$ is sufficient to generalize the results of g_{off} computations in the $1/\nu$ regime for the case of finite precession frequencies (finite radial electric fields).

For further estimates, we assume a fast precession case, $\Omega^\vartheta\tau_d \gg \delta\vartheta$ (with $\Omega^\vartheta\tau_b \ll \delta\vartheta$ staying fulfilled, which is possible at low collisionalities where $\tau_b \ll \tau_d$), which would be the condition of the $\sqrt{\nu}$ transport regime (Galeev & Sagdeev 1979) in case $\delta\vartheta \sim 1$ but is established here for smaller precession frequencies due to $\delta\vartheta \ll 1$. In this case, solution is localized in η near the matching boundary η_m, and we can

https://doi.org/10.1017/S0022377825000200 Published online by Cambridge University Press

ignore class transitions which occur in the well trapped particle domain and also set $\eta = \eta_m$ in all the coefficients. Introducing the dimensionless variables as follows:

$$y = \frac{\vartheta - \vartheta_{\max}}{\delta\vartheta}\ \mathrm{sign}(\Omega^\vartheta), \qquad x = \left(\frac{|\Omega^\vartheta|}{\delta\vartheta\,\langle D^{\eta\eta}\rangle_b}\right)^{1/2}(\eta - \eta_m), \tag{5.4}$$

equation (5.3) is reduced to

$$\frac{\partial g_{\mathrm{off}}}{\partial y} = \frac{\partial^2 g_{\mathrm{off}}}{\partial x^2}, \tag{5.5}$$

where $0 < x < \infty$, $-\infty < y < \infty$, and the boundary conditions are $g_{\mathrm{off}}(0, y) = g_{\mathrm{off}}^{1/\nu}(\vartheta_{\max} + y\,\delta\vartheta\ \ \mathrm{sign}(\Omega^\vartheta), \eta_m)$ and $g_{\mathrm{off}}(x, -\infty) = 0$, so that solution is localized in the range $|y| \lesssim 1$. Since the solution is also localized in the range $x \lesssim 1$, the second of (5.4) results in the localization range $\eta - \eta_m < \delta_E \Delta\eta_{tr}$, where $\Delta\eta_{tr} \sim \varepsilon_t^{1/2}\eta_b$ is the width of trapped particle domain and $\delta_E \ll 1$ is the attenuation factor due to the precession (we assume here $\varepsilon_M \sim \varepsilon_t$ for simplicity). This reduction of the η integration range of $g_{\mathrm{off}} s_{(1)}$ effectively contributing to the Ware-pinch coefficient (2.11) respectively reduces its value by δ_E as compared with the $1/\nu$ regime. Explicitly, this factor is

$$\delta_E \sim \left(\frac{v\delta\vartheta}{l_c|\Omega^\vartheta|}\right)^{1/2} \sim \left(\frac{v\nu_*}{NR|\Omega^\vartheta|}\right)^{1/2}, \tag{5.6}$$

where $N \sim 1/\delta\vartheta$ is the number of toroidal turns within a given off-set pattern. The overall trend of the Ware-pinch off-set with the reduction of ν_* is obtained with the account of switching off-set patterns and thus increasing N in (5.6) according to the first (4.6). Thus, the normalized maximum off-set (4.12) is reduced from its value in $1/\nu$ regime to

$$\frac{\lambda_{\mathrm{off}}^{\max}}{\lambda_{bB}^{\mathrm{tok}}} \sim \iota\delta_E \sim \iota\varepsilon_t^{-3/20}\nu_*^{3/5}\left(\frac{v}{R|\Omega^\vartheta|}\right)^{1/2}, \tag{5.7}$$

i.e. λ_{bB} converges with decreasing collisionality to the Shaing–Callen limit. It should be noted that bootstrap resonances should still be removed from the asymptotic λ_{bB} for the same reason as discussed in § 4.4. In this case, in addition to pitch-angle scattering limiting the effective orbit length contributing to the resonance in the power low spectral decay region, also the precession de-correlates the resonant particles, effectively removing them from that region.

In case of nearly aligned maxima, poloidal width of the off-set region in (5.6) is not small anymore, $\delta\vartheta \sim 1$ or, equivalently, $N \sim 1$. Thus, using the $1/\nu$ regime estimate (4.22) we obtain the scaling for normalized off-set due to violation of ripple equivalence as

$$\frac{\lambda_{\mathrm{off}}^{\mathrm{align}}}{\lambda_{bB}^{\mathrm{tok}}} \sim \frac{\iota\,\varepsilon_t^{3/2}}{N_{\mathrm{tor}}^{1/2}\varepsilon_M^{3/4}}\left(\frac{v}{R|\Omega^\vartheta|}\right)^{1/2}, \tag{5.8}$$

which means that the off-set does not vanish but saturates with reducing collisionality at a rather high level due to the ratio of bounce frequency to the precession frequency in the last factor.

https://doi.org/10.1017/S0022377825000200 Published online by Cambridge University Press

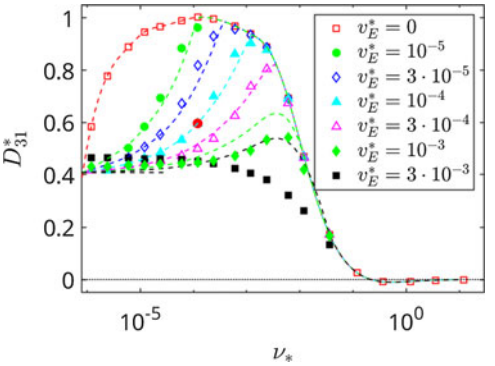

FIGURE 31. Attenuation test for the case in figure 4 of Helander *et al.* (2011). Normalized electric field values (Mach numbers $v^*_E = cE_r/(vB)$) are defined in the legend. Dashed lines show the result of scaling in (5.9) with the reference point shown by a red circle.

To verify the off-set attenuation model in case of a single off-set pattern with fixed N in (5.6), we apply this model to DKES results in figure 4 of Helander *et al.* (2011) where the dominant pattern appears to be unchanged in the whole range of ν_*. The normalized bootstrap coefficient $D^*_{31} \equiv \lambda_{bB}/\lambda^{\rm tok}_{bB}$ in this figure, where the precession is purely due to the $\mathbf{E}\times\mathbf{B}$ drift, $\Omega^{\vartheta} = \Omega_E \propto E_r$, is represented using the scaling of attenuation factor (5.6) with collisionality and radial electric field $\delta_E \propto (\nu_*/E_r)^{1/2}$ as follows:

$$D^*_{31} = D^{\rm SC}_{31} + \left(D^{1/\nu}_{31} - D^{\rm SC}_{31}\right)\frac{D^*_{\rm ref} - D^{\rm SC}_{31}}{D^{1/\nu}_{\rm ref} - D^{\rm SC}_{31}}\left(\frac{\nu_* E_{\rm ref}}{\nu_{\rm ref} E_r}\right)^{1/2}, \tag{5.9}$$

where $D^{\rm SC}_{31}$ is the Shaing–Callen asymptotic value of D^*_{31}, $D^{1/\nu}_{31}$ is the actual value in the $1/\nu$ regime, $\nu_{\rm ref}$ and $E_{\rm ref}$ are the values of ν_* and E_r for a single reference point in the plot and $D^*_{\rm ref}$ and $D^{1/\nu}_{\rm ref}$ are the values of D^*_{31} for $(\nu_*, E_r) = (\nu_{\rm ref}, E_{\rm ref})$ and $(\nu_*, E_r) = (\nu_{\rm ref}, 0)$, respectively. As one can see in figure 31, scaling (5.9) well represents the results with mild electric field but fails for two largest values of v^*_E where the (tokamak like) boundary layer off-set (Helander *et al.* 2011) becomes important (see also figure 19) and where the condition $\Omega_E\tau_b/\delta\vartheta \ll 1$ becomes violated.

6. Off-set in the direct problem, bootstrap effect at the magnetic axis

We discuss now the off-set in the direct (bootstrap) problem qualitatively. Since the off-set in the Ware-pinch problem is driven by the asymmetry of the entrapping of passing particles, off-set in the bootstrap problem is driven by the asymmetry in the inverse process of trapped particle detrapping. Similarly, there are two (same) reasons for this asymmetry. First is the asymmetry of local maxima limiting ripple domains which leads to the detrapping in the direction of the lower maximum. The second one is connected with the violation of ripple equivalence, $A_j = 1$, and, consequently, to the asymmetry of entrapping and further detrapping in the neighboring ripples. We estimate now only the first, simpler effect.

For the equilibrium (Maxwellian) particle distribution which is constant on the flux surface, the detrapping process is balanced by entrapping of passing particles leading

https://doi.org/10.1017/S0022377825000200 Published online by Cambridge University Press

to zero phase space fluxes (detailed equilibrium) and, respectively, to zero parallel current. In the presence of radial gradient, the distribution function of trapped particles is not constant on the flux surface anymore. It is larger in the region with positive bounce-averaged radial drift, and smaller where it is negative. In stellarator symmetry, it is obvious that particles are detrapped in those regions in opposite directions, thus leading to the overall shift of passing particle distribution and, respectively, to the parallel current. Destroyed symmetry of the ripple wells is described by the source term $s_{(1)}$, (2.4), which generates 'anti-particles' in the wells with $\langle v_g^r \rangle_b > 0$ and 'particles' where $\langle v_g^r \rangle_b < 0$. In the asymptotic $1/\nu$ regime, these particles and anti-particles produced by the source term $s_{(1)}$ within ripple wells can leave these wells only through boundary layers between classes, where they are re-distributed and annihilated. As we saw in §§ 2.2.1 and 2.3.1, parallel flows within these boundary layers make a contribution of the order one to the equilibrium Pfirsch–Schlüter current. This changes at finite collisionality where 'relevant ripples' appear with both limiting local maxima entering the trapped–passing boundary layer. Re-distribution of particles and anti-particles between 'relevant' ripples occurs then through the trapped–passing boundary layer (this layer is empty in the asymptotic $1/\nu$ regime) causing the parallel flow there and respective asymmetry of the distribution function over the pitch parameter λ. Such an odd distribution in the boundary layer, g^{odd}, serves as a boundary condition which shifts from zero the odd part of the distribution function in the whole passing particle domain thus generating a bootstrap current.

We can estimate g^{odd} in the boundary layer using the argument at the end of § 2.2.1 as $g^{\mathrm{odd}} \sim H_j(\eta_{\mathrm{loc}})/\delta\eta_{\mathrm{ref}}$, where $H_j(\eta_{\mathrm{loc}})$ is the collisional flux through class boundary $\eta = \eta_{\mathrm{loc}} \equiv \max(\eta_j, \eta_{j+1})$ of the relevant ripple (which corresponds to the off-set domain in the adjoint problem) with

$$H_j(\eta) = -\int_{\varphi_j}^{\varphi_{j+1}} \mathrm{d}\varphi D_\eta \frac{\partial g_{-1}}{\partial \eta}, \tag{6.1}$$

and g_{-1} being the leading-order solution of direct problem (2.27), and where $\delta\eta_{\mathrm{ref}}$ is the width of the trapped–passing boundary layer in the "main region". Since the odd part of passing particle distribution driven by g^{odd} at the trapped–passing boundary is independent of η and is, therefore, equal to g^{odd}, we can estimate the parallel current density off-set using (2.38) as $j_\parallel^{\mathrm{off}} \approx C_\parallel g^{\mathrm{odd}}$, and the respective off-set of the normalized bootstrap coefficient in (2.42) as $\lambda_{\mathrm{off}} \sim g^{\mathrm{odd}}/\rho_L \sim H_j(\eta_{\mathrm{loc}})/(\rho_L \delta\eta_{\mathrm{ref}})$. Naturally, the same result is obtained for the off-set (3.54) in the adjoint problem using for $w_{\mathrm{off}}^{(j)}$ the second equality (3.55) and for $g_{\mathrm{off}}^{(j)}$ (3.28) where $\alpha_j^{\pm} \sim 1$ in case of the maximum off-set, and constant (3.18) is

$$C_0 \approx \frac{2\eta_b \langle B^2 \rangle}{\delta\eta_{\mathrm{ref}}^2} \int_{\varphi_0}^{\varphi_N} \frac{\mathrm{d}\varphi}{B^\varphi} \sim \frac{B}{\delta\eta_{\mathrm{ref}}^2} \int_{\varphi_0}^{\varphi_N} \frac{\mathrm{d}\varphi}{B^\varphi}. \tag{6.2}$$

Note that effect of particle precession reducing the off-set in the adjoint problem is also the same in the direct problem where it causes re-distribution of trapped "particles" and "anti-particles" between trapping domains via the rotation within the

https://doi.org/10.1017/S0022377825000200 Published online by Cambridge University Press

flux surface thus reducing the collisional fluxes into class boundaries as compared with their maximum $1/\nu$ values $H_j(\eta_{\rm loc})$.

Recalling now definitions (2.26) and (2.4) of the normalized collisional velocity space flux H_j (see also (3.55) and (3.57)) we can approximately relate H_j to the radial correlation length in the off-set well $\delta r_{cj} \sim \tau_{dj}\langle v_g^r\rangle_{bj}$ as follows, $H_j \sim \tau_{bj}\langle v_g^r\rangle_{bj}\Delta\eta_j \sim \delta r_{cj}\delta\eta_j^2/\Delta\eta_j$ where τ_{bj} and $\langle v_g^r\rangle_{bj}$ are bounce time and bounce-averaged velocity (3.56), $\tau_{dj} \sim \tau_{bj}(\Delta\eta_j/\delta\eta_j)^2$ is the detrapping time, $\Delta\eta_j \sim \varepsilon_M\eta_b$ is the off-set well depth and $\delta\eta_j$ is boundary layer width in the off-set domain (see (3.26) and (3.20)). Thus, $g^{\rm odd} \sim \delta r_{cj}\delta\eta_j/(A_j\Delta\eta_j)$ with the aspect ratio $A_j = \delta\eta_{\rm ref}/\delta\eta_j$, and we can estimate current density as follows:

$$j_\parallel^{\rm off} \sim C_\parallel g^{\rm odd} \sim \frac{c\delta\eta_j\eta_b}{\rho_L A_j\Delta\eta_j}\left(p(r+\delta r_{cj}) - p(r)\right). \tag{6.3}$$

This formula actually reverses local transport ansatz (2.1) which assumes infinitesimal correlation length, and manifests the fact that variation of the distribution function on a given flux surface (along the field line) from its equilibrium value is because its value in the ripple wells is determined by the values of equilibrium distribution function at the neighboring flux surfaces displaced by the correlation length (strictly speaking, connection of parallel current density to the pressure gradient is non-local, $j_\parallel^{\rm off} = \int \mathrm{d}r' K(r,r')p(r')$, with the kernel $K(r,r')$ localized within $|r'-r| \lesssim \delta r_{cj}$). Thus, this variation and resulting parallel current need not disappear at the magnetic axis where $\mathrm{d}p/\mathrm{d}r = 0$. Expanding $p(r+\delta r_{cj})$ to the next order, we obtain parallel current on axis as

$$j_\parallel^{\rm axis} \sim \frac{c\eta_b\langle v_g^r\rangle_{bj}^2\tau_{bj}^2}{\rho_L A_j}\left(\frac{\Delta\eta_j}{\delta\eta_j}\right)^3\frac{\mathrm{d}^2p}{\mathrm{d}r^2} \sim \frac{c\eta_b\rho_L\varepsilon_M^{5/4}}{A_j N_{\rm tor}^{1/2}\nu_*^{3/2}}\frac{\mathrm{d}^2p}{\mathrm{d}r^2}, \tag{6.4}$$

where we estimated $\langle v_g^r\rangle_{bj} \sim v\rho_L/R$, $\tau_{bj} \sim R/(vN_{\rm tor}\varepsilon_M^{1/2})$, $\Delta\eta_j \sim \eta_b\varepsilon_M$ and $\delta\eta_j \sim \eta_b(\nu_*/N_{\rm tor})^{1/2}\varepsilon_M^{1/4}$, with $N_{\rm tor}$ being the number of ripples. Further denoting $\mathrm{d}^2p/\mathrm{d}r^2 = p/L_{pa}^2$ and normalizing (6.4) to a typical tokamak bootstrap current value $j_b^{\rm tok} \sim c\eta_b\iota^{-1}\varepsilon_t^{-1/2}\,\mathrm{d}p/\mathrm{d}r = c\eta_b p/(\iota\varepsilon_t^{1/2}L_p)$, we obtain

$$\frac{j_\parallel^{\rm axis}}{j_b^{\rm tok}} \sim \frac{\iota\varepsilon_t^{1/2}\varepsilon_M^{5/4}}{A_j N_{\rm tor}^{1/2}}\left(\frac{L_p}{L_{pa}}\right)^2\frac{\rho^*}{\nu_*^{3/2}}, \tag{6.5}$$

where $\rho^* = \rho_L/L_p$. Although this expression contains a small parameter ρ^* in the numerator, it has another small parameter $\nu_*^{3/2}$ in the denominator so that current on axis is not vanishingly small. Estimating for parameters of the tokamak ASDEX Upgrade in the presence of the helical core with $\varepsilon_M \sim 0.01$, $\iota \sim 0.5$, $\varepsilon_t \sim 0.25$, $A_j = 1$, $N_{\rm tor} = 2$ and central density $n_e = 3\cdot 10^{13}$ cm^{-3} and temperature $T_e = 5$ KeV resulting in $\rho^* = \rho_e^* \sim 2\cdot 10^{-4}$ and $\nu_* \sim 3.5\cdot 10^{-3}$, we get $\rho^*\nu_*^{-3/2} \approx 1$ so that $j_\parallel^{\rm axis}/j_b^{\rm tok} \sim 5\cdot 10^{-4}(L_p/L_{pa})^2$. Thus, for peaked T_e profiles (e.g. in the presence of central electron cyclotron heating) peaking factor $L_p/L_{pa} \sim 40$ is needed to make these currents comparable. Of course, in order to achieve $j_\parallel^{\rm axis}$, special conditions on the magnetic geometry are required in order to create, in particular, difference in correlation length δr_j in different ripples.

Note that we have retained in the estimates (6.4) and (6.5) only the off-set effect but ignored the usual bootstrap mechanism where radial correlation length τ_{cj} corresponds to the banana width which is much smaller for electrons than τ_{cj} resulting

https://doi.org/10.1017/S0022377825000200 Published online by Cambridge University Press

from the $1/\nu$ transport. However, this usual mechanism is not small for the ions whose radial orbit extent and, respectively, radial correlation length is much larger (with the orbits near the axis comprising a variety of classes even in an axisymmetric tokamak (Shaing, Ida & Sabbagh 2015; Buchholz *et al.* 2022)), and, more importantly, who retain due to their high mass nearly all the momentum within the species during Coulomb collisions. For the axisymmetric devices, this mechanism generates the parallel ion flow (generally different from the $E \times B$ flow) but not the current since this flow is fully compensated by the electron flow driven by the collisional friction. However, if the toroidal ripple is present, it brakes the electrons leading to some steady current on axis if the ion flow is finite there. The latter is affected by ripple too via the neoclassical toroidal viscous torque (Shaing 2015; Albert *et al.* 2016; Martitsch *et al.* 2016) which tends to bring the toroidal rotation velocity towards the (finite) intrinsic velocity driven by the ion temperature gradient. Due to the finite radial orbit width, finite gradients at surrounding flux surfaces result in finite ion rotation on axis which finally leads to a finite equilibrium current there. Generally, once the axial symmetry of the tokamak magnetic field is violated, there appear various mechanisms resulting in finite non-inductive toroidal current on axis which is necessary for the steady state tokamak operation, see, e.g. Weening & Boozer (1992). At the same time, mechanisms discussed here are rather weak for that purpose which is better achieved with help of stellarator–tokamak hybrids (Ku & Boozer 2009; Henneberg & Plunk 2024; Liang *et al.* 2025).

7. Conclusion

To sum up, we can conclude that the bootstrap current in arbitrary three-dimensional toroidal fields does not converge to the asymptotic Shaing–Callen limit in the $1/\nu$ transport regime. The collisional current off-set being the difference between the actual bootstrap current and its collisionless asymptotic stays of the order of the bootstrap current in the equivalent tokamak and only oscillates aperiodically with changing $\log \nu_*$. Moreover, for a set of configurations with aligned local magnetic field maxima (such that the global maximum is achieved at the flux surface on a line rather than at one or few points) the bootstrap current off-set diverges as $\nu_*^{-1/2}$, as long as the condition of equivalent ripples (3.31) is not fulfilled (this condition is naturally fulfilled in axisymmetric and exactly quasi-symmetric fields). In turn, in the presence of orbit precession, in particular, due to a finite radial electric field, the off-set current converges to zero with reducing collisionality as $\nu_*^{3/5}|\Omega^\vartheta|^{-1/2}$, which is in agreement with the results of numerical modeling by various codes (Beidler *et al.* 2011). Also, in the case of aligned maxima, the off-set does converge – not to zero but to a finite value which exceeds the equivalent tokamak current by a large factor $\sim (v/R\Omega^\vartheta)^{1/2} \sim \left(v_E^*\right)^{-1/2}$, where $v_E^* = cE/(vB) \ll 1$ is the perpendicular Mach number.

The missing convergence of bootstrap current in the $1/\nu$ regime to the analytical collisionless asymptotic value is the consequence of two competing limits present in the problem. Namely, analytical derivations assume explicitly or implicitly that the field line is closed after a finite number of toroidal turns so that the mean free path strongly exceeds the period of the field line closure. As a consequence, the trapped–passing boundary layer width in velocity space $\delta\eta_{\mathrm{ref}}$ is assumed infinitesimal such that all class-transition boundary layers centered around $\eta = \eta_c = 1/B_{\mathrm{loc}}$ coming from local field maxima B_{loc} which are below the global maximum B_{max} are clearly separated from the trapped–passing boundary layer centered at $\eta = \eta_b = 1/B_{\mathrm{max}}$.

https://doi.org/10.1017/S0022377825000200 Published online by Cambridge University Press

Obviously, this assumption cannot be fulfilled at irrational surfaces where the field line closure period is indeed infinite but the mean free path length stays finite, and where class-transition boundary layers inevitably interact with the trapped–passing boundary layer, leading to the bootstrap current off-set. This contradiction between two limits is manifested in the fractal spatial structure of the collisionless solutions for the distribution function, which is the fractal within the irrational flux surface in the adjoint approach (Helander *et al.* 2011) and has a fractal dependence on radius (leading to bootstrap resonances) also in the direct approach (Shaing & Callen 1983; Boozer & Gardner 1990).

The off-set which appears at any collisionality at irrational surfaces (or, equivalently, long enough rational field lines) results from the collisional particle exchange between trapped and passing particle domains in the velocity space. This exchange occurs through the boundary layer which, in usual configurations with global magnetic field maximum achieved in one or few points, is localized at the flux surface in some vicinity (contact region or 'hot spot') around this maximum such that field line returns to this vicinity after $N \propto \nu_*^{-1/5} \ll 1$ toroidal turns. The off-set of the distribution function formed between two return points is the largest from all configurations, $g_{\mathrm{off}} \propto \nu_*^{-3/5}$, but it does not lead to the divergence of bootstrap current because the normalized integral of bounce-averaged velocity over the long off-set domain, $w_{\mathrm{off}} \propto \nu_*^{3/5} \ll 1$ is the smallest and balances the former in resulting bootstrap coefficient $\lambda_{\mathrm{off}} \propto g_{\mathrm{off}} w_{\mathrm{off}}$. This compensation disappears in case of nearly aligned maxima, where boundary layer contact regions turn into stripes with much larger area than 'hot spot' in the usual case. These contact regions cut the field lines into much shorter off-set domains with the length about a single toroidal period, such that w_{off} does not scale with collisionality anymore, but the distribution function still does, $g_{\mathrm{off}} \propto \nu_*^{-1/2}$. Although this scaling is weaker than in the usual case, missing compensation leads to $\nu_*^{-1/2}$ divergence of the resulting bootstrap current. This diverging part is respectively reduced if bounce-averaged drift is minimized for trapped particles, which is naturally the case in quasi-symmetric configurations.

For the analysis of boundary layer effects and resulting off-set of bootstrap current we have developed a simplified propagator method, and obtained with its help, besides the condition of equivalent ripples (3.31) formulated earlier in Helander *et al.* (2011) as a property of ideal quasi-isodynamic stellarators leading there to a tokamak-like bootstrap effect, also the expression (3.53) for the off-set of the distribution function in the case of imperfectly aligned local maxima and a slightly violated ripple equivalence condition (3.53) together with the respective estimate (4.22) of the resulting off-set of bootstrap coefficient in the case of the devices with non-optimized bounce-averaged radial drift of trapped particles. Actually, the case of nearly aligned maxima is the most interesting from the point of view of good fusion alpha particle confinement. This is naturally the case in quasi-symmetric configurations and in quasi-isodynamic configurations with poloidally closed of contours of B. As can be seen from condition (4.22), the way to avoid the off-set of bootstrap current in such configurations is to align the maxima accurately and to realize ripple equivalence condition (3.31). The latter condition is almost the same as the condition of being tied to the flux surface contours of the parallel adiabatic invariant $J_\parallel$ for barely passing particles which, once realized in the case of perfectly aligned maxima, would prevent collisionless trapped–passing particle transitions and resulting stochastic transport. The essential difference of the respective integral I_j from $J_\parallel = m \oint \mathrm{d}l\, v_\parallel$ is only in an extra $1/B$ factor in the sub-integrand. Both conditions are naturally satisfied if quasi-symmetry conditions are realized exactly, which, however,

https://doi.org/10.1017/S0022377825000200 Published online by Cambridge University Press

cannot be achieved at all flux surfaces (Garren & Boozer 1991). More generally, these conditions are fulfilled simultaneously for perfectly omnigeneous fields (Cary & Shasharina 1997; Helander & Nührenberg, 2009) being also an idealization (Cary & Shasharina 1997).

As a curious consequence of bootstrap off-set, we have shown in § 6 a possibility of a bootstrap effect at the magnetic axis due to a rather large radial correlation length of the orbits δr_c at low plasma collisionalities where it scales in the $1/\nu$ regime as $\delta r_c \propto \rho_L/\nu_*$ and strongly exceeds the Larmor radius ρ_L. Thus, the bootstrap current on axis being vanishingly small in axisymmetric fields where, due to a vanishing gradient and $\delta r_c \sim \rho_L$, it scales as $\rho_{Le}^2/L_p^2 = (\rho_e^*)^2$, can have much larger values in the presence of three-dimensional perturbations (essentially, of a field ripple) on axis.

Since the bootstrap effect is often not desired in stellarators where it modifies the ι profile and thus affects the position of an island divertor located at the plasma edge, the minimization of the bootstrap coefficient λ_{bB} is usually one of the goals in stellarator optimization. The presence of a bootstrap off-set which is rather sensitive to plasma collisionality and the ι value does not make this task simpler, and there is little hope that the off-set effect fully vanishes at finite radial electric fields, thus allowing to use the Shaing–Callen limit alone for the reactor optimization. For typical reactor parameters, $B = 5 \cdot 10^4$ G, $n_e = 10^{14}$ cm^{-3}, $T_{i,e} = 10$ KeV, $L_p = a = 300$ cm and $\varepsilon_t = a/R = 0.1$, we obtain $\nu_* = \pi R \nu_\perp/v$ and $\rho^* = \rho/L_p$ as $\nu_*^e = 2\nu_*^i = 0.001 \div 0.1$ for the range contributing 95 % to the convolution (2.9) of bootstrap coefficient $\bar{D}_{31}$, and as $\rho_e^* \approx 2 \cdot 10^{-5}$ and $\rho_i^* \approx 10^{-3}$, respectively. Thus, using in (5.6) $\Omega^\vartheta = \Omega_E = \rho_e^* v/(R\varepsilon_t)$ together with (4.6) we obtain the maximum value of the attenuation factor $\delta_E \sim (\varepsilon_t \nu_*/(N\rho^*))^{1/2}$ as $\delta_E^{\max} \sim 1$ for the electrons, i.e. attenuation is practically unimportant for them and they mostly stay in the $1/\nu$ regime, and $0.08 \leqslant \delta_E \leqslant 1.4$ for the ions which are, therefore, significantly affected by the precession but still cannot be fully described by the collisionless limit.

As follows from § 4.3, the strongest bootstrap current off-set due to nearly aligned maxima appears for the above parameters, $\varepsilon_M \sim \varepsilon_t$, $\iota = 1$ and $N_{\text{tor}} = 5$ if the mismatch of maxima is around $\Delta B/B \sim 2.5$ % for the middle of the collisionality range (around 8 % for the highest collisionality). According to (4.22), bringing this off-set back to the level of bootstrap current in the equivalent tokamak would require to align the maxima better than $\Delta B/B \sim 0.3$ % for the lowest collisionality and to fulfill ripple equivalence condition to within $\Delta A_o \lesssim 50$ %. The latter condition does not appear to be too restrictive and can probably be achieved already when tying to the flux surface $J_\parallel$ contours for barely passing particles.

Unfortunately, the off-set in the distribution function cannot be further minimized by better fulfilling the above conditions because there remains a residual off-set containing the term $\propto \log \nu_*$ not accounted for in this paper. Nevertheless, the resulting bootstrap current off-set can still be minimized by reducing the integral bounce-averaged drift represented by factors $I_\mathcal{V}$, (3.59), which are well defined in the case of aligned maxima by magnetic field geometry alone. Certain minimization of these factors can be achieved at mild collisionalities where off-set wells are relatively short already as a by-product of minimization of $1/\nu$ transport coefficients (2.29) via ε_{eff}. This appears to be the case in W-7X 'standard' configuration where the off-set in D_{31}^* shown in figure 3 of (Kernbichler *et al.* 2016) is of the order of the Shaing–Callen value (10 % of the equivalent tokamak value) for collisionalities $\nu^* > 10^{-5}$, and where ε_{eff} is reduced by about an order of magnitude compared with a standard stellarator (see figure 10 in (Beidler *et al.* 2011)). Strong D_{31}^* off-set of the order one

https://doi.org/10.1017/S0022377825000200 Published online by Cambridge University Press

shows up there only at very low collisionalities where it is due to the (non-optimized) bounce-averaged drift of long bananas (off-set wells are long).

Of course, the above simple recipes assuming independent minimization of purely geometrical quantities (asymptotic λ_{bB} and $I_{\mathcal{V}}$) do not apply in the general case without strong alignment of field maxima where multiple off-set well types contribute simultaneously with their relative contributions depending on collisionality and precession velocity. Minimization of bootstrap current in such cases requires direct numerical evaluation of all transport coefficients and the resulting plasma parameter profiles at finite plasma collisionality (Geiger *et al.* 2015). For the evaluation of bootstrap coefficient in such cases, computations of λ_{bB} in the $1/\nu$ regime would be useful if one accounts for the precession by bounce-averaged approach outlined in § 5. A particular tool for this is NEO-2 which has been specially designed for the effective evaluation of bootstrap current. Another option would be a fast neoclassical code MONKES (Escoto *et al.* 2024, 2025) which, similarly to NEO-2, has an efficiently parallelizable algorithm.

It should be noted that the two above geometric criteria are naturally met in the case of quasi-poloidal symmetry (Spong *et al.* 2001). For such an exact symmetry, $\lambda_{bB} \propto B_{\vartheta} = 0$ in the absence of auxiliary current, while $I_{\mathcal{V}} = 0$ for all exact quasi-symmetries which can actually be approached very closely (Landreman & Paul 2022). More generally, these criteria are met by ideal (omnigeneous) quasi-isodynamic fields (Helander & Nührenberg, 2009; Helander *et al.* 2011). Recent realizations of a quasi-isodynamic field which are rather close to such an ideal field (Goodman *et al.* 2023, 2024) do indeed show very low values of the bootstrap coefficient. Note that mis-alignment of maxima in these configurations is clearly below 2.5 %.

Acknowledgements

The authors gratefully acknowledge useful discussions with P. Helander, M.F. Heyn and F.I. Parra, as well as discussions and regular help in the maintenance of NEO-2 code from A.F. Martitsch and R. Buchholz. The authors are also grateful to P. Helander and co-authors for the data for figure 31. We thank A. Hirczy for long-standing support on hardware and software for computations.

Editor Per Helander thanks the referees for their advice in evaluating this article.

Funding

This work has been carried out within the framework of the EUROfusion Consortium, funded by the European Union via the Euratom Research and Training Programme (Grant Agreement No 101052200 – EUROfusion). Views and opinions expressed are, however, those of the author(s) only and do not necessarily reflect those of the European Union or the European Commission. Neither the European Union nor the European Commission can be held responsible for them. We gratefully acknowledge support from NAWI Graz.

Declaration of interests

The authors report no conflict of interest.

Data availability statement

The data that support the findings of this study are openly available in Zenodo at http://doi.org/10.5281/zenodo.14888543, reference number 14888544.

Appendix A. Fourier amplitudes $\mathcal{V}^s_{mn}$ of high harmonics.

Integration by parts can be used to check that Fourier coefficients of the analytical periodic function (whose derivatives of any order are finite) decay with harmonic index m faster than any power m^{-k} where k is an arbitrary positive integer, i.e. their decay is exponential. Power law decay of Fourier amplitude appears if some finite-order derivative turns into infinity at one or few points whose close vicinity mainly determines this amplitude at high m. This is the case of function $\mathcal{V}$ given by (3.60) with $\eta^{(j)}_{\rm loc}$ set to η_b, so that first- and higher-order derivatives of $\mathcal{V}$ over angles are infinite at the global maximum point. Using a simple model field

$$B = B_{00}\left(1 + \varepsilon_t \cos\vartheta + \varepsilon_h \cos\left(N_{\rm tor}\varphi\right)\right), \tag{A.1}$$

which differs from (2.57) by terms quadratic in ε_t and $\varepsilon_M = 2\varepsilon_h$ and shift of the angles by π, and ignoring angular dependence of non-singular factors we present the Fourier amplitudes of $\mathcal{V}$ as

$$\mathcal{V}^s_{mn} \approx \frac{2m}{B_{00}^2} U_{mn}, \qquad U_{mn} = \frac{1}{4\pi^2}\int\limits_{-\pi}^{\pi} \mathrm{d}\vartheta \int\limits_{-\pi}^{\pi} \mathrm{d}\varphi \;\; \mathrm{e}^{-im\vartheta - in\varphi} U(\vartheta, \varphi), \tag{A.2}$$

where coefficients U_{mn} are real due to stellarator symmetry of

$$U(\vartheta, \varphi) = \left(\varepsilon_t\left(1 - \cos\vartheta\right) + \varepsilon_h\left(1 - \cos\left(N_{\rm tor}\varphi\right)\right)\right)^{3/2}. \tag{A.3}$$

Integrating in (A.2) by parts over both angles and explicitly computing the resulting second derivative $\partial^2 U/(\partial\vartheta\,\partial\varphi)$ we present

$$U_{mn} = \frac{3\varepsilon_t\varepsilon_h N_{\rm tor}}{16mn}\left(W_{m+1,n+N_{\rm tor}} + W_{m-1,n-N_{\rm tor}} - W_{m+1,n-N_{\rm tor}} - W_{m-1,n+N_{\rm tor}}\right), \tag{A.4}$$

where coefficients

$$W_{m,n} = \frac{1}{4\pi^2}\int\limits_{-\pi}^{\pi} \mathrm{d}\vartheta \int\limits_{-\pi}^{\pi} \mathrm{d}\varphi \;\; \mathrm{e}^{-im\vartheta - in\varphi}\left(\varepsilon_t\left(1 - \cos\vartheta\right) + \varepsilon_h\left(1 - \cos\left(N_{\rm tor}\varphi\right)\right)\right)^{-1/2}, \tag{A.5}$$

differ from zero for $n = kN_{\rm tor}$, where k is an integer. Reducing the integration over φ for such n to a single field period, expanding in the sub-integrand $(1 - \cos\vartheta) \approx \vartheta^2/2$ and $1 - \cos\left(N_{\rm tor}\varphi\right) \approx N_{\rm tor}^2\varphi^2/2$ and then extending the integration over both angles to the infinite limits, which is justified for large m and n, we get

$$\begin{aligned} W_{m,n} &\approx \frac{N_{\rm tor}}{2\sqrt{2}\pi^2}\int\limits_{-\infty}^{\infty} \mathrm{d}\vartheta \int\limits_{-\infty}^{\infty} \mathrm{d}\varphi \;\; \mathrm{e}^{-im\vartheta - in\varphi}\left(\varepsilon_t\vartheta^2 + \varepsilon_h N_{\rm tor}^2\varphi^2\right)^{-1/2} \\ &= \frac{N_{\rm tor} I_W}{2\pi^2\sqrt{2(\varepsilon_t n^2 + \varepsilon_h N_{\rm tor}^2 m^2)}}, \end{aligned} \tag{A.6}$$

https://doi.org/10.1017/S0022377825000200 Published online by Cambridge University Press

where we changed the integration variables from (ϑ, φ) to polar variables (ρ, ϕ) as follows:

$$\vartheta = \left(m^2 + \frac{n^2\varepsilon_t}{\varepsilon_h N_{\rm tor}^2}\right)^{-1/2} \rho\cos\phi, \qquad \varphi = \left(n^2 + \frac{m^2\varepsilon_h N_{\rm tor}^2}{\varepsilon_t}\right)^{-1/2} \rho\sin\phi, \tag{A.7}$$

in order to get

$$I_W = \int\limits_0^\infty \mathrm{d}\rho \int\limits_{-\pi}^{\pi} \mathrm{d}\phi \;\; \mathrm{e}^{-i\rho\sin(\phi+\chi)} = 2\pi \int\limits_0^\infty \mathrm{d}\rho\, J_0(\rho) = 2\pi. \tag{A.8}$$

Here, $\chi = \mathrm{atan}\left((\varepsilon_h/\varepsilon_t)^{1/2} m N_{\rm tor}/n\right)$ and $J_0(\rho)$ is Bessel function of the first kind. For large m and n finite differences in (A.4) can be approximated by derivatives

$$U_{mn} \approx \frac{3\varepsilon_t\varepsilon_h N_{\rm tor}^2}{4mn} \frac{\partial^2}{\partial m \partial n} W_{m,n} \approx \frac{9\varepsilon_t^2\varepsilon_h^2 N_{\rm tor}^5}{4\pi\sqrt{2}\left(\varepsilon_t n^2 + \varepsilon_h N_{\rm tor}^2 m^2\right)^{5/2}}. \tag{A.9}$$

Expressing here modulation amplitudes via second derivatives of the field at the global maximum

$$\varepsilon_t = -\frac{1}{B_{00}}\frac{\partial^2 B}{\partial\vartheta^2}, \qquad \varepsilon_h N_{\rm tor}^2 = -\frac{1}{B_{00}}\frac{\partial^2 B}{\partial\varphi^2} = -\frac{1}{\beta B_{00}}\frac{\partial^2 B}{\partial\vartheta^2}, \tag{A.10}$$

where β is defined in (4.1) and approximating $\eta_b \approx 1/B_{00}$ we present (A.9) as

$$U_{mn} \approx \frac{9\beta^{1/2}\eta_b^{3/2}}{4\pi\sqrt{2}} \left|\frac{\partial^2 B}{\partial\vartheta^2}\right|^{3/2} \frac{N_{\rm tor}}{(m^2+\beta n^2)^{5/2}} \tag{A.11}$$

which, together with $\eta_b \approx 1/B_{00}$ in the first (A.2), results in (4.11).

REFERENCES

ALBERT, C.G., BUCHHOLZ, R., KASILOV, S.V., KERNBICHLER, W. & RATH, K. 2023 Alpha particle confinement metrics based on orbit classification in stellarators. *J. Plasma Phys.* **89** (3), 955890301.

ALBERT, C.G., HEYN, M.F., KAPPER, G., KASILOV, S.V., KERNBICHLER, W. & MARTITSCH, A.F. 2016 Evaluation of toroidal torque by non-resonant magnetic perturbations in tokamaks for resonant transport regimes using a Hamiltonian approach. *Phys. Plasmas* **23** (8), 082515.

ALBERT, C.G., KASILOV, S.V. & KERNBICHLER, W. 2020*a* Accelerated methods for direct computation of fusion alpha particle losses within stellarator optimization. *J. Plasma Phys.* **86** (2), 815860201.

ALBERT, C.G., KASILOV, S.V. & KERNBICHLER, W. 2020*b* Symplectic integration with non-canonical quadrature for guiding-center orbits in magnetic confinement devices. *J. Comput. Phys.* **403** (2), 109065.

BEIDLER, C., et al. 1990 Physics and engineering design for Wendelstein VII-X. *Fusion Technol.* **17** (1), 148–168.

BEIDLER, C.D. 2020 Final report on deliverable S2-WP19.1-T005-D005 Neoclassical and fast-ion transport. *EUROfusion internal communication*.

BEIDLER, C.D., et al. 2011 Benchmarking of the mono-energetic transport coefficients - results from the international collaboration on neoclassical transport in stellarators (ICNTS). *Nucl. Fusion* **51** (7), 076001.

BEIDLER, C.D. & D'HAESELEER, W.D. 1995 A general solution of the ripple-averagedkinetic equation (GSRAKE). *Plasma Phys. Control. Fusion* **37** (4), 463–490.

https://doi.org/10.1017/S0022377825000200 Published online by Cambridge University Press

Belli, E.A. & Candy, J. 2015 Neoclassical transport in toroidal plasmas with nonaxisymmetric flux surfaces. *Plasma Phys. Control. Fusion* **57** (5), 054012.

Boozer, A.H. 1981 Plasma equilibrium with rational magnetic surfaces. *Phys. Fluids* **24** (11), 1999–2003.

Boozer, A.H. & Gardner, H.J. 1990 The bootstrap current in stellarators. *Phys. Fluids B* **2** (10), 2408–2421.

Buchholz, R., Kasilov, S.V., Kernbichler, W., Grabenwarter, L., Savchenko, A.A. & Albert, C.G. 2022 Account of non-standard orbits in computations of neoclassical toroidal viscous torque in the resonant plateau regime of a tokamak. *J. Phys.: Conf. Ser.* **2397** (12), 012012.

Calvo, I., Parra, F.I., Velasco, J.L. & Alonso, J.A. 2017 The effect of tangential drifts on neoclassical transport in stellarators close to omnigeneity. *Plasma Phys. Control. Fusion* **59** (5), 055014.

Cary, J.R. & Shasharina, S.G. 1997 Omnigenity and quasihelicity in helical plasma confinement systems. *Phys. Plasmas* **4** (9), 3323–3333.

Chambliss, A., Paul, E. & Hudson, S. 2024 Fast particle trajectories and integrability in quasiaxisymmetric and quasihelical stellarators. *arXiv preprint* 2411.04289.

d'Haeseleer, W.D., Hitchon, W.N.G., Callen, J.D. & Shohet, J.L. 1991 *Flux Coordinates and Magnetic Field Structure*. Springer-Verlag.

d'Herbemont, V., Parra, F.I., Calvo, I. & Velasco, J.L. 2022 Finite orbit width effects in large aspect ratio stellarators. *J. Plasma Phys.* **88** (5), 905880507.

Escoto, F.J., Velasco, J.L., Calvo, I., Landreman, M. & Parra, F.I. 2024 MONKES: a fast neoclassical code for the evaluation of monoenergetic transport coefficients in stellarator plasmas. *Nucl. Fusion* **64** (7), 076030.

Escoto, F.J., Velasco, J.L., Calvo, I. & Sánchez, E. 2025 Evaluation of neoclassical transport in nearly quasi-isodynamic stellarator magnetic fields using MONKES. *Nucl. Fusion* **65** (3), 036017.

Galeev, A.A. & Sagdeev, R.Z. 1979 Theory of neoclassical diffusion. In *Reviews of Plasma Physics*, vol. **7**, pp. 257–343. Consultants Bureau.

Garren, D.A. & Boozer, A.H. 1991 Existence of quasihelically symmetric stellarators. *Phys. Fluids B* **3** (11), 2822–2834.

Geiger, J., Beidler, C.D., Feng, Y., Maassberg, H., Marushchenko, N.B. & Turkin, Y. 2015 Physics in the magnetic configuration space of W-7X. *Plasma Phys. Control. Fusion* **57** (1), 014004.

Goodman, A.G., Camacho Mata, K., Henneberg, S.A., Jorge, R., Landreman, M., Plunk, G.G., Smith, H.M., Mackenbach, R.J.J., Beidler, C.D. & Helander, P. 2023 Constructing precisely quasi-isodynamic magnetic fields. *J. Plasma Phys.* **89** (9), 905890504.

Goodman, A.G., Xanthopoulos, P., Plunk, G.G., Smith, H., Nührenberg, C., Beidler, C.D., Henneberg, S.A., Roberg-Clark, G., Drevlak, M. & Helander, P. 2024 Quasi-isodynamic stellarators with low turbulence as fusion reactor candidates. *PRX Energy* **3** (2), 023010.

Hardy, G.H. & Wright, E.M. 1985 *An Introduction to the Theory of Numbers*. Oxford University Press.

Helander, P., Geiger, J. & Maassberg, H. 2011 On the bootstrap current in stellarators and tokamaks. *Phys. Plasmas* **18** (9), 092505.

Helander, P. & Nührenberg, J. 2009 Bootstrap current and neoclassical transport in quasi-isodynamic stellarators. *Plasma Phys. Control. Fusion* **51** (5), 055004.

Helander, P., Parra, F.I. & Newton, S.L. 2017 Stellarator bootstrap current and plasma flow velocity at low collisionality. *J. Plasma Phys.* **83** (2), 905830206.

Helander, P. & Sigmar, D.J. 2002 *Collisional Transport in Magnetized Plasmas*. Cambridge University Press.

Henneberg, S.A. & Plunk, G.G. 2024 Compact stellarator-tokamak hybrid. *Phys. Rev. Res.* **6** (2), L022052.

Heyn, M.F., Ivanov, I.B., Kasilov, S.V., Kernbichler, W., Loarte, A., Nemov, V.V. & Runov, A.M. 2012 On the confnement of passing alpha particles in a tokamak-reactor with resonant magnetic field perturbations shielded by plasma currents. *Nucl. Fusion* **52** (5), 054010.

Hinton, F.L. & Hazeltine, R.D. 1976 Theory of plasma transport in toroidal confinement systems. *Rev. Mod. Phys.* **48** (2), 239–308.

HIRSHMAN, S.P., SHAING, K.C., VAN RIJ, W.I., BEASLEY, C.O., Jr. & CRUME, E.C., Jr. 1986 Plasma transport coefficients for nonsymmetric toroidal confinement systems. *Phys. Fluids* **29** (9), 2951–2959.

KAPPER, G., KASILOV, S.V., KERNBICHLER, W. & ARADI, M. 2018 Evaluation of relativistic transport coefficients and the generalized Spitzer function in devices with 3D geometry and finite collisionality. *Phys. Plasmas* **25** (12), 122509.

KAPPER, G., KASILOV, S.V., KERNBICHLER, W., MARTITSCH, A.F., HEYN, M.F., MARUSHCHENKO, N.B. & TURKIN, YU 2016 Electron cyclotron current drive simulations for finite collisionality plasmas in Wendelstein 7-X using the full linearized collision model. *Phys. Plasmas* **23** (11), 112511.

KASILOV, S.V., KERNBICHLER, W., MARTITSCH, A.F., MAASSBERG, H. & HEYN, M.F. 2014 Evaluation of the toroidal torque driven by external non-resonant non-axisymmetric magnetic field perturbations in a tokamak. *Phys. Plasmas* **21** (9), 092506.

KASILOV, S.V., REITER, D., RUNOV, A.M., KERNBICHLER, W. & HEYN, M.F. 2002 On the "magnetic" nature of electron transport barriers in tokamaks. *Plasma Phys. Control. Fusion* **44** (5), 986–1004.

KERNBICHLER, W., KASILOV, S.V., KAPPER, G., MARTITSCH, A.F., NEMOV, V.V. & HEYN, M.F. 2016 Solution of drift kinetic equation in stellarators and tokamaks with broken symmetry using the code NEO-2. *Plasma Phys. Control. Fusion* **58** (10), 104001.

KERNBICHLER, W., KASILOV, S.V., LEITOLD, G.O., NEMOV, V.V. & ALLMAIER, K. 2008 Recent progress in NEO-2 - a code for neoclassical transport computations based on field line tracing. *Plasma Fusion Res.* **3**, S1061–S1061-4.

KU, L.-P. & BOOZER, A.H. 2009 Nonaxisymmetric shaping of tokamaks preserving quasiaxisymmetry. *Phys. Plasmas* **16** (8), 082506.

LANDREMAN, M., BULLER, S. & DREVLAK, M. 2022 Optimization of quasi-symmetric stellarators with self-consistent bootstrap current and energetic particle confinement. *Phys. Plasmas* **29** (8), 082501.

LANDREMAN, M. & PAUL, E. 2022 Magnetic fields with precise quasisymmetry for plasma confinement. *Phys. Rev. Lett.* **128** (3), 035001.

LIANG, Y., ZHOU, Y., DONG, F., ZHU, C., YU, G., ZHAO, Y. & DONG, G. 2025 Design of 3D equilibria and coils for steady-state operation of tokamaks. *Nucl. Fusion* **65** (2), 026033.

MAASSBERG, H. 2004 Private communication.

MAASSBERG, H., BEIDLER, C.D. & TURKIN, Y. 2009 Momentum correction techniques for neoclassical transport in stellarators. *Phys. Plasmas* **16** (7), 072504.

MARTITSCH, A.F. *et al.*et al. 2016 Effect of 3D magnetic perturbations on the plasma rotation in ASDEX upgrade. *Plasma Phys. Control. Fusion* **58** (7), 074007.

MIKHAILOV, M.I., SHAFRANOV, V.D., SUBBOTIN, A.A., ISAEV, M.YU, NÜHRENBERG, J., ZILLE, R. & COOPER, W.A. 2002 Improved particle confinement in stellarators with poloidally closed contours of the magnetic field strength. *Nucl. Fusion* **42** (11), L23–L26.

MOROZOV, A.I. & SOLOV'EV, L.S. 1966 Motion of charged particles in electromagnetic fields. In *Reviews of Plasma Physics*, vol. **2**, pp. 201–297. Consultants Bureau.

MYNICK, H.E., CHU, T.K. & BOOZER, A.H. 1982 Class of model stellarator fields with enhanced transport. *Phys. Rev. Lett.* **48** (5), 322–326.

NAKAJIMA, N., OKAMOTO, M., TODOROKI, J., NAKAMURA, Y. & WAKATANI, M. 1989 Optimization of the bootstrap current in a large helical system with $l = 2$. *Nucl. Fusion* **29** (4), 605–616.

NEMOV, V.V., KALYUZHNYJ, V.N., KASILOV, S.V., DREVLAK, M., NÜHRENBERG, J., KERNBICHLER, W., REIMAN, A. & MONTICELLO, D. 2004 Study of neoclassical transport and bootstrap current for W7-X in the $1/\nu$ regime, using results from the PIES code. *Plasma Phys. Control. Fusion* **46** (1), 179–191.

NEMOV, V.V., KASILOV, S.V., KERNBICHLER, W. & HEYN, M.F. 1999 Evaluation of $1/\nu$ neoclassical transport in stellarators. *Phys. Plasmas* **6** (12), 4622–4632.

NÜHRENBERG, J. & ZILLE, R. 1988 Quasi-helically symmetric toroidal stellarators. *Phys. Lett. A* **129** (2), 113–117.

VAN RIJ, W.I. & HIRSHMAN, S.P. 1989 Variational bounds for transport coefficients in three-dimensional toroidal plasmas. *Phys. Fluids B* **1** (3), 563–569.

SASINOWSKI, M. & BOOZER, A.H. 1995 A δf Monte Carlo method to calculate plasma currents. *Phys. Plasmas* **2** (3), 610–619.

SATAKE, S., KANNO, R. & SUGAMA, H. 2008 Development of a non-local neoclassical transport code for helical configurations. *Plasma Fusion Res.* **3**, S1062.

SHAING, K.C. 2015 Superbanana and superbanana plateau transport in finite aspect ratio tokamaks with broken symmetry. *J. Plasma Phys.* **81** (2), 905810203.

SHAING, K.C. & CALLEN, J.D. 1983 Neoclassical flows and transport in nonaxisymmetric toroidal plasmas. *Phys. Fluids* **26** (11), 3315–3326.

SHAING, K.C. & HOKIN, S.A. 1983 Neoclassical transport in a multiple-helicity torsatron in the low-collisionality ($1/\nu$) regime. *Phys. Fluids* **26** (8), 2136–2139.

SHAING, K.C., IDA, K. & SABBAGH, S.A. 2015 Neoclassical plasma viscosity and transport processes in non-axisymmetric tori. *Nucl. Fusion* **55** (12), 125001.

SMIRNOVA, M.S. 1997 Improvement of the highly energetic passing particle confinement in torsatrons and heliotrons. *Phys. Plasmas* **4** (7), 2584–2596.

SOLOV'EV, L.S. & SHAFRANOV, V.D. 1970 Plasma confinement in closed magnetic systems. In *Reviews of Plasma Physics*, vol. **5**, pp. 1–247. Consultants Bureau.

SPONG, D.A. *et al.*et al. 2001 Physics issues of compact drift optimized stellarators. *Nucl. Fusion* **41** (6), 711–716.

SUBBOTIN, A.A., et al. 2006 Integrated physics optimization of a quasi-isodynamic stellarator with poloidally closed contours of the magnetic field strength. *Nucl. Fusion* **46** (11), 921–927.

SUGAMA, H. & NISHIMURA, S. 2002 How to calculate the neoclassical viscosity, diffusion, and current coefficients in general toroidal plasmas. *Phys. Plasmas* **9** (11), 4637–4653.

SUGAMA, H. & NISHIMURA, S. 2008 Moment-equation methods for calculating neoclassical transport coefficients in general toroidal plasmas. *Phys. Plasmas* **15** (4), 042502.

TAGUCHI, M. 1992 A method for calculating neoclassical transport coefficients with momentum conserving collision operator. *Phys. Fluids B* **4** (11), 3638–3643.

WEENING, R.H. & BOOZER, A.H. 1992 Completely bootstrapped tokamak. *Phys. Fluids B* **4** (1), 159–170.